

THIN P-CLAD InGaAs SINGLE QUANTUM WELL LASERS

By

CHIH-HUNG WU

A DISSERTATION PRESENTED TO THE GRADUATE SCHOOL
OF THE UNIVERSITY OF FLORIDA IN PARTIAL FULFILLMENT
OF THE REQUIREMENTS FOR THE DEGREE OF
DOCTOR OF PHILOSOPHY

UNIVERSITY OF FLORIDA

1996

TO MY FAMILY

ACKNOWLEDGMENTS

I wish to express my sincere gratitude to Dr. Peter S. Zory, my advisor, for accepting and supporting me for graduate study. His guidance and constant source of encouragement have proved to be essential in the successful completion of this work. I attribute the knowledge I have acquired in the field of quantum well lasers to his academic leadership and expertise. His commitment to hard work and discipline has inspired me through the course of this study.

I would like to thank the members of my supervisory committee, Dr. Gijs Bosman, Dr. Arnost Neugroschel, Dr. Ramakant Srivastava and Dr. Robert M. Park, for giving me helpful suggestions and critiques. I am grateful to Dr. Gary Evans of Southern Methodist University for providing the Modeig program, of great use in laser structure modal loss computations. I want to express my greatest appreciation to Dr. Mark A. Emanuel of Lawrence Livermore National Lab. for providing the MOCVD grown InGaAs/GaAs SQW laser material used in this study. I would also like to thank Dr. David P. Bour of Xerox PARC for supplying GaInP/AlGaInP material during the experiments. My appreciation is especially extended to the Institute of Nuclear Energy Research (INER) in Taiwan for supporting and encouraging me to complete my Ph.D. study.

I have to recognize other individuals who have provided invaluable assistance. I wish to thank Mr. James Chamblee and Mr. Tim Vanght of the Microelectronics Laboratory for all the technical assistance they provided over the years. In addition, I thank all my colleagues in the Photonics Research Laboratory: Horng-Jye Luo, Young-Soh Park, Michael Grove, Chi-Lin Young, Craig Largent, Chia-Fu Hsu and Jeong-Seok O for their friendship and inspiration.

Last, I want to thank my parents for their love and for teaching me how important education is. I am deeply indebted to my mother-in-law for supporting and helping taking care of my son during my studying abroad. I would like to express greatest appreciation to my wife Yu-Fen Shen and my sons Pei-Shen Wu and Conan S. Wu for their love and understanding. I would also like to thank my sisters and my wife's sisters for their encouragement and support.

TABLE OF CONTENTS

	<u>page</u>
ACKNOWLEDGMENTS.....	iii
ABSTRACT.....	vii
CHAPTERS	
1 INTRODUCTION.....	1
2 CONTACT REFLECTIVITY EFFECTS ON THIN P-CLAD InGaAs SINGLE QUANTUM WELL LASERS.....	8
2.1 Introduction.....	8
2.2 Laser Material and Theoretical Calculations.....	9
2.3 Experimental Results and Discussions.....	19
3 THIN P-CLAD RIDGE GUIDED LASERS.....	37
3.1 Introduction.....	37
3.2 Theoretical Calculations.....	38
3.3 Device Fabrication.....	40
3.4 Pulse Current Characteristics.....	41
3.5 CW Current Characteristics.....	43
3.6 Ridge Height Dependent Diode Laser Performance.....	45
4 DUAL WAVELENGTH DIODE LASERS AND THERMAL RESISTANCE IMPROVEMENT.....	59
4.1 Introduction.....	59
4.2 Fabrication of Dual Wavelength Diode Lasers.....	61
4.3 Dual Wavelength Laser Experimental Results and Discussion.....	62
4.4 Thermal Resistance Improvements.....	65
5 P*-GaAs CAP LAYER THICKNESS EFFECTS.....	91
5.1 Introduction.....	91
5.2 Laser Structure and Theoretical Calculations.....	92
5.3 Long Time Lasing Delay in Gain-Guided Lasers.....	94
5.4 Long Time Lasing Delay and Q-Switching	

	Lasing Delay in Narrow Stripe, 300 nm Ridge- Height Lasers	105
6	SURFACE SENSITIVE LASER DIODES	134
	6.1 Introduction	134
	6.2 Device Structure and Theoretical Calculations	135
	6.3 Device Fabrications	142
	6.4 Device Characterizations	143
7	SUMMARY and RECOMMENDATION	160
	7.1 Summary	160
	7.2 Recommendation for Future Study	163
	REFERENCES	169
	BIOGRAPHICAL SKETCH	176

Abstract of Dissertation Presented to the Graduate School of
the University of Florida in Partial Fulfillment of the
Requirements for the Degree of Doctor of Philosophy

THIN P-CLAD InGaAs SINGLE QUANTUM WELL LASERS

By

CHIH-HUNG WU

May 1996

Chairman: Peter Zory

Major Department: Electrical and Computer Engineering

The surface sensitive aspects of InGaAs single quantum well, semiconductor diode lasers with thin p-type cladding layers (thin p-clad lasers) are studied. Experiments using different thickness quantum wells (QW), contact layers (p⁺-cap layers), contact layer metallurgies and laser geometries are described and modeled.

Lasers fabricated with a QW thickness of 10 nm, an AlGaAs p-clad thickness of 250 nm, a GaAs p⁺-cap layer thickness of 100 nm and a nickel contact show significantly higher threshold currents and lower slope efficiencies than lasers fabricated with gold contacts. For a range of cavity lengths, the lasing wavelength of the nickel contact lasers is about 50 nm shorter than the gold contact lasers. This phenomenon is exploited to demonstrate side by side lasers on

the same chip with operating wavelengths of 960 and 910 nm. In a 5 μm -stripe, low-ridge configuration, the gold contact lasers operate continuously with single spatial mode output power comparable to those of conventional, high-ridge, thick p-clad lasers.

When the QW thickness is reduced to 8 nm and the GaAs p⁺-cap layer thickness is increased from 100 nm to 200 nm, new types of effects are observed. For example, when lasers with 50 micron stripe widths and gold contacts are operated, they show microsecond-long lasing delays. This long delay is attributed to the time it takes for the active region to heat to the point where net mode gain exceeds mirror loss. Net mode gain increase is due to an increase in mode overlap with the QW material gain as well as a decrease in mode overlap with the lossy gold contact layer. When the p⁺-cap layer is decreased below 170 nm, laser performance is significantly improved and no lasing delay obtained.

By combining 100 nm and 200 nm p⁺-cap layer structures into one laser and removing the gold layer from the 200 nm section, laser output power at fixed current becomes dependent on the type of material placed on the 200 nm section. Experiments using these "surface sensitive" diode lasers are described and their possible use in sensor applications discussed.

CHAPTER 1

INTRODUCTION

Semiconductor material growth technology continues to improve and very high quality epitaxial, multi-layered structures are now available. The improved materials are being used in the fabrication of various types of semiconductor devices including semiconductor diode lasers. The features of small physical dimension, high efficiency, high speed and low cost have made semiconductor diode lasers important and widely-used devices in optical fiber communication and optical memory systems.

In most diode laser applications, it is usually desirable that the devices have low threshold current density (J_{th}) and high differential quantum efficiency (η_d). To fulfill these two requirements, diode laser structures must be designed to have both optical field and carrier confinement. Normally, the active region of diode lasers is grown and confined in a pair of cladding layers which have higher energy bandgaps and smaller refractive index than those of the active region. Additionally, the thickness of the

cladding layer is usually greater than $1.0\text{ }\mu\text{m}$ to reduce the optical loss from the contact layer and substrate.

For continuous wave (cw) or rapidly pulsed operation, the removal of heat generated in the active region is crucial to the reliability of diode lasers. To obtain highly reliable cw operation and reduce the temperature sensitivity of threshold current, the thermal impedance of the diode laser structure must be as small as possible. Theoretical work showed that the thermal resistance of diode lasers can be reduced by decreasing the thickness of the cladding layers [Joyc75]. Experimental study of double heterostructure (DH) lasers with $\sim 0.12\text{ }\mu\text{m}$ active layer thickness showed that J_{th} increases and η_d decreases dramatically when the p-type AlGaAs cladding layer thickness is less than $0.8\text{ }\mu\text{m}$ [Case75]. Similar results were also theoretically obtained in [Butl75], where the active region gain at threshold (G_{th}) increased significantly as the p-AlGaAs cladding layer thickness was reduced to less than $\sim 1.0\text{ }\mu\text{m}$ due to the increase of optical loss.

Despite the increase of G_{th} caused by the optical loss, several reports have been published using this "thin cladding layer" diode laser structure. Since the cladding layer thickness is thin, the separation distance between the active region and p-contact layer or substrate is reduced. As a result, the interaction between the tail of lasing modes and either contact layer or corrugated-substrate could be very

strong to provide grating coupled output [Zory75] or distributed feedback (DFB) action [Scif75]. In recent years, several publications have been issued relating the utilization of thin p-cladding layer diode laser structures with the fabrication of surface emission [Maco87, Mott89] and edge emission [Shan88] DFB diode lasers. Additionally, in order to reduce the optical loss of diode lasers with thin p-cladding layers, shiny Au-contacts were found to be essential [Luo90].

In previous studies of thin p-clad diode lasers, the device structures were mostly concentrated on DH diode lasers. The effects of decreasing p-cladding layer thickness on the performance of quantum well (QW) lasers are relatively unknown. In order to study these effects, single quantum well (SQW) InGaAs lasers with thin p-cladding layers (250 nm) were used in this study. The diode laser performance is found to be greatly related to the reflectivity of the contact metal. As mentioned before, there could be strong interaction between the contact metal and the tail of the lasing mode when the p-cladding layer thickness is thin enough. This interaction not only changes the modal loss [Wu94b] and lasing threshold conditions but also shifts the lasing wavelength of the QW lasers [Wu94a]. In addition to the study of contact reflectivity effects, the device fabrication technique of this thin p-clad diode structure is also explored.

Diode lasers with single spatial mode operation are useful for increasing the coupling efficiency in optical fiber communication applications. Conventionally, "ridge-guided" diode lasers with thick p-cladding layer ($>1.0\text{ }\mu\text{m}$) are fabricated to achieve this single spatial mode operation output. By using such a thick p-cladding layer diode laser structure, a deep etching step has to be performed to remove certain amounts of the outside stripe material to obtain a sufficient refractive index step between the stripe and outside stripe region for maintaining the ridge-guided property. This removal process can be obtained by either wet chemical etching or using more sophisticated RIE (reactive ion etching) techniques. Because the ridge height is critical for diode lasers to operate in the index-guided regime, a very thin "etch-stop" layer is usually grown inside the diode laser structure to make the device fabrication process somewhat less complicated. On the contrary, by using the thin p-clad laser structure, one does not need to do any etching and the fabrication process of index-guided diode lasers is greatly simplified. Single spatial mode lasing to high power levels comparable to that of the conventional thick p-clad diode lasers was obtained [Wu95].

Multi-wavelength emission diode lasers are very attractive for the application of wavelength division multiplexed communication systems. Several approaches have been reported for fabricating monolithic multi-wavelength emission diode lasers, such as changing active layer

composition [Saka82, Boua82], grating period variations [Dutt86, Aiki76], stripe width related modal loss control [Toku86] and material desorption technique [Eple90]. The associated techniques for most of these approaches are either low yield and non-reliable or complicated and time consuming. Previously, we have mentioned that contact reflectivity has a great effect on the thin p-clad SQW diode lasers [Wu94b]. One of the important characteristics is that, by selecting shiny or less shiny contact metal, one can control the lasing wavelength of diode laser on either the first or the second energy level of a single quantum well active layer. Based on this concept, the process of fabricating dual wavelength emitting diode lasers should be much simpler and more reliable than the other approaches as stated above.

Diode lasers with epi-side up bonding have less diffraction noise and better lasing beam quality than diode lasers with epi-side down bonding. In the epi-side up bonding configuration, however, thermal resistance reduction becomes an important problem. Since the heat sink is far away ($\sim 100 \mu\text{m}$) from the active region, heat generated inside the active region flowing through the cap layer becomes an effective heat dissipation path for diode laser operation. Theoretical study [Joyc75] has shown that the thermal resistance of diode lasers can be reduced effectively by depositing a thick Au layer as the heat spreader on the top laser. Based on this concept, a thick Au plating technique was developed and

applied to the devices fabricated to show the reduction of thermal resistance and performance improvements.

In designing thin p-clad InGaAs lasers, the p^+ -GaAs cap layer thickness has to be determined with care in order to avoid the possible increase of modal loss from the cap layer. This is because the refractive index value of the cap layer is very close to that of the quantum well region at the lasing wavelength. In this case, due to the short separation between the quantum well and the p^+ -GaAs cap layer, a thick cap layer allows the lasing mode to penetrate through the thin p-cladding layer and couple into the p-cap layer forming a twin-guide laser structure [Suem75]. As a result, more modal loss will be generated and poor diode laser performance obtained. Additionally, due to the smaller optical confinement of lasing mode caused by the thick (200 nm) p^+ -cap layer, microsecond-long lasing delays are observed on 50- μ m stripe width lasers [Wu96a].

Although thick p^+ -cap layer, thin p-clad lasers appear not to be useful, the insertion of a thick p^+ -cap section into a thin p^+ -cap layer laser may have practical applications. The combination of one or more 100 nm p^+ -cap layer sections as the electron pumped sections and a 200 nm p^+ -cap layer section as the surface sensitive section in one laser structure makes a "surface sensitive" diode laser [Wu96b] which may prove useful in sensor applications.

This dissertation is organized as follows: Chapter 2 shows the details of contact reflectivity effects on the thin

p-clad diode lasers. Both the theoretical calculations of QW modal gain, modal loss and experimental results are described. Chapter 3 presents the theoretical calculations and the experimental results of ridge-guided thin p-clad diode lasers. The comparison between thin p-clad and thick p-clad diode lasers are also included. Chapter 4 states the fabrication process and the experimental results of dual wavelength diode lasers made from a thin p-clad laser structure. In addition, the details of a thick Au plating heat spreader technique developed to show diode laser thermal resistance improvements are described. Chapter 5 outlines the influence of p⁺-GaAs cap layer thickness on the thin p-clad diode laser performance. Chapter 6 describes the details of theoretical and experimental work on surface sensitive laser diodes (SSLD) based on the thin p-clad laser structure with both 100 nm and 200 nm p⁺-cap layers. Finally, the conclusion and recommendations for future study are presented in Chapter 7.

CHAPTER 2

CONTACT REFLECTIVITY EFFECTS ON THIN P-CLAD InGaAs SINGLE QUANTUM WELL LASERS

2.1 Introduction

In this chapter we show how the performance of shiny contact, InGaAs single quantum well (SQW) lasers is changed when the contact metal is changed from shiny gold to less shiny nickel. In addition to the expected difference in threshold current and slope efficiency, operating wavelength differences of more than 50 nm are observed [Wu94] for cavity lengths between 250 and 700 microns. At shorter (gold) and longer (nickel) cavity lengths, large shifts in operating wavelength are observed. In Section 2.2, the laser material used is described. Additionally, theoretical calculations of the quantum well laser modal gain and the modal loss induced by the different contact metal are outlined. In Section 2.3, the experimental results of thin p-clad diode lasers with shiny gold (Au) and less shiny nickel (Ni) fabricated are shown and compared with the theoretical calculations. Also presented are the changes of diode laser performance under various annealing time and constant annealing temperature.

Diode lasers with and without facet coating are life-time tested to evaluate the reliability of these thin p-clad lasers.

2.2 Laser Material and Theoretical Calculations

Figure 2.1 shows the diode laser structure used in this study which consists of a 250 nm n^+ -GaAs buffer layer grown on a n^+ -GaAs substrate, a 70 nm $\text{Al}_x\text{Ga}_{1-x}\text{As}$ graded layer ($x=0.05-0.6$), a 1400 nm n -type $\text{Al}_{0.6}\text{Ga}_{0.4}\text{As}$ cladding layer, a 200 nm graded $\text{Al}_y\text{Ga}_{1-y}\text{As}$ (undoped) barrier layer ($y=0.3-0.6$), an active layer of 10 nm $\text{In}_z\text{Ga}_{1-z}\text{As}$ ($z\sim 0.15$) undoped strained quantum well centered in a pair of 7 nm GaAs bounding layers, a 200 nm graded $\text{Al}_y\text{Ga}_{1-y}\text{As}$ (undoped) barrier layer ($y=0.6-0.3$), a 250 nm p - $\text{Al}_{0.6}\text{Ga}_{0.4}\text{As}$ cladding layer, a 25 nm $\text{Al}_x\text{Ga}_{1-x}\text{As}$ graded layer ($x=0.6-0.05$) and a 100 nm p^+ -GaAs contact layer. As can be seen the p-cladding layer is only 250 nm and is much thinner than those of conventional laser devices ($>1.0\text{ }\mu\text{m}$).

Since the total thickness of the epitaxial layers above the quantum well in this structure is only $\sim 600\text{ nm}$, the type of metallization used on the p^+ -contact layer is expected to be important in determining the mode loss coefficient α_i [Luo90]. To understand the effect of p-contact metal on the diode laser loss coefficient (α_i), the α_i values for the laser structure shown in Figure 2.1 have to be calculated.

To do the computations of α_1 , the lasing wavelength is determined first. In computing the lasing wavelength of the laser structure, the energy gap shift due to the presence of biaxial strain induced by the lattice mismatched-material InGaAs/GaAs has to be calculated. The strained effects can be divided into two components: hydrostatic component and shear component [Van89]. Under the hydrostatic strain effect both the conduction band edge and the valence band edge will move up by ΔE_c and ΔE_v eV as referenced from the corresponding bulk material band edge. The energy gap change ΔE_g due to hydrostatic strain effect is obtained from the following equations [Van89]:

$$\Delta E_g = \Delta E_c - \Delta E_v \quad (2.2.1)$$

$$\Delta E_c = a_c * \frac{\Delta\Omega}{\Omega} \quad (2.2.2)$$

$$\Delta E_v = a_v * \frac{\Delta\Omega}{\Omega} \quad (2.2.3)$$

$$\frac{\Delta\Omega}{\Omega} = \epsilon_{xx} + \epsilon_{yy} + \epsilon_{zz} = 2 * \left(\frac{a_s - a_o}{a_o} \right) * \left(1 - \frac{C_{12}}{C_{11}} \right) \quad (2.2.4)$$

where

a_c, a_v : hydrostatic deformation potential for the conduction band and valence band

$\frac{\Delta\Omega}{\Omega}$: fractional volume change due to strain effect

$\epsilon_{xx}, \epsilon_{yy}, \epsilon_{zz}$: diagonal components of the strain tensors

a_s, a_o : lattice parameter for the barrier (GaAs) and quantum well ($\text{In}_x\text{Ga}_{1-x}\text{As}$)
 C_{11}, C_{12} : elastic stiffness coefficient

Since the exact value of either the hydrostatic deformation potential or the elastic stiffness coefficients of the ternary material $\text{In}_x\text{Ga}_{1-x}\text{As}$ has not yet been determined, in this study we assume that both parameters can be expressed as the combination of those of InAs and GaAs. In other words, a_c, a_v, C_{11} and C_{22} for the $\text{In}_x\text{Ga}_{1-x}\text{As}$ can be expressed as:

$$a_i = (1 - x) * a_i(\text{GaAs}) + x * a_i(\text{InAs}) \quad i=c, v \quad (2.2.5)$$

$$C_{1j} = (1 - x) * C_{1j}(\text{GaAs}) + x * C_{1j}(\text{InAs}) \quad j=1, 2 \quad (2.2.6)$$

Under the shear component of strain effects the valence band edge will become degenerated and split into heavy-hole band edge and light-hole band edge. The separation between heavy-hole band edge and light-hole band edge is derived from the equations as shown below:

$$S = 2 * \delta\epsilon_s * (1 - \frac{\delta\epsilon_s}{\Delta}) \quad (2.2.7)$$

$$\delta\epsilon_s = b * \frac{a_s - a_o}{a_o} * (1 + 2 * \frac{C_{12}}{C_{11}}) \quad (2.2.8)$$

$$b = (1 - x) * b(\text{GaAs}) + x * b(\text{InAs}) \quad (2.2.9)$$

$$\Delta = (1 - x) * \Delta(\text{GaAs}) + x * \Delta(\text{InAs}) \quad (2.2.10)$$

where

S: bandedge split energy between heavy hole and light hole

$\delta\epsilon_a$: heavy hole splitting energy

b: uniaxial deformation potential

Δ : split orbit energy

The lattice constant of $\text{In}_x\text{Ga}_{1-x}\text{As}$ and GaAs can be expressed as $a_0(x) = (5.6533 + 0.405 \cdot x) \text{ \AA}$ and $a_0 = 5.6533 \text{ \AA}$, respectively [Corz93]. As referenced from data shown in Van de walle [Van89], one can calculate the total energy gap shift caused by the hydrostatic and shear components of strain by substituting the related parameters into equation (2.2.1) to equation (2.2.10). Figure 2.2 shows the schematic diagram of bandgap lineup for $\text{In}_{0.15}\text{Ga}_{0.85}\text{As}/\text{GaAs}$ quantum well structure, where strain-induced bandedge split energy S between the heavy hole and the light hole, and the heavy hole energy bandgap $E_g(\text{HH})$ are computed as $S = 63.9 \text{ meV}$ and $E_g(\text{HH}) = 1253.3 \text{ meV}$. A conduction band offset ratio of 0.55 is also assumed [Cole93] to compute the conduction band energy barrier, heavy hole valence band energy barrier and light hole valence band energy barrier as 93.9 meV, 76.8 meV and 12.9 meV, respectively. The energy state distribution of the InGaAs/GaAs quantum well structure is calculated by solving the Schrodinger equation [Bast88], in which a square well structure with finite barrier height is assumed. The effective masses used for the electron, heavy hole and light hole in the InGaAs quantum well are $0.0599 m_0$, $0.4395 m_0$ and $0.0847 m_0$ respectively [Pan88], where m_0 is the electron rest mass. For the conduction band, the energy states inside the

100 Å $\text{In}_{0.15}\text{Ga}_{0.85}\text{As}$ quantum well are calculated as $E_{c1}=22.9$ meV and $E_{c2}=62.9$ meV (referenced from the conduction bandedge). For the valence band, there are four heavy hole energy states: $E_{vh1}=6$ meV, $E_{vh2}=23.8$ meV, $E_{vh3}=52.2$ meV and $E_{vh4}=86.8$ meV, and one light hole energy state: $E_{vl1}=82.5$ meV (referenced from the heavy hole band edge) inside the quantum well. According to the results of the computations, a lasing wavelength of ~960 nm is obtained for this InGaAs SQW diode laser and used for the following computations.

The modal loss induced by both shiny Au and less shiny Ni contacts are calculated from Modeig program [Deme89]. The refractive indices of Au and Ni at this wavelength are interpolated from [Weas87] as 0.091-i6.03 and 2.75-i4.87, respectively. The corresponding optical constants of each layer of the diode laser structure are obtained [Taka78], [Adac85]. Only the fundamental mode is considered from the calculated results in which the highest effective refractive index value of the diode structure is found. Figure 2.3 shows the dependence of the calculated mode loss α_1 on the thickness of the p-cladding layer when Au and Ni p-contact metals are used. From this plot, we can see as the p-clad layer thickness is reduced below 400 nm, the optical mode loss for the Ni contact lasers increases rapidly whereas that for the Au contact remains relatively flat. In other words, Au contacts are shiny compared to Ni contacts. At 250 nm p-cladding layer thickness, the calculated mode loss of diode

laser with Au and Ni metal contact is $\alpha_i(\text{Au})=3 \text{ cm}^{-1}$ and $\alpha_i(\text{Ni})=70 \text{ cm}^{-1}$, respectively. Since the threshold mode gain G_{th} is proportional to the modal loss of diode lasers, the larger modal loss induced by the Ni contact indicates that Ni contact lasers should have higher G_{th} than those of Au contact lasers. The magnitude of the increase in G_{th} required for lasing when using Ni rather than Au is given by [Chin88]

$$G_{\text{th}} = \Gamma g_{\text{th}} = \alpha_i + \frac{1}{L} \ln \frac{1}{R} \quad (2.2.11)$$

where Γ is the optical confinement factor, g_{th} is the threshold gain in the quantum well, L is the cavity length of diode laser and R is the mode reflectivity at the facets.

As stated earlier, for L in the range from 250 to 700 μm , the Ni and Au thin p-clad devices differ in operating wavelength by more than 50 nm. In order to understand this effect, it is necessary to calculate the spectral gain function $g(h\nu)$ [Chin88] as well as threshold spectral gain g_{th} for these two different optical mode loss devices.

Since the energy state distributions in the QW structure have been determined, the carrier density required for obtaining a given quasi-Fermi level can be calculated. In the computations, a parabolic subband model is used for conduction band, heavy hole valence band and light hole valence band. For the conduction band, the electron concentration is denoted [Corz93] as

$$\begin{aligned}
N &= 2 \int_{E_c}^{\infty} \rho^{2D}(E - E_c) * f_c * dE \\
&= \frac{m_c * k_B * T}{\pi * \hbar^2 * L_z} \sum_n \ln[1 + \exp\{-(E_{cn} - E_{fc}) / k_B * T\}]
\end{aligned}
\tag{2.2.12}$$

where

$\rho^{2D}(E-E_c)$: density of states in the quantum well

f_c : Fermi-Dirac distribution for electrons in the conduction band

m_c : effective mass of electron in the conduction band

k_B : Boltzmann's constant

E_{cn} : quantized energy level of electron in the conduction band

E_{fc} : quasi-Fermi level in the conduction band

L_z : quantum well thickness

\hbar : reduced Planck constant

For the valence band, the hole concentration is the summation of light hole concentration and heavy hole concentration, and can be expressed as [Corz93]

$P=P_h+P_l$ and

$$P_h = \frac{m_h * k_B * T}{\pi * \hbar^2 * L_z} \sum_{n_h} \{ \ln[1 + \exp(\frac{E_{vn_h} - E_{fv}}{k_B * T})] \}
\tag{2.2.13}$$

$$P_l = \frac{m_l * k_B * T}{\pi * \hbar^2 * L_z} \sum_{n_l} \{ \ln[1 + \exp(\frac{E_{vn_l} - E_{fv}}{k_B * T})] \}
\tag{2.2.14}$$

where m_h , m_l : effective mass of heavy hole and light hole; n_h , n_l : quantum state number of heavy hole and light hole in the valence band; $E_{v n_h}$, $E_{v n_l}$: quantum state energy for heavy hole and light hole in the valence band; E_{fv} : quasi-Fermi level in the valence band.

By using equations (2.2.12), (2.2.13), (2.2.14) and the quantum state energy inside the quantum well, one can get the relationship between the quasi-Fermi level E_{fc} , E_{fv} and the corresponding carrier density in the conduction band and valence band.

In semiconductor the optical gain caused by the photon-induced transitions of electrons from conduction band to valence band is defined as the fractional increase in photons per unit length

$$g \equiv \frac{1}{\Phi} \frac{d\Phi}{dz} = W_{c \rightarrow v} - W_{v \rightarrow c} \quad (2.2.15)$$

and can be written as [Corz93]

$$g(h\nu) = \left(\frac{1}{h\nu}\right) \frac{\pi e^2 \hbar}{\epsilon_0 c m_0^2 n} \frac{\bar{n}_g}{\bar{n}} |M_T|^2 \rho_{red}(f_c - f_v) \quad (2.2.16)$$

where F is the photon flux (unit; $s^{-1}cm^{-2}$); $W_{c \rightarrow v}$, $W_{v \rightarrow c}$: total transition rate from conduction band to valence band and from valence band to conduction band, respectively; \bar{n}_g , \bar{n} : group refraction index and refraction index of the crystal; $|M_T|^2$: transition matrix element; ρ_{red} : reduced density of state; f_c ,

f_v : Fermi-Dirac distribution for electrons in the conduction band and valence band. In the calculations, we assume the difference between \bar{n}_q and \bar{n} can be neglected.

Considering the TE polarized transition, \mathbf{k} -selection rule and ignoring the forbidden transition, the transition matrix element can be expressed as

$$|M_{\Gamma}|^2_{\Gamma\nu n_z} = S_{\Gamma\nu n_z}^{\text{TE}} |M|^2 < F_{\nu n_z} | F_{\Gamma n_z} > = S_{\Gamma\nu n_z}^{\text{TE}} |M|^2 \quad (2.2.17)$$

where

$$S_{\Gamma\nu n_z}^{\text{TE}} = S_{\Gamma h n_z}^{\text{TE}} = \frac{1}{2} (1 + \cos^2 \theta_{n_z}) \quad \text{for e-hh transition} \quad (2.2.18)$$

$$S_{\Gamma\nu n_z}^{\text{TE}} = S_{\Gamma l n_z}^{\text{TE}} = \frac{1}{6} (5 - 3 \cos^2 \theta_{n_z}) \quad \text{for e-lh transition} \quad (2.2.19)$$

$$\cos^2 \theta_{n_z} = \frac{\Delta E_{\Gamma n_z} + \Delta E_{\nu n_z}}{h\nu - E_q} \quad (2.2.20)$$

$$\rho_{\text{red}, l} = \frac{m_{r, l}}{2\pi\hbar^2} \frac{1}{L_z} \quad i=h \text{ for e-hh transition}; \quad (2.2.21)$$

$$\frac{1}{m_{r, l}} = \frac{1}{m_c} + \frac{1}{m_l} \quad i=l \text{ for e-lh transition}. \quad (2.2.22)$$

$\Delta E_{\Gamma n_z}$: energy difference between the electron energy state and the conduction bandedge E_c .

$\Delta E_{\nu n_z}$: energy difference between the heavy hole energy state and the heavy hole bandedge or between the light hole energy state and the light hole bandedge.

For the $\text{In}_x\text{Ga}_{1-x}\text{As}$ quantum well, $|M|^2$ term in equation (2.2.17) can be written as [Corz93]

$$|M|^2 = \frac{m_0}{2} (28.8 - 6.6 * x) \quad (2.2.23)$$

By ignoring intraband relaxation [Garb93], the total optical gain is then calculated from equation (2.2.16) to equation (2.2.23) as the summation of optical gain due to e-hh transitions and e-lh transitions. Figure 2.4 shows the dependence of spectra gain on photon energy for the diode laser structure shown in Figure 2.1, where the injected carrier density is assumed at $N=2.5 \times 10^{18} \text{ cm}^{-3}$ and $5.5 \times 10^{18} \text{ cm}^{-3}$. It is evident in Figure 2.4 that the photon energies at peak gain for the two carrier densities are considerably different. At $2.5 \times 10^{18} \text{ cm}^{-3}$ injection carrier density, the peak gain occurs at an energy corresponding to the band edge transition energy from $n=1$ conduction band electrons to $n=1$ heavy holes, $E_{11} \sim 1286 \text{ meV}$. When the injection carrier density increases to $5.1 \times 10^{18} \text{ cm}^{-3}$, the peak gain is the same at E_{11} and E_{22} (the band edge transition energy from $n=2$ conduction band electrons to $n=2$ heavy holes, $E_{22} \sim 1364 \text{ meV}$). Above $5.1 \times 10^{18} \text{ cm}^{-3}$, the gain peak occurs at E_{22} . The g_{th} values shown in Figure 2.4 are calculated from equation (2.2.11) using the α_i values from Figure 2.3, a confinement factor $\Gamma=0.02$, mode reflectivity $R=0.31$ [Lee91] and cavity length $L=380 \text{ }\mu\text{m}$. It is clear that the increase in g_{th} required by the extra mode loss due to the Ni contact can cause a large shift in lasing wavelength.

2.3. Experimental Results and Discussion

In order to fabricate wide-stripe lasers, 50 μm stripes on 500 μm centers are defined on the $\text{p}^+\text{-GaAs}$ contact layer using standard photolithography techniques. Mesas and current blocking oxide layer are formed using a pulsed anodic oxidation technique [Gro94]. Usually the oxidation time is ~6 minutes (with anodic oxidation current density $J \sim 100 \text{ mA/cm}^2$, repetition rate = 50 Hz and pulse width = 700 μsec) to remove the $\text{p}^+\text{-GaAs}$ cap layer and part of the p-cladding layer to reduce the diode current spreading effect. After the oxidation process, wafers are cleaned and covered with new photoresist to protect the epilayer surface for the following wafer thinning process. This wafer surface protection step is important for making good adhesion shiny contact for the diode lasers. The wafers are thinned to about 100 μm , a metallurgy of $\text{Ge}(20 \text{ nm})/\text{Au}(40 \text{ nm})/\text{Ni}(20 \text{ nm})/\text{Au}(15 \text{ nm})$ is evaporated sequentially on the substrate side and annealed at 430 C for 5 minutes to obtain the n-type ohmic contact. A non-alloyed $\text{Au}(80 \text{ nm})/\text{Ni}(50 \text{ nm})/\text{Au}(50 \text{ nm})$ or $\text{Ni}(80 \text{ nm})/\text{Au}(50 \text{ nm})$ is evaporated as the shiny or less shiny p-contact respectively. Then, another non-alloyed $\text{Ni}(25 \text{ nm})/\text{Au}(50 \text{ nm})$ is deposited on the subtract side to improve the metal contact conductivity. Diode lasers with 500 μm wide and cavity lengths ranging from 120 μm to 1200 μm are cleaved, soldered on copper blocks by using either indium soldering or

sliver epoxy (1 part Ag epoxy + 1 part thinner and cured at 150 C for ~5 minutes) and characterized.

The measured emission spectrum of Au and Ni lasers with $L=380\text{ }\mu\text{m}$ is shown in Figure 2.5. The difference in operating wavelength is ~52 nm, in good agreement with the predicted difference of ~55 nm shown in Figure 2.4. The corresponding pulsed output power versus input current characteristics are shown in Figure 2.6. Threshold current and total slope efficiency for these two lasers are $I_{th}(\text{Au})=60\text{ mA}$, $\eta_s(\text{Au})=0.76\text{ mW/mA}$ and $I_{th}(\text{Ni})=240\text{ mA}$, $\eta_s(\text{Ni})=0.41\text{ mW/mA}$ respectively. In addition, from measured inverse slope efficiency versus cavity length plots, the internal mode loss for Au-contact lasers and Ni-contact lasers are $\alpha_i(\text{Au})=8\text{ cm}^{-1}$ and $\alpha_i(\text{Ni})=51\text{ cm}^{-1}$ respectively. These are to be compared with the calculated values from Figure 2.3, $\alpha_i(\text{Au})=3\text{ cm}^{-1}$ and $\alpha_i(\text{Ni})=70\text{ cm}^{-1}$. The difference of 5 cm^{-1} in $\alpha_i(\text{Au})$ and 19 cm^{-1} in $\alpha_i(\text{Ni})$ can be explained if the complex refractive index of the Au, $n(\text{Au})$, and the complex refractive index of the Ni, $n(\text{Ni})$, used in our experiments are somewhat different from the values interpolated from [Weas87]. For example, if $n(\text{Au})$ is changed from $0.091-i6.03$ to $0.16-i4.08$, $\alpha_i(\text{Au})$ changes from 3 cm^{-1} to measured value of 8 cm^{-1} . On the other hand, if $n(\text{Ni})$ is changed from $2.75-i4.87$ to $2.30-i5.25$, $\alpha_i(\text{Ni})$ changes from 70 cm^{-1} to the measured value of 51 cm^{-1} . We believe that

variations in both $n(\text{Au})$ and $n(\text{Ni})$ of these magnitudes are possible since it is known that refractive index values can be strongly dependent on the details of the deposition process.

In the previous section, it is mentioned that transition E_{11} and E_{22} have the same peak spectral gain at a carrier density of $5.1 \times 10^{18} \text{ cm}^{-3}$. This implies that lasers requiring this carrier density to lase should operate simultaneously at two wavelengths about 50 nm apart [Zory86]. It is clear from equation (2.2.11) that it should be possible, in principle, to change cavity length L to achieve this condition for both Au and Ni contact lasers ($L > 380 \text{ } \mu\text{m}$ for Ni lasers and $L < 380 \text{ } \mu\text{m}$ for Au lasers). In order to check this prediction, the emission wavelengths of both laser types are measured as a function of L . As shown in Figure 2.7, the emission wavelength jumps occur for the Ni lasers at $L \sim 900 \text{ } \mu\text{m}$ and at $L \sim 200 \text{ } \mu\text{m}$ for the Au lasers. Similar wavelength jumps have been observed for thick p-clad 7.5 nm InGaAs SQW lasers when their stripe widths are reduced from 50 to 15 microns [Shie89] or thick p-clad 15 nm InGaAs SQW lasers with 25 μm stripe widths when their active region temperature is increased due to current [Beer91a]. Using the above L values in equation (2.2.11) along with the measured values of α_1 discussed above and $R=0.31$, we find that $G_{\text{th}}=66.5 \text{ cm}^{-1}$ for 200 μm long Au contact lasers and $G_{\text{th}}=64 \text{ cm}^{-1}$ for 900 μm long Ni contact lasers, in close agreement as expected. The blue shift of the spectral peaks accompanied with the decrease of

cavity length shown by the dashed lines in Figure 2.7 is mainly due to band-filling modified by bandgap renormalization [Chin88].

So far we have shown that the reflectivity of p-contact metal is important in determining the performance of thin p-clad diode lasers, we are interested in understanding the effects of annealing p-contact metal on the thin p-clad diode laser. To check this point, thin p-clad diode lasers with shiny Au contact are annealed at 320 C for different annealing time: 30, 60, 120, 180 and 300 seconds. The variations of threshold current and total slope efficiency as a function of annealing time are shown in Figure 2.8. As can be seen from this plot, threshold current increases rapidly as the annealing time increases upto 120 seconds and then becomes saturated when diodes are annealed further longer. Additionally, the total slope efficiency decreases gradually from 0.8 mW/mA(0 second) to ~0.5 mW/mA(120 seconds) and remains constant as annealing time increases further. The deterioration of diode laser performance can be explained by the decrease of contact reflectivity caused by the reactions of Au and GaAs at 320 C. This interaction will make the Au contact become less shiny. As the annealing time increases further, the interactions may saturate and cause the contact reflectivity keep constant. Consequently, even at low temperature (320 C), the annealing effect can decrease the contact reflectivity and diode laser performance. To have

good thin p-clad diode laser behavior, the shiny Au contact should not be annealed.

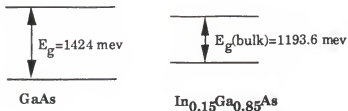
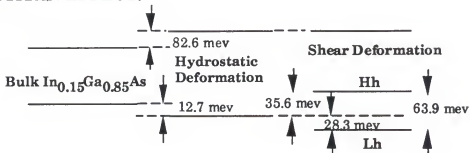
To further evaluate shiny contact thin p-clad diode lasers, samples without and with facet coatings are CW lifetime tested at 20 C with output power 50 mW/facet (w/o coating) and 100 mW (w/ coating), respectively, where both samples are packaged with p-side up configuration. The coated sample is prepared by depositing a thickness of $\lambda/4n$ Al_2O_3 on the emitting facet as the anti-reflection (AR) coating layer and $\text{Al}_2\text{O}_3(\lambda/4n)/\text{Al}(100 \text{ nm})/\text{Al}_2\text{O}_3(\lambda/4n)$ on the reflective facet as the high reflector (HR) where n is the refractive index of the active region at the lasing wavelength. Figure 2.9 and Figure 2.10 show the output power P versus input current I characteristics and the corresponding variations of threshold current and total slope efficiency of diode laser without facet coating after t hours lifetime test. Similar results of the coated sample are shown in Figure 2.11 and Figure 2.12. For the uncoated sample, threshold current increases from the initial value of 42 mA to ~56 mA and the total slope efficiency almost keeps constant at 0.65 mW/mA for the first 500 hours lifetime test and gradually decreases to ~0.57 mW/mA after 1057 hours lifetime test. For the coated sample, threshold current increases quicker than that of uncoated sample from the initial value of 40 mA to ~65 mA. In addition, the slope efficiency decreases faster than that of the uncoated sample from 0.62 mW/mA to ~0.41 mW/mA after 1050

hours lifetime test. The possible reason for the big difference of I_{th} and η_s between both diode lasers could be due to the cavity length difference where the uncoated sample is 600 μm long while that of the coated sample is only 450 μm . Since diode laser with longer cavity length is believed to have better lifetime performance than that of diode laser with shorter cavity length, especially for the high output power condition. From the results of lifetime test, we have successfully demonstrated that thin p-clad diode lasers can "live" for long time CW operation. Further applications from this thin p-clad laser structure could be possible as the fabrication process is improved and optimized.

In summary, we have demonstrated that the reflectivity of p-contact has a significant effect on the performance of thin p-clad diode lasers. Decreasing the reflectivity of the p-contact metal increases optical mode loss, which increases threshold current, decreases slope efficiency and shifts the emission wavelength. The more than 50 nm wavelength difference between the thin p-clad diode lasers with different p-contact metallurgy can be explained quantitatively by superimposing the threshold gain required for lasing in each case with the corresponding spectral gain curve calculated using standard QW laser theory.

p^+ -GaAs contact layer: 100 nm
$p\text{-Al}_z\text{Ga}_{1-z}\text{As}$ ($z=0.6 - 0.05$): 25 nm
$p\text{-Al}_{0.6}\text{Ga}_{0.4}\text{As}$ cladding layer: 250 nm
$\text{Al}_x\text{Ga}_{1-x}\text{As}$ ($x=0.3 - 0.6$): 200 nm
GaAs: 7 nm
$\text{In}_y\text{Ga}_{1-y}\text{As}$ SQW ($y\sim 0.15$): 10 nm
GaAs: 7 nm
$\text{Al}_x\text{Ga}_{1-x}\text{As}$ ($x=0.6 - 0.3$): 200 nm
$n\text{-Al}_{0.6}\text{Ga}_{0.4}\text{As}$ cladding layer: 1400 nm
$n\text{-Al}_z\text{Ga}_{1-z}\text{As}$ ($z=0.05\text{-}0.6$): 25 nm
n-GaAs substrate

Figure 2.1 Thin p-clad InGaAs single quantum well diode structure used in the contact reflectivity effect study.

BULK MATERIAL:**STRAIN EFFECT:****BAND LINEUP UNDER STRAIN EFFECT:**

(Assume conduction band energy offset ratio = 0.55)

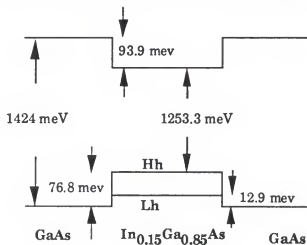


Figure 2.2 Schematic diagram of bandgap lineup between the strained InGaAs quantum well and GaAs barrier layers of the diode laser structure shown in Figure 2.1.

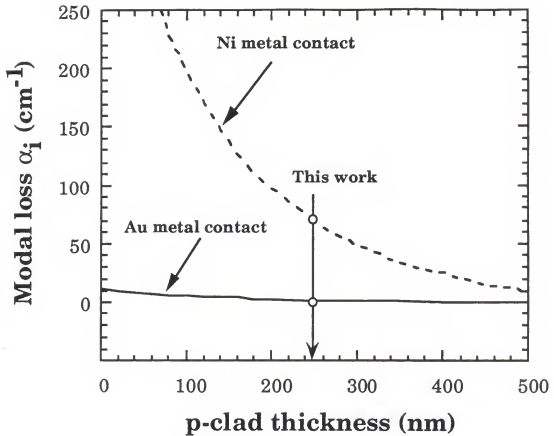


Figure 2.3 The calculated relationship between the optical mode loss and p-clad thickness for the InGaAs single quantum well (SQW) laser structure shown in Figure 2.1.

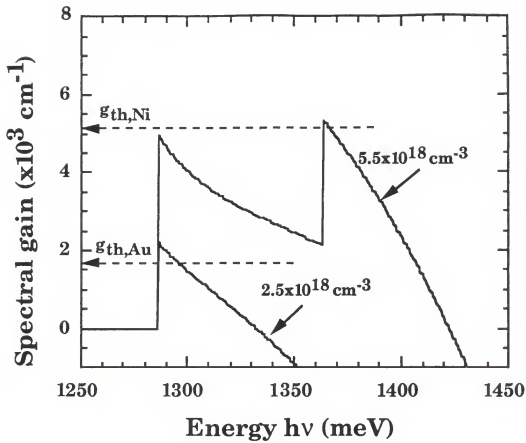


Figure 2.4 The dependence of spectral gain on photon energy for a 100 Å $\text{In}_{0.15}\text{Ga}_{0.85}\text{As}/\text{GaAs}$ structure at two carrier densities. The two dashed lines are the active layer threshold gains for thin (0.25 μm) p-clad InGaAs SQW lasers with Ni or Au contact metal.

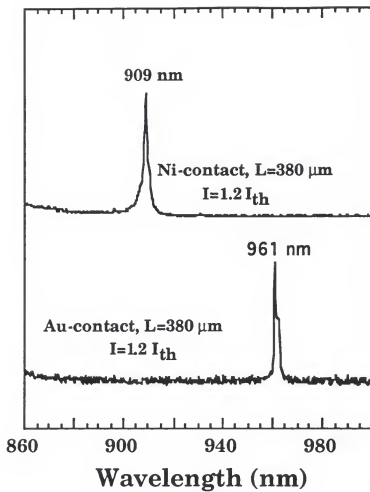


Figure 2.5 Measured lasing wavelengths of thin (0.25 μm) p-clad InGaAs SQW diode lasers with different p contact metals.

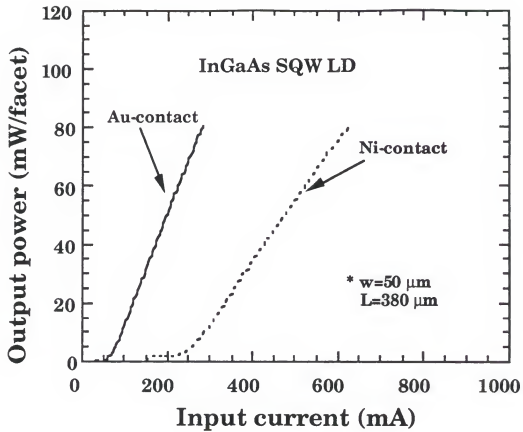


Figure 2.6 Measured pulsed output power versus input current characteristics of thin p-clad InGaAs SQW diode lasers with Au contact or Ni contact.

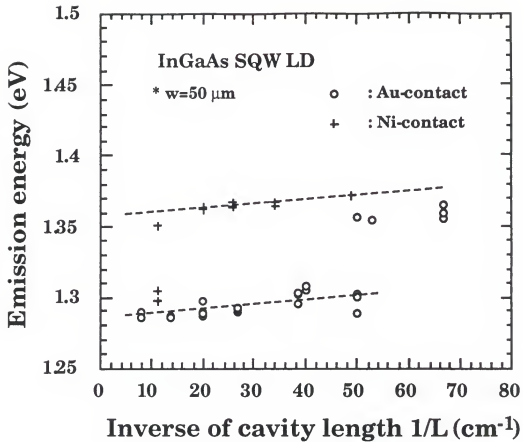


Figure 2.7 Spectral position of peak lasing energy as a function of reciprocal cavity length of thin p-clad InGaAs SQW diode lasers using Au or Ni as the p-type contact. (Each mark represents an individual laser.)

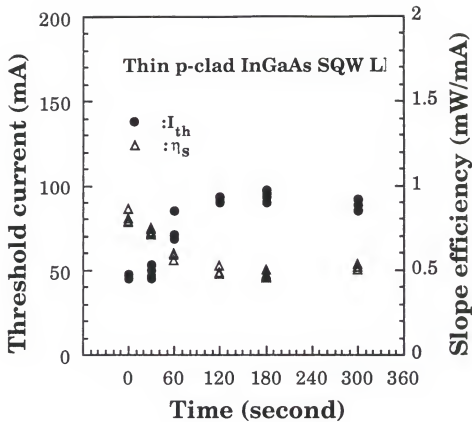


Figure 2.8 The variations of threshold current (I_{th}) and total slope efficiency (η_s) of thin p-clad diode lasers as a function of p-contact metal annealing time, where the annealing temperature is set at constant 320 C.

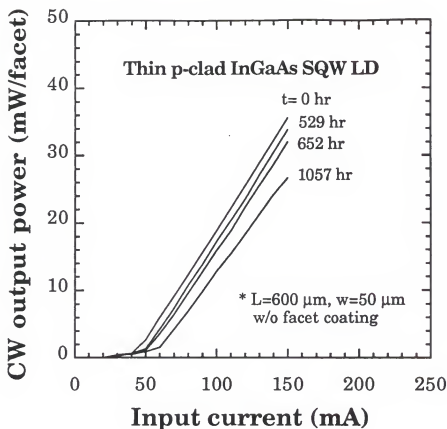


Figure 2.9 Measured CW output power versus input current characteristics of Au-contact thin p-clad InGaAs SQW diode laser after $t=0$, 529 and 1057 hrs lifetime test, where the output power is set constant CW 50 mW/facet during the lifetime test.

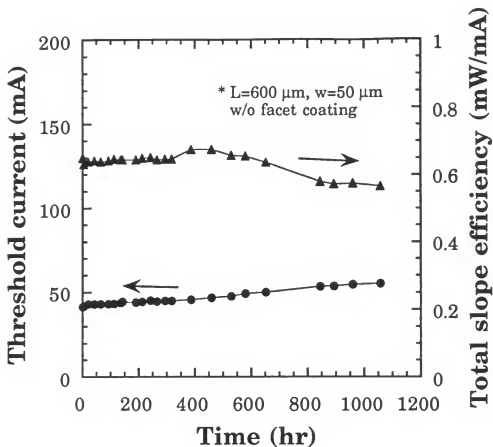


Figure 2.10 The variations of threshold current and total slope efficiency of Au-contact, thin p-clad InGaAs SQW diode laser as a function of lifetime test period when operated with constant output power CW 50 mW/facet.

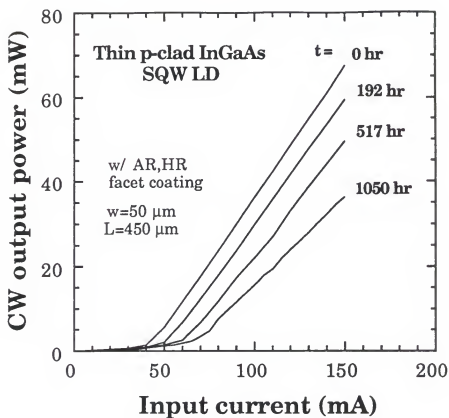


Figure 2.11 Measured CW output power versus input current characteristics of Au-contact thin p-clad InGaAs SQW diode laser after $t=0$, 192, 517 and 1050 hr. lifetime test, where sample is with AR and HR facet coating and output power is set constant CW 100 mW during the lifetime test.

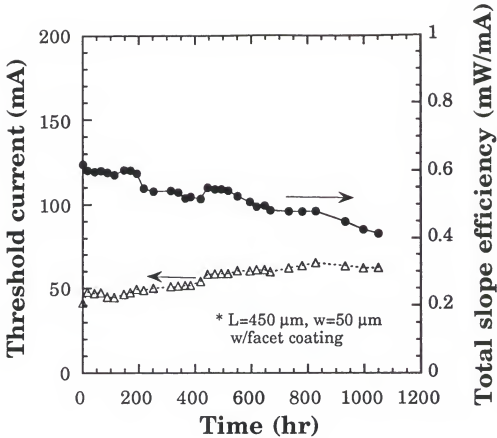


Figure 2.12 The variations of threshold current and total slope efficiency of Au-contact thin p-clad InGaAs SQW diode laser as a function of CW 100 mW constant output power lifetime test period, where sample is with AR and HR facet coating.

CHAPTER 3

THIN P-CLAD RIDGE-GUIDED DIODE LASERS

3.1 Introduction

In chapter 2 we have demonstrated the important effects of p-metal contact reflectivity on the thin p-clad diode laser performance. In this chapter, a new and simple method of fabricating ridge-guided diode laser from a thin p-clad structure is proposed and demonstrated. The major advantage of using a thin p-clad diode laser structure instead of the conventional thick p-clad structure for fabricating ridge-guided diode lasers is that only a small part of outside stripe material is required to remove for providing a strong waveguiding. This will make the device fabrication process become simple and economical. Moreover, we have found that these low-ridge, thin p-clad lasers can operate in a single lateral mode with cw performance characteristics similar to those reported for InGaAs SQW lasers fabricated from conventional epitaxial material in a high-ridge configuration [Fisc87, Bour90, Take90]. In other words, thin p-clad diode laser with low ridge height structure can provide strong

waveguiding for diode lasers operating with low threshold current (I_{th}) and high slope efficiency (η_s). This is totally different from those of thick p-clad diode laser structure in which the threshold current of an InGaAs single quantum well (SQW) diode laser is very high (> 100 mA) when fabricated in either a low-ridge [Shie89] or oxide-defined [Beer91b], narrow-stripe configuration.

In Section 3.2, the main design principle responsible for low threshold, single lateral mode lasing is discussed. In Section 3.3, the procedure for fabricating ridged-guided, thin p-clad lasers using pulsed anodic oxidation [Gro94] is outlined. The results of pulsed characterization measurements on these lasers are presented in Section 3.4 and compared with measured values reported for thick p-clad lasers [Shie89, Beer91b]. In Section 3.5, the cw performance characteristics of 5 micron wide, low-ridge, thin p-clad lasers are presented and compared with those of reported thick p-clad, high-ridge waveguide lasers [Fisc87, Bour90, Take90]. In Section 3.6, the dependence of diode laser performance on the ridge height is presented and comparisons are made between thin and thick p-clad ridge-guided lasers with various ridge heights.

3.2 Theoretical Calculations

The thin p-clad diode laser structure used in this study is the same as that stated in previous chapter (as shown in

Figure 2.1). Since the thickness of the p-clad layer is only 250 nm, the behavior of ridge waveguide lasers fabricated from this material should be quite different from that of ridgeguide lasers with the same ridge height fabricated from conventional material with thick p-clad layers (> 1000 nm). The parameter normally used in designing ridgeguide lasers is Δn , the difference in effective refractive index (lateral index step) between the ridge region and the outside-ridge region [Agra84]. Consequently, it is of interest to calculate Δn as a function of ridge height (the amount of epitaxial material removed in defining the ridge) for thick and thin p-clad configurations. In the calculations, it is assumed that the p^+ -GaAs contact layer, the $p\text{-Al}_x\text{Ga}_{1-x}\text{As}$ graded-layer and part of the p-clad layer of the outside-ridge region are removed and replaced with a native oxide, the whole structure being covered with Au. A lasing wavelength of 960 nm, an oxide refractive index of 1.8 and a Au refractive index of $0.091 - i6.03$ are also assumed in the computations. The optical constants of each layer of the laser structure are the same as those used in our previous work on thin p-clad InGaAs SQW lasers [Wu94b]. Figure 3.1 shows the calculated Δn of thin (250 nm) p-clad diode lasers as a function of ridge height when various oxide values are used as the current blocking layer. It is interesting to note that relatively large values of Δn are obtained with the removal of small amounts of material. For example, a Δn value of greater than 3×10^{-3} is

obtained when 130 nm of epitaxial material is removed and replaced by 130 nm of native oxide. If a conventional thick p-clad layer is used instead of a thin p-clad layer (1300 nm vs 250 nm), a Δn value of only $\sim 1 \times 10^{-6}$ is obtained for the same removal/replacement process. In order to achieve a Δn of 3×10^{-3} in the 1300 nm thick material, an order of magnitude more material (~ 1200 nm) must be removed from the laser structure creating a "high-ridge" device. From a Δn point of view therefore, a low-ridge, thin p-clad device is equivalent to a high-ridge, thick p-clad device. If Δn is the key parameter which determines device performance, then low-ridge, thin p-clad lasers should not show the high threshold effect as ridge width is narrowed [Shie89, Beer91]. In addition, they should be capable of operating in a single spatial mode to high cw power levels if the ridge width is sufficiently narrow [Fisc87, Bour90, Take90]. These two speculations are addressed in Sections 3.4 and 3.5 respectively.

3.3 Device Fabrications

Thin p-clad lasers with 130 nm ridge height and four different ridge widths ($w=5 \mu\text{m}$, $10 \mu\text{m}$, $25 \mu\text{m}$ and $50 \mu\text{m}$) are fabricated using a pulsed anodic oxidation technique [Grov94]. In this technique, photoresist is used to define the ridge widths on the laser wafer which is then used as one

of the electrodes in an electrolyte composed of 40 parts ethylene glycol, 20 parts water (H_2O) and one part phosphoric acid (H_3PO_4). Running 700 μ sec wide current pulses through the electrolyte at 50 Hz repetition rate converted 130 nm of epitaxial material into 100 nm of native oxide in about 3.5 minutes (anodic oxidation current density ~ 100 mA/cm²). The laser material is then thinned to about 100 μ m and a Ge/Au/Ni/Au contact metallurgy deposited onto the n-side by electron beam evaporation. After a standard high temperature anneal, a Au/Ni/Au contact metallurgy is electron beam evaporated onto the p-side and 450 μ m wide bars cleaved from the material. The cleaved bars are then scribed into 500 μ m wide chips and soldered, substrate-side-down, onto indium-coated copper blocks. It is important to note that the p-side contact was not annealed. If it were annealed, the p-contact would not be "shiny" and laser thresholds would be very high as shown in chapter 2.

3.4 Pulsed Current Characteristics

As discussed in Section 3.2, low ridges in thin p-clad material produce relatively big Δn values ($\Delta n \sim 3 \times 10^{-3}$ when using 250 nm-thick p-clad material with 130 nm ridges). To see if this Δn is sufficient to avoid the high threshold effect at narrow ridge widths reported in references 1 and 2, the pulsed threshold current (I_{th}) and laser emission energy of the 130 nm-ridge, thin p-clad lasers are measured and

compared with the data reported for thick p-clad devices [Shie89, Beer91]. In Figure 3.2, the thick p-clad lasers are (a), 200 nm-ridge lasers [Shie89] with 400 μm cavity length and (b), oxide-defined stripe devices [Beer91b] with 510 μm cavity length. As can be seen, I_{th} for both laser types increases as the stripe width is narrowed, the increase being very large for the oxide-defined stripe lasers. Moreover, there is a lasing energy jump [Wu94] associated with the increase of threshold current for both thick p-clad laser types. In contrast, as the stripe width of the 130 nm-ridge, thin p-clad laser is decreased from 50 μm to 5 μm , I_{th} decreases from 50 mA to 10 mA and the lasing energy is essentially constant. It appears that the lateral index step $\Delta n \sim 3 \times 10^{-3}$ is sufficiently big in the thin p-clad, 130 nm ridgeguides to create a low loss lateral waveguide. If Δn is too small, the lateral dimension of the lasing mode spreads out into the unpumped region causing a large mode loss. This forces the required carrier density for lasing to be very large leading to carrier-induced antiguidance and additional mode loss [Shie89, Beer91b].

Since a low loss lateral waveguide appears to exist in the thin p-clad, 130 nm ridgeguide lasers, their lateral far-fields should also be quite different from those observed in references [Shie89, Beer91b]. To check this point, we have to measure the lateral far-field distributions of thin p-clad diode lasers by using the setup shown in Figure 3.3. In the measurements, diode lasers are kept at room temperature and

by rotating the detector to obtain the far-field distributions. As shown in Figure 3.4, a single-lobe lateral far-field pattern is obtained for lasers with 5 μm , 10 μm and 25 μm ridge widths at $I \sim 1.1 I_{th}$. The single-lobe far-field pattern of the 5 μm ridge-width diode laser is about 5 times narrower than the single-lobe pattern reported in [Shie89] and totally different from the double-lobe pattern reported in [Beer91b]. As the drive current increases to $\sim 1.5 I_{th}$, both 5 μm and 10 μm lasers remain single-lobed with no significant change in pattern width. The lateral far field pattern for the 25 μm laser however, changes from single-lobed to double-lobed as the current increases to $1.5 I_{th}$. Since similar behavior is observed in the far field during cw operation of the 25 μm device, the change can probably be attributed to spatial-hole burning [Garr87] rather than thermal waveguiding [Bour90]. At $I = 1.5 I_{th}$, the 50 μm stripe-width laser still remains double-lobed.

3.5 CW Current Characteristics

As discussed in Section 3.4, a Δn value of $\sim 3 \times 10^{-3}$ is sufficient to avoid the high threshold effect at narrow ridge widths. It is interesting to ask if this Δn is also sufficient to allow single lateral mode operation to high cw power levels when the ridge width is 5 μm . To check this

point, the cw lateral far-field patterns of several 5 μm wide, 130 nm-ridge, thin p-clad diode lasers are measured at four drive currents: 40 mA, 80 mA, 120 mA and 160 mA (see Figure 3.5). Typically one observes that the full width at half maximum (FWHM) of the patterns ($\sim 10^\circ$) increases by less than 1° as the current is increased from 40 mA to 120 mA. Between 120 mA and 160 mA, the FWHM increases by about 3° . In order to understand the cause of this broadening, the lateral far field patterns are also measured using short pulse excitation. In this case, no broadening is observed over the entire current range leading us to believe that the slight cw broadening observed up to 120 mA is due to a narrowing of the near field caused by thermal index guiding [Bour90]. While the relatively large increase of the broadening above 120 mA could be due to the onset of higher mode oscillation, the lack of any significant beam steering tends to rule against this possibility [Guth94]. In any event, the addition of a heat spreading layer should be very effective in reducing this broadening effect since the p-cladding layer is very thin. The measured FWHM value of the transverse far-field pattern is $\sim 42^\circ$, independent of current

The measured cw output power versus drive current (P-I) characteristic is plotted in the inset of Figure 3.5. As shown, the slope efficiency stays constant up to about 120 mA (~ 70 mW of cw total output power) and then begins to drop at higher currents due to heating. Threshold current and total differential quantum efficiency are 10 mA and 49 %, respectively.

respectively. The threshold current of 10 mA is comparable to that reported for conventional SQW InGaAs high-ridge lasers [Fisc87, Bour90, Take90] although the differential quantum efficiency is $\sim 10\%$ smaller. In order to see if this result could be improved on, thin p-clad diode lasers are fabricated with a 180 nm-ridge height and, according to Figure 3.1, a Δn of close to 5×10^{-3} . In this case a cw total differential quantum efficiency of 61 % (cavity length $L=600\ \mu\text{m}$ and stripe width $w=5\ \mu\text{m}$) and threshold current of 9 mA are measured. Figure 3.6 shows the measured CW P-I characteristics of the 5- μm stripe, 180 nm ridge lasers when different cavity length L are considered. As can be seen from this plot, the 180 nm ridge lasers show comparable P-I performance with those reported for the conventional ridge-guided lasers and indicate strong waveguiding in these thin p-clad, narrow stripe lasers.

3.6 Ridge Height Dependent Diode Laser Performance

It is mentioned in Section 3.2, that high ridge structure has to be performed for thick p-clad narrow stripe ridge-guided diode lasers to obtain sufficient index step in operating at low threshold, single spatial mode regime. In addition, CW measurements of thin p-clad ridge-guided lasers have indicated that diode laser performance greatly depends on the ridge height of the device. Since we are interested in

understanding the dependence of narrow stripe laser behaviors on the ridge height, thin p-clad (250 nm) lasers as well as thick p-clad (1300 nm) lasers with 5 μm stripe width and various ridge heights are fabricated and characterized. Both types of samples are prepared by using similar process steps as described in Section 3.3. Thick p-clad samples are anodic oxidized to get right heights: ~ 230 nm, 530 ± 30 nm, 1000 ± 50 nm, 1150 ± 50 nm, 1220 ± 30 nm and 1350 ± 50 nm respectively. On the other hand, thin p-clad samples are oxidized to have ridge heights: 130 ± 5 nm, 180 ± 5 nm and 260 ± 5 nm.

Figure 3.7 shows the measured variations of pulsed P-I characteristics of thick p-clad (1300 nm) 5- μm stripe diode lasers at different ridge height. Figure 3.8 shows the variations of threshold current and slope efficiency as a function of ridge height. It is noticed from Figure 3.7, that P-I behavior of diode laser is not linear until the associated ridge height exceeds 1000 nm for this thick p-clad (1300 nm) laser structure. This is due to the occurrence of higher order modes which generate when the ridge waveguiding is not strong enough to support only single mode operation [Thom80]. The non-linear P-I performance also explains the weak waveguiding inside the low-ridge thick p-clad diode laser and agrees well with the theoretical predictions of Section 3.2. Even for the 1000 ± 50 nm ridge height laser, the non-linear P-I characteristics still occur as the injection current increases up to ~ 100 mA. From Figure 3.8, it is observed that threshold current (I_{th}) of thick p-clad ridge

guided laser decreases as the ridge height increases to ~ 1000 nm and becomes saturated when the ridge height increases further in the measured range. In this study, the minimum I_{th} value obtained for the $5\text{-}\mu\text{m}$ stripe-width, $500\text{ }\mu\text{m}$ long, thick p-clad diode laser is ~ 10 mA. As shown in Figure 3.8, for the samples without significant non-linear P-I performance, the slope efficiency η_s increases and reaches the maximum value at ridge height ~ 1150 nm, whereas η_s shows a decrease as ridge height increases from ~ 1150 nm to ~ 1350 nm.

For the thin p-clad samples, however, non-linear P-I characteristics are not observed in the measured range as shown in Figure 3.9. This is due to the strong waveguiding from the low ridge structure. In addition, from the corresponding I_{th} , η_s vs ridge height plot as shown in Figure 3.10, threshold current shows a small value decrease from $I_{th} \sim 11$ mA to $I_{th} \sim 10$ mA as the ridge height increases from ~ 130 nm to 260 nm. This is dramatically different from those of thick p-clad lasers, where ~ 5 time decrease of I_{th} occurs as the ridge height increases from low ridge (~ 230 nm) to high ridge (~ 1000 nm). Additionally, the η_s value of thin p-clad ridge-guided laser increases as the ridge height increases and reaches a maximum point then decreases as the ridge height becomes higher. The decrease of slope efficiency is due to the contraction of lateral mode caused by the strong index-guiding which could make the mode profile narrower than

the gain profile resulting in a lower slope efficiency [Agra84]. In this thin p-clad laser structure, the 180 nm ridge-height laser shows the best performance of slope efficiency.

In summary, we have demonstrated that the lateral refractive index step generated in low-ridge, thin p-clad diode lasers is sufficient to provide low loss lateral waveguiding. The threshold current of 130 nm-ridge diode lasers decreases from 50 mA to 10 mA when the ridge width is decreased from 50 μm to 5 μm whereas the lasing energy remains essentially constant. In addition, the 5 μm stripe devices were shown to be capable of stable, single lateral mode cw lasing with less than 10 % broadening up to total output power levels of about 70 mW. On the contrary, for the thick p-clad (1300 nm) diode laser, deep etching for obtaining ridge height larger than 1000 nm is required to provide the sufficient waveguiding effects for narrow stripe lasers operating with stable single mode output. By the optimization of diode laser structure, single spatial mode operation with linear P-I profiles to much higher cw powers should be possible. This feature with the combinations of the flexibility of fabricating different diffraction grating types (nickel, gold metal grating or dielectric material grating) in thin p-cladding material (no regrowth required) could lead to the development of higher performance gain-coupled DFB lasers [Luo92].

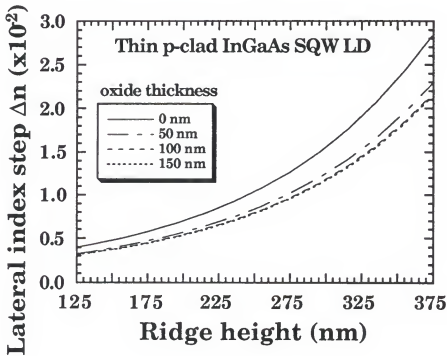
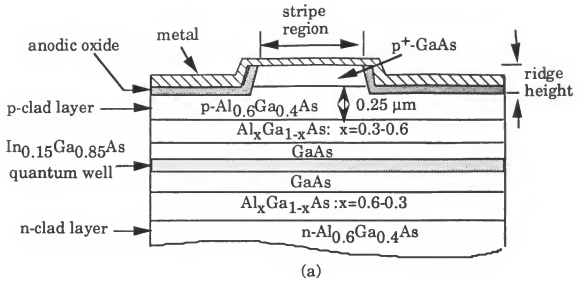


Figure 3.1 (a) Schematic diagram of narrow stripe thin p-clad InGaAs SQW ridge-guided laser. (b) Calculated lateral index step Δn of laser structure in (a) as a function of ridge-height for various current blocking oxide values. It is assumed that the ridge guide structure is covered with Au.

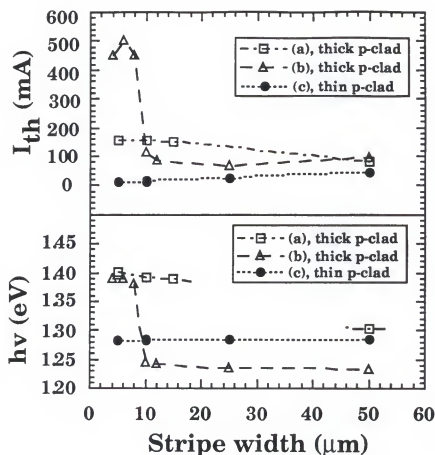


Figure 3.2 The dependence of threshold current and laser emission energy of InGaAs SQW diode lasers on the stripe width for (a) thick p-clad, 200 nm-ridge, $L=400 \mu\text{m}$ [Shie87], (b) thick p-clad, oxide-defined stripe, $L=510 \mu\text{m}$ [Beer91], and (c) thin p-clad, 130 nm-ridge, $L=450 \mu\text{m}$ [this work].

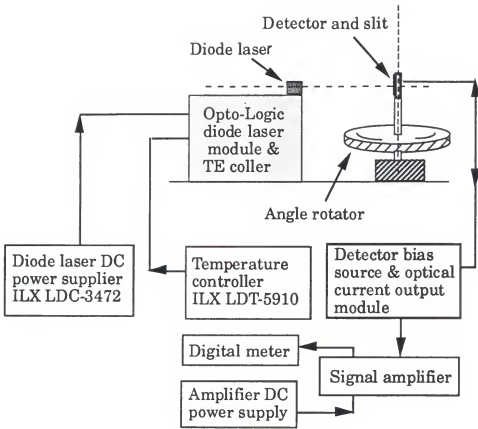


Figure 3.3 Schematic diagram of far-field measurement setup used in this study.

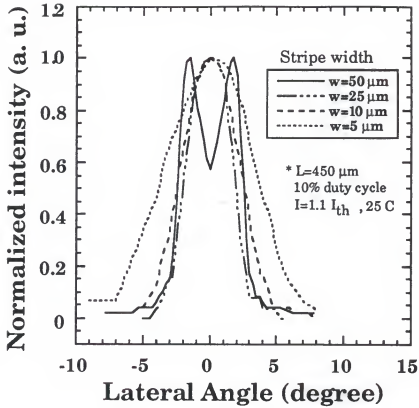


Figure 3.4 The measured lateral far-field intensity distribution of 130 nm-ridge, thin p-clad InGaAs SQW diode lasers as a function of ridge width.

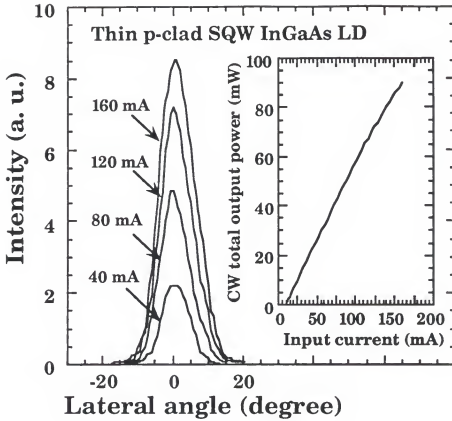


Figure 3.5 CW lateral far-field patterns of a 5 μm wide, 130-nm ridge, thin p-clad InGaAs SQW laser with uncoated facets at a heat sink temperature of 25 $^{\circ}\text{C}$. The corresponding total output power versus drive current characteristic is shown in the inset plot.

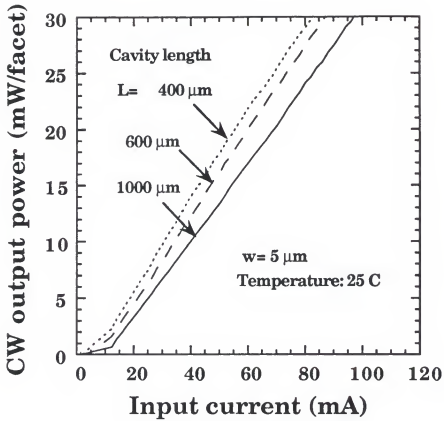


Figure 3.6 The variations of CW P-I characteristics of 5- μm stripe, thin p-clad InGaAs SQW diode lasers with 180 nm ridge height and different cavity length.

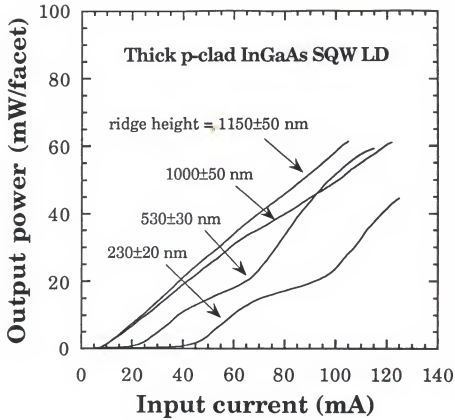


Figure 3.7 The variations of pulsed P-I characteristics of 5- μ m stripe thick p-clad InGaAs SQW diode lasers with different ridge height.

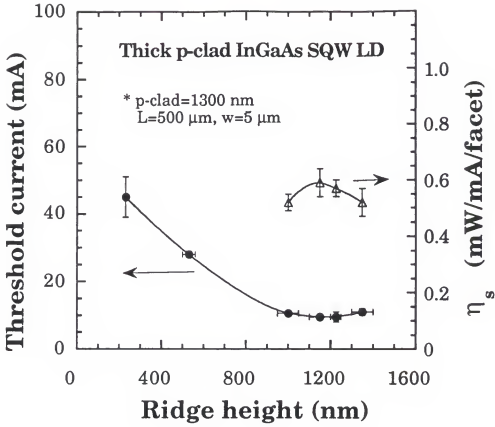


Figure 3.8 The measured dependence of threshold current I_{th} and slope efficiency η_s of 5- μm stripe thick p-clad InGaAs SQW diode lasers on the ridge height.

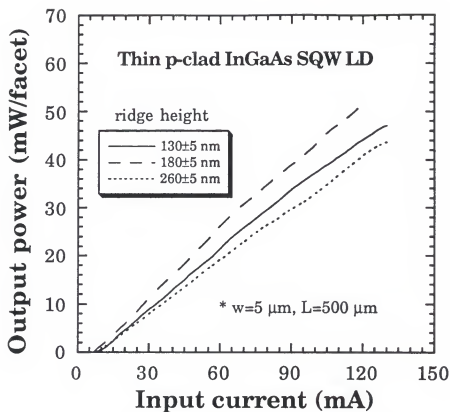


Figure 3.9 The variations of P-I characteristics as a function of ridge height for thin p-clad 5-μm stripe diode lasers.

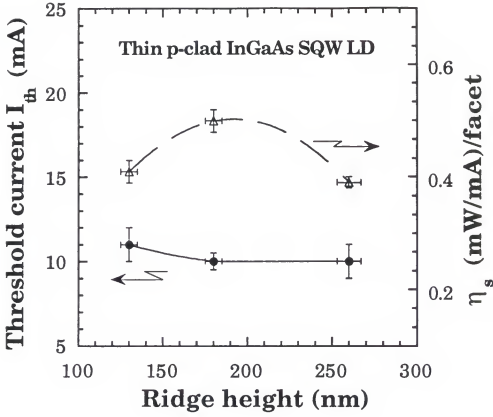


Figure 3.10 The dependence of I_{th} and η_s on the ridge height of 5- μm stripe thin p-clad InGaAs SQW diode lasers.

CHAPTER 4

DUAL WAVELENGTH DIODE LASERS AND THERMAL RESISTANCE IMPROVEMENT

4.1 Introduction

Diode laser emitting simultaneously at multi-wavelength is very attractive for the applications to wavelength division multiplexed communication systems. Several reports have been issued about the fabrication of a monolithic multi-wavelength emission diode laser. The first approach is to use different active layer composition. In this approach, either selectively etching [Saka82] or etch-and-regrowth technique [Boua82] has to be accurately performed in order to obtain reliable diode laser quality. The second approach is to utilize complex grating technique where different lasing wavelengths are obtained by either changing the stripe width to vary the index of refraction [Dutt86] or different periods of DFB grating [Aiki76]. The third approach is to control the modal loss through the change of stripe width of diode laser to obtain lasing on either the first or the second quantized energy levels of a single quantum well active layer [Toku86].

In this method, high temperature and time-consuming material disordering process is used and make this method become hard to control. In addition, more complicated method of using laser-induced desorption to selectively decrease the single quantum well thickness has been developed to fabricate multiple wavelength emission diode lasers [Eple90]. Previously, we have demonstrated that contact reflectivity has a great effect on the thin p-clad SQW diode lasers [Wu94b]. One of the important characteristics is that, by selecting shiny or less shiny contact metal, one can control the modal loss of diode laser and make the laser lase on either the first or the second energy level of a single quantum well active layer. Based on this concept, the process of fabricating the dual wavelength emitting diode lasers should be much simpler and more reliable than the other approaches as stated above. In this chapter, a twin stripe diode laser structure with dual wavelength lasing is proposed and demonstrated.

Recently, the influence of heat spreader on the laser performance has been reported on AlInP red light emission material system and shows significant CW P-I performance improvements [Unge93]. However, the dependence of thermal resistance on the heat spreader thickness and the associated effects on the InGaAs/GaAs material system are seldom reported. In this chapter, a thick Au plating technique is developed and applied to the devices fabricated to show the

reduction of thermal resistance and performance improvements of InGaAs/GaAs diode lasers.

In Section 4.2 the dual wavelength laser structure and fabrication process are described. The experiment results and discussion of the dual wavelength diode lasers are stated in Section 4.3. The main principle of thermal resistance measurements, details of thick Au plating technique as the heat spreader and the performance improvements of thin p-clad InGaAs/GaAs diode lasers with Au heat spreader are presented in Section 4.4.

4.2 Fabrication of Dual Wavelength Diode Lasers

Figure 4.1 shows the twin stripe diode laser structure used in this study. Basically, the diode laser structure is the same as shown in previous chapters except a twin stripe geometry is used instead of a single stripe. The stripe width of Au contact and Ni contact laser is designed as 50 μm and 20 μm respectively in order to have close threshold current for both laser types. The separation distance between these two stripe edge is 50 μm with an isolation slot of 20 μm used to make these two diode laser operate independently.

Wafer is first cleaned in boiling TCA, ACE and methanol. Then, photoresist AZ-1350 is spreaded and baked to define a 20 μm window. Since the isolation slot is important to make the twin stripe diode lasers operate independently, the etching depth of the isolation slot has to be larger than 0.6

μm for this laser structure. The etching depth can be obtained by chemical etching, anodic oxidation or the combination of both methods. In this experiment, the isolation slot is first etched by the chemical solution of 1 part NH_4OH + 1 part H_2O_2 + 50 parts H_2O at room temperature. After the etching step, wafer is cleaned and spreaded with new photoresist to define the two-stripe patterns ($w=20\ \mu\text{m}$ and $w=50\ \mu\text{m}$). Pulsed anodic oxidation is then performed to remove parts of the $\text{p}^+\text{-GaAs}$ cap layer and grow an oxide layer to cover the whole area except the twin stripes. Wafer is then covered with new photoresist and thinned to about $100\ \mu\text{m}$. A metallurgy of $\text{Ge}(20\ \text{nm})/\text{Au}(40\ \text{nm})/\text{Ni}(30\ \text{nm})/\text{Au}(50\ \text{nm})$ is evaporated on the substrate side and annealed at $430\ \text{C}$ for 5 minutes to get n-type ohmic contact. Photoresist of AZ-1375 is spreaded to define p-contact patterns for the lift-off process. At first, by using lift-off technique, $\text{Ni}(60\ \text{nm})/\text{Au}(50\ \text{nm})$ are deposited sequentially to form the Ni-metal contact for the $20\ \mu\text{m}$ stripe lasers. Following this step, photoreisst AZ1375 is used again to define Au contact pattern. A metallurgy of $\text{Au}(80\ \text{nm})/\text{Ni}(50\ \text{nm})/\text{Au}(30\ \text{nm})$ is sequentially evaporated and lift-off to get the Au-metal contact for the $50\ \mu\text{m}$ stripe lasers. Finally, diode lasers are cleaved, soldered on the copper blocks and characterized.

4.3 Dual Wavelength Lasers Experiment Results and Discussion

Figure 4.2 shows the top view and the side view of the twin stripe diode laser after being soldered and bonded on

the copper block. The measured current (I) versus voltage (V) characteristics of the twin stripe diode lasers are shown in Figure 4.3(a) and 4.3(b). As can be seen, both devices show the same cutin voltage $V_c \sim 1.4$ Volts. At $I=50$ mA, the corresponding voltage value of the Ni contact laser is little bit higher than that of Au contact laser (2.1 Volts versus 2.0 Volts), which could be attributed to the fact that Au contact device has larger contact surface than that of Ni contact laser. Figure 4.3(c) shows the I - V characteristic measured between Au contact electrode and Ni contact electrode. Even at high voltage $V=12$ volts, the current-flow between these two electrodes is very small ($< 20 \mu A$) and indicates good electric isolation between these two diode lasers.

The measured pulsed P versus I characteristics of the twin stripe diode lasers are plotted in Figure 4.4. At room temperature the slope efficiency η_s and threshold current I_{th} of the diode laser with cavity length $L=350 \mu m$ are $\eta_s(Au)=0.55$ mW/mA per facet, $I_{th}(Au)=45$ mA and $\eta_s(Ni)=0.18$ mW/mA per facet, $I_{th}(Ni)=105$ mA respectively. At current $I=150$ mA, more than 8 mW/facet output power from the Ni contact laser and more than 50 mW/facet from the Au contact laser can be obtained. The P - I characteristics are comparable to those data reported before [Aiki76, Boua82, Saka82, Dutt86]. The lasing wavelengths of the twin stripe diode laser at injection current $I \sim 1.5 I_{th}$ are shown in Figure 4.5. At $I_i=160$ mA and

$I_2=0$ mA, only the Ni contact laser can lase with the emission wavelength $\lambda_1=914$ nm. While at $I_1=0$ mA and $I_2=65$ mA only the Au contact laser can lase with the lasing wavelength $\lambda_2=967$ nm. When $I_1=160$ mA and $I_2=65$ mA, both laser can lase with $\lambda_1=914$ nm and $\lambda_2=967$ nm, respectively. Therefore a monolithic diode laser with dual wavelength emission capability has been successfully demonstrated by using contact reflectivity effect on the thin p-clad diode laser for the first time. This method of achieving dual wavelength operation is much simpler and more reliable than the other approaches as stated in Section 4.1.

To further check the lasing characteristics of the twin stripe diode laser, near field emission patterns are observed under three different injection current conditions. Figure 4.6(a) shows the near field pattern of the Ni contact laser at $I_1=120$ mA and $I_2=0$ mA. Figure 4.6(b) is the near field pattern of the Au contact laser at $I_1=0$ mA and $I_2=60$ mA. Under these independent operating conditions, no significant spontaneous emission radiated from the unpumped stripe region is observed and indicates a negligible leakage current between these two devices which is consistent with the results shown in Figure 4.3 (c). Figure 4.6(c) shows the near field pattern as $I_1=120$ mA and $I_2=60$ mA. No significant light intensity increase is found in each individual diode laser as compared to the results of Figure 4.6(a) and Figure 4.6(b).

This also demonstrates that these two devices can be operated independently.

4.4 Thermal Resistance Improvements

Low thermal resistance are essential for diode lasers to increase the CW operation temperature and maximize CW output power [Jones75]. Thick Au heat spreader is found to play an important role for improving thermal resistance of diode laser when soldered with epi-side up configuration [Joyce75]. To have thick Au deposited on the top of p-contact of diode lasers, Au plating is the quick and economic method. Two important points are found to be crucial for obtaining thick Au when using Au plating technique: (1) the thickness of photoresist (PR) for the patterns defined and (2) the conditions used for Au plating. In this study, $\sim 5 \mu\text{m}$ thick photoresist is obtained by spreading PR AZ1375 three times at 4000 RPM for 30 seconds each time. In addition, an optimal pulsed Au plating condition (pulse width 700 $\mu\text{sec.}$) is obtained to have thick Au heat spreader. The evolution of the optimal Au plating condition as a function of time is shown in Figure 4.7. It is found that the initial condition is important for obtaining good quality thick Au film, where Au plating current density and repetition rate must be adjusted appropriately to avoid too high values used. Moreover, Au thickness obtained does not only depends on the plating time but also depends on the plating conditions and Au density

inside the plating solution. Normally, the plating conditions shown in Figure 4.7 will give one 4~5 μm Au thickness. By following the Au plating process as shown in Figure 4.7, diode lasers are Au plated, cleaved, soldered and characterized.

Figure 4.8 (a) is the schematic diagram of the Au heat spreader designed for the experiments where the separation between each individual Au heat spreader is important for the diode laser cleaving process. The finished top view of the heat spreader on the p-contact metal is shown in Figure 4.8(b). Figure 4.9 shows the CW P-I characteristics of 5- μm stripe, thin p-clad diode lasers with and without thick Au ($\sim 7 \mu\text{m}$) heat spreader (HS). It is interesting to note that the linear P-I performance of sample without heat spreader is less than 100 mW output power, however the sample with heat spreader shows a linear P-I performance up to 150 mW. In addition, the maximum output power P_{max} significantly improves from P_{max} (without HS) ~ 150 mW to P_{max} (with HS) ~ 220 mW. These $\sim 50\%$ improvements in both linear CW P-I performance and P_{max} value apparently signify the important heat dissipation effects provided by the thick Au heat spreader.

To further understand the influence of heat spreader on the diode laser performance, we have to measure diode laser thermal resistance. Figure 4.10 shows the setup used for the thermal resistance measurements. The main principle for this setup is to utilize the temperature dependence of refractive index n within the laser waveguide. The advantage of this

measurement setup is that no preliminary calibration measurement is required and only a null measurement of the exact wavelength of a single Fabry-Perot mode is made for the R_{th} determination [Paol75]. In this study, diode lasers are driven at a constant current near threshold ($I \sim I_{th}$) with 2 μ sec constant pulse width. The temperature of laser resonator is controlled by varying the input current duty cycle through the change of its repetition rate. The variations of laser temperature can cause lasing wavelength shift. The wavelength shift due to the temperature change from $T+\Delta T$ to T can be expressed as

$$\Delta\lambda_{FP} = \lambda_{FP}(T+\Delta T) - \lambda_{FP}(T) = (d\lambda/dT)\Delta T \quad (4.4.1)$$

where $\Delta\lambda_{FP}$ is the Fabry-Perot mode shift due to the variation of refractive index, $\lambda_{FP}(T+\Delta T)$, $\lambda_{FP}(T)$ are the modes corresponding to the refractive index at temperature $T+\Delta T$ and T respectively.

From the laser oscillation condition, the wavelength λ can be written as

$$\lambda = 2nL/q \quad (4.4.2)$$

where q is an integer and L is laser cavity length. Therefore, $\Delta\lambda_{FP}$ can be expressed as

$$\Delta\lambda_{FP} = \{d(2nL/q)/dT\}\Delta T = (\lambda/n)(dn/dT)\Delta T \quad (4.4.3)$$

From equation (4.4.3), if we assume the refractive index change of $In_xGa_{1-x}As$ ($x \sim 0.15$) quantum well is the same as that

of GaAs as $(dn/dT)=4 \times 10^{-4}$ [Mar 64], then we can get $\Delta\lambda_{FP}/\Delta T \sim 1.1$ Å/K. Since the width of a Fabry-Perot mode near threshold can be less than 0.2 Å/K, the wavelength of a single longitudinal mode is a sensitive indicator of the temperature of the laser resonator [Paol75]. Figure 4.11(a), (b) and (c) show the wavelength shifts of the Fabry-Perot modes of 50 μm stripe width diode laser at different duty cycles and heat sink temperature. The wavelength shift of the selected Fabry-Perot mode is compensated by the drop of heat sink temperature ΔT_{HS} . Since the heat sink temperature change is a linear function of duty cycle [Paol75], one can obtain the temperature change ΔT_{cw} by measuring ΔT_{HS} only to certain value (<100 %) of duty cycle and get the temperature rise ΔT_{cw} from the plot of ΔT_{HS} versus duty cycle. Figure 4.12 is the result of heat sink temperature change as a function of operation duty cycle for the 50 μm stripe lasers with and without thick Au heat spreader. In this plot, ΔT_{cw} is obtained by elongating the linear relationship to 100% duty cycle and get the corresponding intercept ΔT_{HS} value i.e. ΔT_{cw} . After the temperature rise ΔT_{cw} is determined, thermal resistance R_{th} of the laser can be calculated from $\Delta T_{cw} = R_{th} P_{cw}$ [Paol75], where P_{cw} is the average supplied electrical power given by the current I times the diode voltage V . Figure 4.13 is a typical plot of I - V and CW P - I characteristics for the thin p-clad SQW 50 μm stripe diode laser. Since the selected operating current for R_{th} measurement is close to the threshold current, the radiative output power is only a small fraction of the input

power, one can get P_{cw} value directly from Figure 4.13 and calculate R_{th} . From the measurements, the thermal resistance for the sample with heat spreader and without heat spreader as shown in Figure 4.12 are $R_{th}(w/HS)=70$ C/W and $R_{th}(w/o HS)=102$ C/W respectively. Obviously, samples with heat spreader can have less thermal resistance than those without heat spreader.

In order to check the dependence of thermal resistance on the thickness of heat spreader, wide stripe (50 μm) thin p-clad lasers are deposited with various thickness of Au heat spreader and thermal resistance measured as stated above. Figure 4.14 shows the measured variations of thermal resistance of diode laser as a function of Au plating thickness. It is noted that thermal resistance decreases significantly for the first 7~8 μm Au heat spreader thickness and becomes gradually saturated when Au thickness is thicker than 8 μm .

Since diode laser performance is temperature dependent, threshold current I_{th} of diode laser can be normally expressed as $I_{th}(T) \sim \exp(T/T_0)$, where T_0 is the characteristic temperature of diode laser. We are interested in understanding if there is any relationship between diode laser thermal resistance and its temperature related performance. To check this point, diode lasers with different thermal resistance are measured at various temperature (from 20 C to 80 C) in both pulsed and CW operation. Figure 4.15 shows the variations of laser characteristic temperature T_0 as function of thermal

resistance when operated in pulse and CW conditions. For both pulsed and CW operations the characteristic temperatures remain relatively flat when thermal resistance is less than 80 C/W. As thermal resistance becomes larger than 80 C/W, the associated T_0 values start to decrease gradually. Additionally, due to the heat effect from the CW operation, the average characteristic temperature is ~ 15 C lower than that of pulsed operation. The measured dependence of pulsed and CW differential quantum efficiency (dQE) on the heat sink temperature of diode lasers with different thermal resistance $R_{th} = 44$ C/W, 57 C/W and 96 C/W are shown in Figure 4.16. In the pulsed operation, the dQE values show a weak function of heat sink temperature and no significant thermal-resistance dependence is observed. However, in the CW operation, differential quantum efficiency of diode laser shows a great dependence on heat sink temperature as well as the thermal resistance. The dQE value of laser with $R_{th}=96$ C/W decreases significantly as the heat sink temperature is beyond 60 C. This pronounced decrease in differential quantum efficiency could be due to the increase of non-radiative Auger recombination [Dutt83] or carrier leakage over heterobarriers [Good75, Dutt81] for the high R_{th} diode laser when operated at high temperature CW condition.

In summary, thin p-clad diode lasers with a two-stripe configuration emitting dual wavelengths through the control of the contact reflectivity are successfully demonstrated for

the first time. The fabrication process of this dual wavelength diode laser is much simpler and more reliable than those approaches used before. Based on this experiment results, one can design a thin p-clad diode laser with several emission energy levels inside the single quantum well and select the suitable contact metal to control the emission wavelength to obtain a monolithic multiple wavelength emission diode laser. Additionally, thermal resistance was found to play an important role for diode lasers operating at high temperature in CW condition. Laser performance can be greatly improved by reducing its thermal resistance through the deposition of thick Au heat spreader. However, both the characteristic temperature T_0 and differential quantum efficiency dQE show very weak dependence on the thermal resistance when diode laser is in pulsed operation.

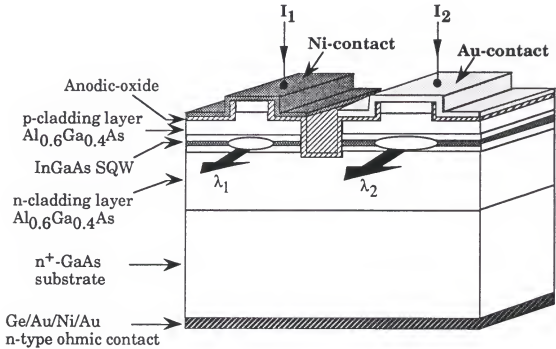
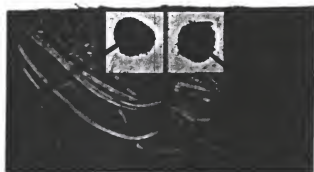


Figure 4.1 Schematic diagram of dual wavelength diode laser structure used in this study. The details of the epilayer thickness and the associated compositions are the same as those shown in Figure 2.1.

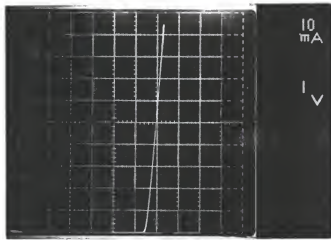


(a)

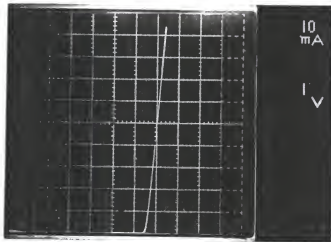


(b)

Figure 4.2 (a) The top view and (b) side view of dual wavelength InGaAs SQW diode laser after soldered and bonded on the copper block

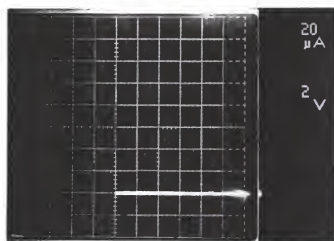


(a)



(b)

Figure 4.3 Measured I-V characteristics of dual wavelength emission InGaAs SQW (a) Au contact and (b) Ni contact diode lasers. The I-V characteristics between both lasers are also shown in (c).



(c)

Figure 4.3 -Continued.

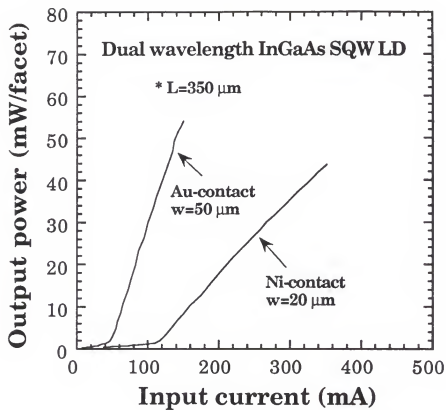


Figure 4.4 Measured pulsed output power versus input current characteristics of dual wavelength InGaAs SQW diode laser.

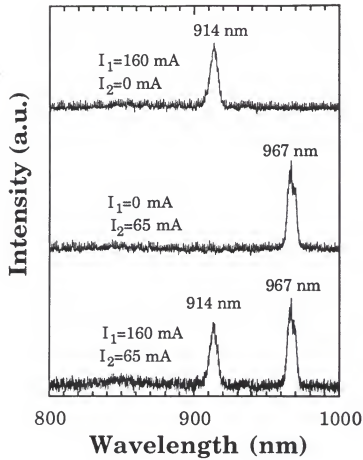
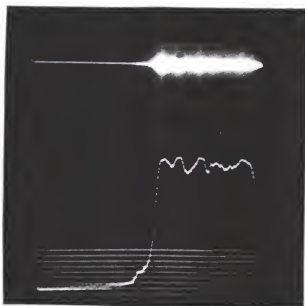


Figure 4.5 The measured lasing wavelength of the dual wavelength InGaAs SQW diode laser when operated at different input current conditions where I_1 and I_2 are the same as those shown in Figure 4.1.

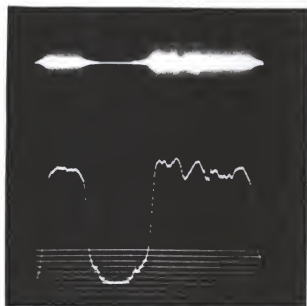


(a)



(b)

Figure 4.6 Measured near-field distributions of dual wavelength emission InGaAs SQW diode laser when operated at (a) $I_1(\text{Ni})=1.1 I_{1\text{th}}$, $I_2(\text{Au})=0$, (b) $I_1(\text{Ni})=0$, $I_2(\text{Au})=1.1 I_{2\text{th}}$, and (c) $I_1(\text{Ni})=1.1 I_{1\text{th}}$, $I_2(\text{Au})=1.1 I_{2\text{th}}$.



(c)

Figure 4.6 -Continued.

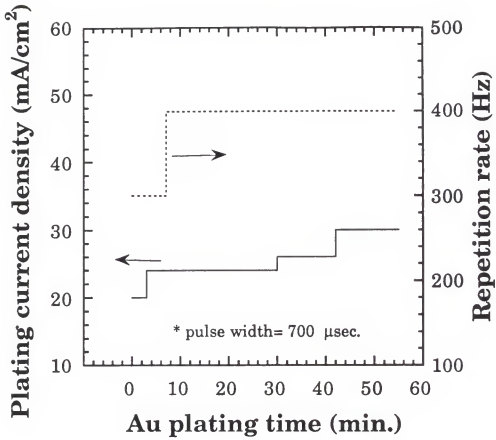
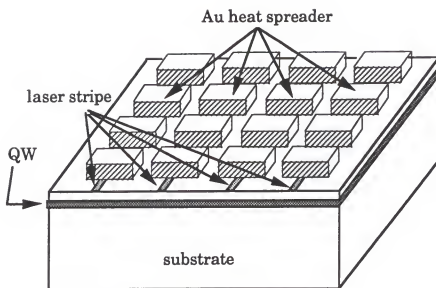
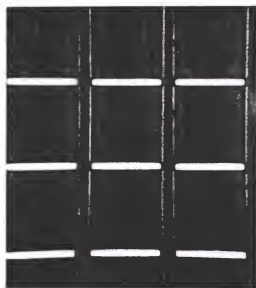


Figure 4.7 The evolution of current density and repetition rate as a function of plating time for Au plating used in the deposition of thick Au heat spreader.



(a)



(b)

Figure 4.8 (a) Schematic diagram of Au heat spreader patterns. (b) The outlook of finished Au heat spreader on the top of thin p-clad InGaAs SQW diode lasers, where Au heat spreader thickness is $\sim 5 \mu\text{m}$.

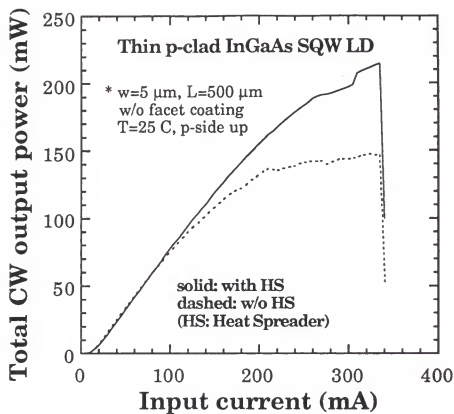


Figure 4.9 Total CW output power versus input current characteristics for 5- μm stripe thin p-clad InGaAs SQW diode lasers with heat spreader and without heat spreader, where heat spreader thickness is $\sim 7\text{ }\mu\text{m}$.

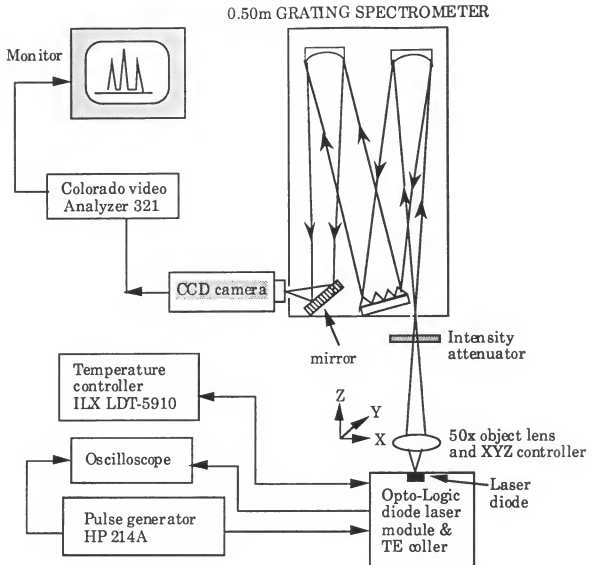
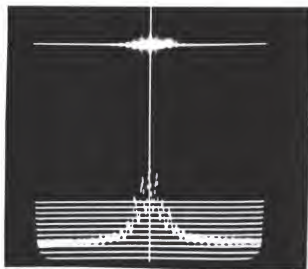
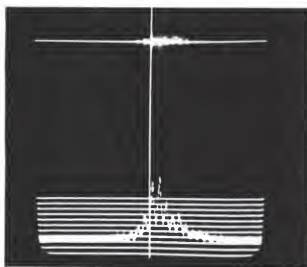


Figure 4.10 Schematic diagram of thermal resistance R_{th} measurement setup used in the experiments.

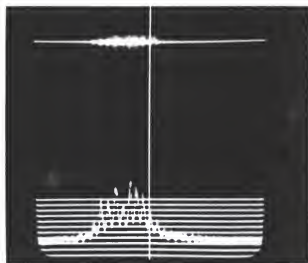


(a)



(b)

Figure 4.11 The variations of the Fabry-Perot mode shifts in 50 μm stripe width, 500 μm cavity length, InGaAs SQW diode laser measured by using the setup shown in Figure 4.10, where laser is operated at $I \sim 1.1 I_{th}$ and, (a) $T_{HS} = 21.8^\circ\text{C}$, 40 % duty cycle, (b) $T_{HS} = 21.8^\circ\text{C}$, 20 % duty cycle and (c) $T_{HS} = 24.8^\circ\text{C}$, 40 % duty cycle. The vertical central line is used as the referenced line for the thermal resistance measurements.



(c)

Figure 4.11 -Continued.

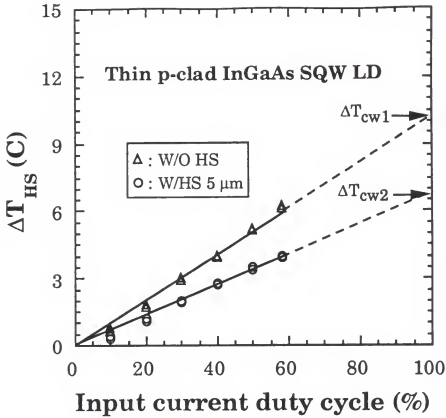


Figure 4.12 The measured heat sink temperature (T_{HS}) rise as a function of duty cycle for the 50 μm stripe width thin p-clad InGaAs SQW diode lasers with and without Au heat spreader. The dashed lines are the extensions of the linear relationship to obtain the ΔT_{cw} value from the intersect points at 100 % duty cycle respectively.

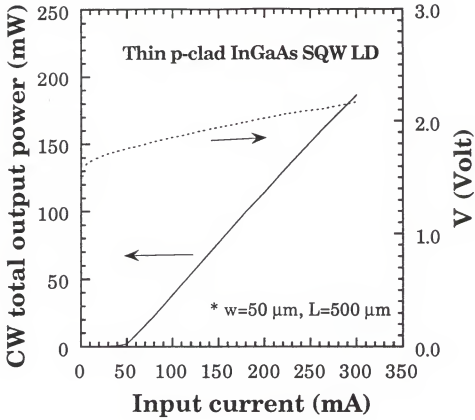


Figure 4.13 Typical CW P-I and I-V characteristics of $50\text{ }\mu\text{m}$ stripe width, Au contact, thin p-clad InGaAs SQW diode laser.

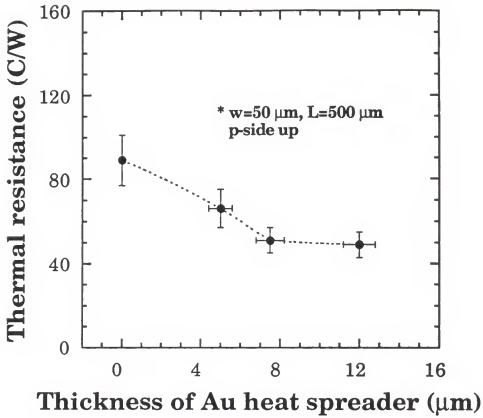


Figure 4.14 The measured dependence of thermal resistance on the Au heat spreader thickness for thin p-clad InGaAs SQW diode lasers.

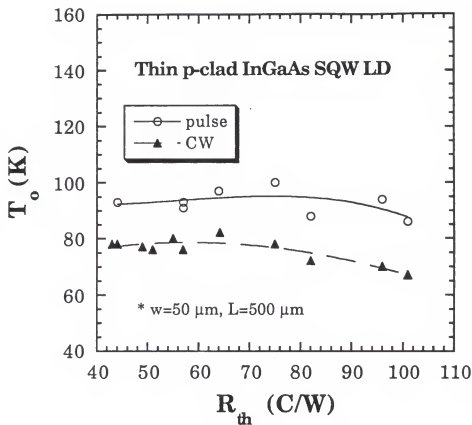


Figure 4.15 The dependence of characteristic temperature T_0 on the thermal resistance R_{th} of diode lasers, where lasers are pulsed operation or CW operation.

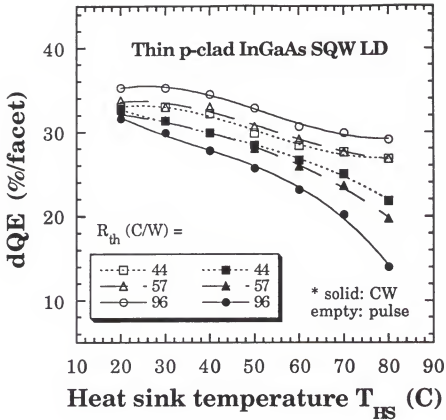


Figure 4.16 The variations of differential quantum efficiency (dQE) as a function of heat sink temperature of thin p-clad InGaAs SQW diode lasers with various R_{th} , where lasers operated in pulse and CW are compared.

CHAPTER 5

p⁺-GaAs CAP LAYER THICKNESS EFFECTS

5.1 Introduction

In previous chapters we have described the influence of contact reflectivity on the thin p-clad diode laser performance and several diode laser fabrication advantages of this interesting structure. However, since the p-cladding layer is only 250 nm thick and, especially, the associated refractive index value at the lasing wavelength for the cap layer is very close to that of quantum well, the p⁺-GaAs cap layer thickness could substantially affect the diode laser behavior [Suem75]. In our continuous work on this thin p-clad (250 nm) laser structure, we have found that both wide stripe and narrow stripe lasers with 200 nm p⁺-GaAs cap layer show a long time delay between the application of an excitation current pulse and the onset of stimulated emission [Wu96a]. In addition, this lasing delay time becomes shorter as the input current increases. Besides the lasing time delay characteristics, threshold current of this thick p-cap (200 nm) laser is abnormally high and show strong dependence on

the period of the excitation current on-time. Moreover, as the cap layer thickness is reduced below 170 nm, diode laser performance improves significantly and no lasing delay is observed for the wide stripe lasers. For the narrow stripe 300 ridge-height lasers, stripe width (w) becomes an important factor in determining diode laser performance. Long time lasing delay behaviors are observed for the 6- μm stripe-width lasers and Q-switching lasing performances are obtained for both 3.5- μm stripe-width and 2.5- μm stripe-width lasers. However, when stripe width is reduced to $w=1.5\ \mu\text{m}$, neither long time lasing delay nor Q-switching performance is found. In Section II, diode laser structure used in this study is presented. Also included are the theoretical calculation results of optical confinement factor Γ and modal loss α_i of thin p-clad laser structure. The gain-guided device fabrication process, experimental results and discussions are described in Section III. In Section IV, the details of fabricating process for narrow stripe, 300 nm ridge-height lasers and performance characterized are presented.

5.2 Laser Structure and Theoretical Calculations

Figure 5.1 shows the thin p-clad InGaAs SQW diode laser structure used in this study, where the quantum well thickness is 80 Å and p⁺-GaAs cap layer thickness t is 200 nm. As mentioned before, the increase of cap layer thickness could substantially affect diode laser performance, in order

to check this point the optical confinement factor and the corresponding modal loss of the laser structure shown in Figure 5.1 are calculated as a function of p⁺-GaAs cap layer thickness t . In the computations, a lasing wavelength of 950 nm and shiny Au metal with refractive index of 0.174 - i 5.691 [Gray72] used as the p-contact are assumed. The calculated results are shown in Figure 5.2. In this plot, it is noticed that Γ and α_i remain relatively flat upto $t \sim 100$ nm and then changes slowly when t is increased from 100 nm to 140 nm. In addition, when t is increased beyond 140 nm, the modal loss α_i increases quickly and the optical confinement Γ decreases significantly. At 200 nm cap layer thickness, modal loss α_i is increased to $\sim 66 \text{ cm}^{-1}$ and optical confinement factor Γ becomes as small as $\sim 0.4 \%$. The calculated results indicate that much more material gain is required for thin p-clad lasers to reach threshold condition if the p-cap layer thickness is changed from $t=100$ nm to $t=200$ nm. This speculation could also be seen from the calculated near field intensity distributions as shown in Figure 5.3, where the peak intensity in the quantum well decreases quickly with the increase of t ($t \geq 150$) and becomes smaller than that in the p-cap layer when t is thicker than 175 nm. As p-cap thickness is continuously increased to $t=200$ nm, most of the near field intensity is "coupled" inside the p-cap layer. Consequently,

a very small value of Γ and a large α_i are obtained as shown in Figure 5.2.

5.3 Long Time Lasing Delay in Gain-Guided Lasers

To check diode laser performance, gain-guided lasers with stripe width $w=50, 25, 10$ and $5 \mu\text{m}$ are fabricated, where non-alloyed Au and alloyed Ge/Au/Ni/Au metallurgy are used as the p-type and n-type contact respectively. Diode lasers with various cavity length are then soldered on the In coated copper blocks and characterized at room temperature.

Figure 5.4 shows the pulsed output power (P) versus input current (I) characteristics of thin p-clad gain-guided diode lasers with $325 \mu\text{m}$ cavity length and different stripes when measured at $2 \mu\text{sec}$ pulse width and 1 KHz repetition rate. As can be seen from this plot, a lot of spontaneous emission occurs for all samples before the stimulated emission starts. In addition, threshold currents are abnormally high and slope efficiencies are much smaller ($< 0.10 \text{ mW/mA}$) than those of lasers fabricated with normal p-cap layer thickness (100 nm). From the plot of inverse slope efficiency η_s^{-1} versus cavity length L , a measured modal loss α_i of $\sim 64 \text{ cm}^{-1}$ is obtained, which is in good agreement with the calculated results.

As stated in Section 5.1, these diode lasers show long time delay between the excitation of current pulse and the

start of stimulated emission. To find out this point, lasers with various stripe widths are measured at a constant repetition rate: 1K Hz and different pulse widths: 2, 4, 6, 8, 10 and 12 μsec . All the samples show similar lasing delay behaviors and the lasing delay time decreases as the input current increases. Figure 5.5(a)-5.5(d) show the variations of the time response (upper trace) of a 50 μm stripe, 500 μm cavity gain-guided thin p-clad InGaAs SQW laser when a current pulse I (lower trace) with 12 μsec pulse width and 1 KHz repetition rate is applied. At $I=900$ mA, the lasing delay time is ~ 10 μsec . and then decreases to ~ 5 μsec . when I is increased to ~ 1100 mA. In addition to the lasing delay, we have found that lasing threshold currents of diode lasers are greatly dependent on the period of input current on-time τ . Figure 5.6(a)-5.6(d) show the measured τ dependent lasing behaviors (upper trace) of a 50 μm stripe width diode laser, where the lasing output power is kept constant at ~ 5 mW/facet. Two interesting results are observed from the measurements: (1) the input current I for having the same output power decreases remarkably from $I \sim 1600$ mA to $I \sim 1000$ mA as τ is increased from 2 μsec to 8 μsec and then remains unchanged as τ is beyond 12 μsec . However, if τ is increased upto very high value, due to heating effect, stimulated emission would not occur. (2) The spontaneous emission intensity decreases as τ is increased. Figure 5.7 (a) and (b)

show the schematic diagram of the lasing delay phenomena and the measured dependence of threshold τ on the input current for diode lasers with 500 μm cavity length and various stripe width: 5, 10, 25 and 50 μm , respectively. For the 50 μm stripe width laser, the averaged current decreases significantly from ~ 1000 mA to ~ 720 mA (~ 28 % reduction) as the threshold input current pulse on-time is increased from 2 μsec to 12 μsec . For the 5 μm stripe width laser, the averaged current decreases from ~ 280 mA to ~ 220 mA (~ 21 % reduction) when the threshold input current on-time τ_{th} increases from 2 μsec to 12 μsec . The possible reason for the difference of threshold current improvements between 50 μm stripe laser and 5 μm stripe laser could be due to the higher current spreading effects from the 5 μm stripe laser than that of the 50 μm stripe laser [Yone73].

The calculated results of Figure 5.2 indicate that thin p-clad laser structure with 200 nm p-cap layer shows small optical confinement factor Γ and large modal loss α_1 . To understand what is the dominant cause for the abnormal lasing delay performance in wide stripe gain-guided quantum well diode laser, both thick p-clad and thin p-clad InGaAs SQW gain-guided diode lasers with thin (100 nm) p^+ -GaAs cap layer thickness are fabricated and characterized. Moreover, wide stripe thin p-clad InGaAs SQW diode laser with less shiny Ni contact are measured and used as the large modal loss referenced sample for comparison. Table 5.1 shows the

measured results of lasing delay behaviors of various stripe width, gain-guided InGaAs SQW lasers, where sample L978 is thick p-clad (1300 nm) laser with 100 nm p-cap layer, sample L979 and sample L529 are thin p-clad (250 nm) lasers with 100 nm p-cap layer and sample L980 is thin p-clad (250 nm) laser with 200 nm (structure as shown in Figure 5.1). It is noticed from this table that lasing delay occurs for the narrow stripe ($<10 \mu\text{m}$) gain-guided SQW lasers of all three sample types and is independent of the optical confinement factor Γ and modal loss α_1 . However, for the wide stripe lasers, only samples fabricated from laser structure (L980) with small optical confinement $\Gamma \sim 0.4$ % have the unusual lasing delay behaviors. The comparison between sample L980 and L529 also clearly indicates that the decrease of optical confinement induced by the increase of p⁺-GaAs cap layer thickness in the thin p-clad of laser structure is the main cause of the abnormal lasing delay observed in the wide stripe single quantum well laser. This statement is also indirectly consistent with the experiment results observed in double heterostructure (DH) lasers [Dyme72], where optical confinement factor Γ is big and no lasing delay obtained.

Injection carriers induced refractive index changes of active region have been shown important in determining the lasing delay behaviors of semiconductor lasers [Grün74, Thom74, Nune77]. In addition, this index change was found as

a function of current pulse time and injection current density [Nune77]. For the InGaAs quantum well, carrier-induced refractive index depression larger than 0.5 has also been reported [Shie89]. To see how the refractive index change of active region Δn_{active} could affect diode laser performance, the variations of optical confinement factor Γ and the associated modal loss α_i are calculated for the laser structure shown in Figure 5.1. Figure 5.8 shows the calculated dependence of optical confinement factor and modal loss on Δn_{active} , where two different p-cap layer thickness $t=100$ nm and $t=200$ nm are considered. For the 200 nm p-cap layer device, both the optical confinement factor and modal loss show strong dependence on Δn_{active} . When Δn_{active} is changed from $\Delta n_{\text{active}} = -0.2$ to $\Delta n_{\text{active}} = +0.2$, the associated optical confinement factor changes from 0.21 % to 0.81 % and modal loss changes from 72 cm^{-1} to 52 cm^{-1} . For the 100 nm p-cap layer device, under the same variations of Δn_{active} the corresponding optical confinement factor changes from ~2 % to 2.7 % and modal loss shows a relatively small change from $\sim 4 \text{ cm}^{-1}$ to 2 cm^{-1} . The combined variations of optical confinement factor and modal loss due to the change of Δn_{active} could lead to a dramatic difference in threshold material gain g_{th} for the two different laser types to reach threshold conditions. Figure 5.9 is the calculated results of threshold quantum well gain g_{th} as a function of refractive index change of active region Δn_{active} for diode lasers with 100 nm, 200 nm p-

cap layer thickness, where a cavity length $L=500 \text{ } \mu\text{m}$ and a facet reflectivity of 0.3 are assumed. It is noticed from Figure 5.9 that g_{th} changes significantly for the laser with 200 nm p-cap layer from $g_{th}(\Delta n_{active}=0)=2.7 \times 10^4 \text{ cm}^{-1}$ to $g_{th}(\Delta n_{active}=-0.2) \sim 4.5 \times 10^4 \text{ cm}^{-1}$ and $g_{th}(\Delta n_{active}=+0.2) \sim 0.94 \times 10^4 \text{ cm}^{-1}$ when Δn_{active} changes from 0 to -0.2 and +0.2, respectively. In contrast, under the same variations of Δn_{active} , only a small amount of g_{th} change from $g_{th}(\Delta n_{active}=-0.2)=1400 \text{ cm}^{-1}$ to $g_{th}(\Delta n_{active}=+0.2)=970 \text{ cm}^{-1}$ is found for the 100 nm p-cap layer laser. The dramatic difference of Δn_{active} -dependent g_{th} variations between the 100 nm p-cap layer laser and 200 nm p-cap layer device are consistent with the experimental results shown in Table 1. This is because the variations of g_{th} caused by Δn_{active} of 100 nm p-cap laser is so small that I_{th} could remain relatively unchanged during the whole current pulse of measurements and no lasing delay is obtained. However, for the 200 nm p-cap laser, the variation of g_{th} induced by Δn_{active} is very big that I_{th} could be changed dramatically at different input current on-time and causes lasing delay behaviors.

To explain the unusual lasing delay behaviors of wide stripe SQW lasers, the model proposed by Nunes et al. [Nune77] for the SH diode lasers is adopted, where the refractive index of the active region is primarily affected by three different factors: (1) the injection carriers, (2) the gain-guiding confinement and (3) the heating of active region. Factor (1) could results in a negative increase of refractive

index of quantum well while factor (2) and (3) could cause a positive refractive index change. The combination of these three factors could result in a great variation of Δn_{active} when input current pulse width τ and the injection current density J are changed. Figure 5.10 shows the schematic diagram of the lasing delay model used to explain the experimental results. In this Figure, at some constant current density J_1 , the refractive index change due to the injection carriers could dominate Δn_{active} at the initial current on-time τ_1 and causes a depression of Δn_{active} , causing lasing mode overlap with quantum well gain to decrease and lasing mode overlap with loss in Au to increase, hence, higher g_{th} is required for lasers to start the stimulated emission. If the quantum well gain is not sufficient to overcome total loss, laser could not reach threshold condition. As τ continues to increase, Δn_{active} could become positive, causing lasing mode overlap with quantum well gain to increase and lasing mode overlap with loss in Au to decrease, and less g_{th} is needed to reach threshold condition. Stimulated emission could begin if the laser quantum well gain is large enough to compensate the total loss and lasing delay occurs. Consequently, the lasing threshold of diode laser strongly depends on the current on-time, in other words, the threshold behaviors of lasers are input current on-time dependent. On the other hand, at certain current on-time τ_2 , Δn_{active} could be dominated by the

injection carriers at some injection current density J_1 and cause a negative value of Δn_{active} , hence higher g_{th} is required to reach threshold condition and no stimulated emission is obtained if the material gain is not equal to the total loss. At higher injection current density J_2 , the heating effects of active region could dominate the index change of quantum well and Δn_{active} could be increased in the positive direction. At this point, less g_{th} is needed for reaching threshold condition and laser could start lasing at some time point before τ_2 if the laser material gain is well above the total loss. As a result, lasing delay would become shorter as the input current density increases.

In Section 5.2 we have shown that optical confinement factor Γ as well as modal loss α_i could be significantly improved by decreasing the p^+ -GaAs cap layer thickness of thin p-clad laser structure and lead to an improvement potential of diode laser performance. To check this point, wide stripe (50 μm) thin p-clad diode lasers with three different p-cap layer thickness: 170 ± 6 nm, 130 ± 5 nm and 70 ± 5 nm are fabricated with non-alloyed shiny Au and alloyed Ge/Au/Ni/Au as the p-contact and the n-contact. The various p-cap layer thickness is performed by etching away part of the 200 nm p^+ -GaAs cap layer shown in Figure 5.1 through the utilization of pulsed anodic oxidation technique [Gro94] and MIF 312 developer to strip off the remaining anodic oxide. Lasers with various cavity length are cleaved, soldered on In

coated copper blocks and characterized. Figure 5.11 shows the variations of pulsed threshold currents as a function of cavity length for samples with different p-cap layer thickness when measured at 2 μ sec current pulse width and 1000 Hz repetition rate. It is interesting to see that threshold currents I_{th} decrease tremendously as p-cap layer thickness is reduced from 200 nm to ~130 nm and then slowly decrease when p-cap layer thickness is reduced further. In addition, the increase rate of I_{th} with cavity length is much smaller for the lasers with thin p-cap layer thickness (≤ 170 nm) than that of devices with 200 nm p-cap layer thickness. The decrease of lasing threshold behavior is well consistent with our predictions as shown in Figure 5.2, where the improvements of optical confinement factor Γ as well as the modal loss α_i could directly result in a great reduction of diode laser threshold performance as described in equation (2.2.11). Another important feature is that no lasing delay is observed for the wide stripe lasers during the measurements. This again indicates a significant improvement of optical confinement from the decrease of p-cap layer thickness. The decrease of modal loss with the reduction of p-cap layer thickness shown in Figure 5.2 could also be checked from the measurements of laser slope efficiency η_s at various laser cavity lengths. Figure 5.12 is the measured modal loss of thin p-clad InGaAs SQW diode lasers as a function p⁺-GaAs cap layer thickness. The dashed line in this

plot is the computation results for comparison. As can be seen from the measured points of this figure, the modal loss decreases rapidly from $\alpha_1 = 64 \text{ cm}^{-1}$ to $\alpha_1 = 34 \text{ cm}^{-1}$ when p-cap thickness is decreased from 200 nm to ~170 nm. At ~130 nm p-cap layer, the measured modal loss is $\sim 8 \text{ cm}^{-1}$ and changes slowly to $\sim 3 \text{ cm}^{-1}$ as p-cap layer thickness is reduced further to ~70 nm. The measured results are in good agreement with the theoretical predictions.

5.4 Long Time Lasing Delay and Q-Switching Lasing Delay in Narrow stripe, 300 nm Ridge-Height Lasers.

It has been reported that lasing delay behaviors of narrow stripe quantum well lasers can be eliminated if there is a built-in guide along the junction plane with an effective refractive index step greater than 10^{-3} [Prin85]. In addition, strong waveguiding effects obtained by using thin p-clad structure to fabricate narrow stripe (5 μm) index-guided lasers with performance comparable to those of conventional thick p-clad lasers have been demonstrated [Wu95]. For similar thin p-clad laser structure with 200 nm p-cap layer thickness studied in this chapter we are interested in understanding whether the strong waveguiding effects of narrow stripe lasers could be obtained to eliminate lasing delay by simply removing parts of the outside stripe material.

In Section 5.2 and 5.3 we have demonstrated that the variations of p-cap layer thickness could substantially

change the waveguiding of thin p-clad laser structure. Consequently, the behaviors of ridge waveguide lasers fabricated from thin p-clad material with 200 nm p-cap layer should be quite different from that of ridge-guide lasers fabricated from thin p-clad material with 100 nm p-cap layer. The difference in effective refractive index (lateral index step) between the ridge region and the outside-ridge region Δn is normally used in designing ridge-guide lasers [Agra84]. Therefore, it is interesting to calculate Δn as a function of ridge height (the amount of epitaxial material removed in defining the ridge) for thin p-clad configuration. In the computations, it is assumed that the p⁺-GaAs cap layer, the p-Al_xGa_{1-x}As graded-layer and part of the p-clad layer of the outside-ridge region are removed and replaced with a native oxide, the whole structure being covered with Au. A lasing wavelength of 950 nm, an oxide refractive index of 1.8 and a Au refractive index of 0.174-i5.691 are also assumed in the computations. Figure 5.13 shows the calculated Δn as a function of ridge height (distance measured from the top of p-cap layer on the stripe region to the top of p-clad layer on the outside stripe region) when various oxide values are used as the current blocking layers. As can be found from this plot that a calculated effective refractive index step Δn as high as 3.3×10^{-2} is obtained when the outside stripe p⁺-GaAs cap layer is totally removed. This Δn value is ~10 times larger than that calculated from thin p-clad laser structure with p-cap layer 100 nm (as shown in Figure 3.1 (a)). As a

result, strong waveguiding effects are expected for the narrow stripe lasers when fabricated from this thin p-clad QW laser structure. Besides the Δn computations, we also calculate the lateral far field intensity distributions of diode lasers with different stripe widths. In the computations, a three layer waveguide structure is assumed and the associated refractive index values are quoted from the calculated effective refractive index of the stripe region and outside stripe region. The calculated results are shown in Figure 5.14, where various stripe width $w=1, 2, 3$ and $5 \mu\text{m}$ are concerned. It is noticed from this plot that single lateral lobe of far field pattern could be obtained when stripe width w is not wider than $2 \mu\text{m}$. At $w=3 \mu\text{m}$, a double lobe pattern is obtained while at $w=5 \mu\text{m}$ a triple lobe occurs.

To fabricate narrow stripe diode lasers, $6 \mu\text{m}$, $3.5 \mu\text{m}$, $2.5 \mu\text{m}$ and $1.5 \mu\text{m}$ stripe width on $500 \mu\text{m}$ centers are defined by using standard photolithography technique. Ridge-guided laser structures are formed by etching away the outside stripe p^+ -GaAs cap layer material through the chemical solution of $1 \text{ NH}_4\text{OH} + 1 \text{ H}_2\text{O}_2 + 50 \text{ H}_2\text{O}$ for $\sim 35''$ and followed by an anodic oxidation $\sim 4'$ to grow oxide on the outside stripe region. The resultant ridge height is $\sim 300 \text{ nm}$ after measured by Dektak. Wafer is then thinned to $\sim 100 \mu\text{m}$ and deposited with alloyed Ge/Au/Ni/Au and nonalloyed Au as n-type and p-type contact respectively. Lasers with various cavity length

are cleaved, soldered on the In coated copper blocks and characterized.

Table 5.2 shows the summarized results of narrow stripe diode lasers with cavity length $L=500\text{ }\mu\text{m}$ and different stripe width when measured at $2\text{ }\mu\text{sec.}$ current pulse width and 1000 Hz repetition rate. It is interesting to find that all measured sample types except the $1.5\text{ }\mu\text{m}$ stripe-width sample show either Q-switching or long time lasing delay performance [Ripp74]. Additionally, threshold currents for the samples with lasing delay behaviors are quite high as compared with the results presented in Chapter 3 and then decreases quickly when stripe width is decreased to $w=1.5\text{ }\mu\text{m}$. The $6\text{ }\mu\text{m}$ stripe-width sample shows high average threshold current $I_{th}\sim 250\text{ mA}$ and long time lasing delay behaviors similar to those observed in the gain-guided lasers. For the samples with either $2.5\text{ }\mu\text{m}$ or $3.5\text{ }\mu\text{m}$ stripe-width, a transition from Q-switching to long time lasing delay performance are observed during the measurements. The average threshold currents for both sample types are $I_{th}(w=2.5\text{ }\mu\text{m})\sim 80\text{ mA}$ and $I_{th}(w=3.5\text{ }\mu\text{m})\sim 180\text{ mA}$ respectively. Figure 5.15 (a)-(d) shows the evolution of lasing behaviors of the $2.5\text{ }\mu\text{m}$ stripe-width sample as a function of input current I , where the measured condition is repetition rate: 1000 Hz , pulse width: $2\text{ }\mu\text{sec.}$ At $I=80\text{ mA}$, it is clear to see that stimulated emission starts at the time pulse position corresponding to the ending edge of the input current pulse i.e. Q-switching lasing behavior. As the input current I is increased to 100 mA , both

Q-switching and long time lasing delay occur at the same time. When I is increased further to 120 mA, Q-switching disappears and long time lasing delay dominates diode laser performance. For the 1.5 μm stripe-width laser, neither Q-switching nor long time lasing delay is observed and threshold current decreases dramatically as compared with the samples with wider stripe width ($I_{th}(w=1.5 \mu\text{m}) \sim 25 \text{ mA}$ vs $I_{th}(w \geq 2.5 \mu\text{m}) \geq 80 \text{ mA}$).

Possible explanation for the totally different lasing behaviors between the various stripe-width samples could be due to the different waveguiding effects caused by the effective refractive index step Δn . From the calculated results shown in Figure 5.13, at 300 nm ridge height the associated lateral effective refractive index step is $\Delta n \sim 3.5 \times 10^{-2}$. For the 6 μm stripe-width sample the $\Delta n \sim 3.5 \times 10^{-2}$ could be insufficient to provide strong waveguiding effects to compensate the weak transverse waveguiding effects for laser to operate at low threshold condition. For both 3.5 μm stripe-width sample and $w=2.5 \mu\text{m}$ stripe-width sample, although the lateral waveguiding formed by the refractive index step Δn is still weak to obtain index guiding, the lateral optical confinement could be somehow improved such that Q-switching performance is observed. Since it has been theoretically studied that total loss of diode laser could decrease faster than the gain and confinement so that stimulated emission can occur at the end of current pulse even though laser can not lase during the current pulse

[Nune77]. We believe the large index step $\Delta n = 3.5 \times 10^{-2}$ in our devices (lasers with stripe with $w = 2.5 \mu\text{m}$ and $w = 3.5 \mu\text{m}$) could somehow improve the optical confinement of laser waveguide structure and make stimulated emission occur at the ending edge of current pulse. The significant decrease of threshold current of the $1.5 \mu\text{m}$ stripe-width laser lead us to believe that the effective lateral refractive index step $\Delta n = 3.5 \times 10^{-2}$ could be sufficient to provide strong waveguiding effects to overcome the drawback of small transverse optical confinement as shown in Section 5.2. Since it is believed that waveguiding effects in narrow stripe, ridge-guided lasers are two dimensional properties (transverse and parallel to the quantum well plane) and the waveguiding effect in each dimension is related to that of the other. In order to check this point, we have used the far-field measurement setup (shown in Figure 3.3) to measure the far-field intensity distributions of all four sample types. Figure 5.16 shows the measured far-field intensity distributions of diode lasers when measured at $I \sim 1.3 I_{th}$ with 10 μsec . current pulse, 10 KHz repetition rate and room temperature. As can be seen from this plot that a four-lobe pattern is obtained for the $6 \mu\text{m}$ stripe-width sample. For the $3.5 \mu\text{m}$ stripe-width sample, a triple lobe pattern with an unsymmetric side lobes is observed. For the $2.5 \mu\text{m}$ stripe-width sample, a symmetric double lobe pattern with a large separation is obtained. When the input current or the current pulse width is increased, each lobe is widen and the separation becomes smaller. For

the 1.5 μm stripe-width laser, a single lobe pattern is found during the measurement and remains single lobe pattern when current pulse width is increased. The far-field intensity distribution measurements indicate that $\Delta n = 3.5 \times 10^{-2}$ is sufficient to provide strong lateral waveguiding effects for the 1.5 μm stripe-width sample to overcome the weak transverse waveguiding and operate with a single spatial mode output. Figure 5.17 shows the measured room temperature CW P-I characteristics of the 1.5 μm stripe-width laser. The threshold current and differential quantum efficiency are $I_{th} \sim 29 \text{ mA}$ and $\eta_d = 50 \%$ respectively. The CW transverse (perpendicular to the QW plane) and lateral far-field intensity distributions when measured at 25 C and $I = 1.3 I_{th}$ are shown in Figure 5.18 (a) and (b). It is noticed that both transverse and lateral far field pattern show single lobe behavior despite the transverse waveguiding is very weak. In addition, the FWHM values of both lateral and transverse far field are larger than those obtained before.

In summary, we have shown that p-cap layer thickness is important in determining thin p-clad SQW diode laser performance. At 200 nm p-cap layer thickness, lasing delay occur in both wide stripe and narrow stripe gain-guided lasers. As p-cap layer thickness is decreased, diode laser performance could be dramatically improved and no lasing delay are observed in the wide stripe diode lasers. The lasing delay behaviors can be explained by the refractive

index change of quantum well induced by the current pulse time related injected carriers. In addition, at 1.5 μm stripe width, strong lateral waveguiding effects are sufficient to overcome the deficit of transverse waveguiding and make laser operate in low threshold regime.

p^+ -GaAs cap layer: t nm
$p\text{-Al}_z\text{Ga}_{1-z}\text{As}$: 25 nm ($z=0.6\text{-}0.05$)
p-clad layer $\text{Al}_{0.6}\text{Ga}_{0.4}\text{As}$: 250 nm
$p\text{-Al}_x\text{Ga}_{1-x}\text{As}$: 200 nm ($x=0.3\text{-}0.6$)
GaAs: 7 nm
$\text{In}_y\text{Ga}_{1-y}\text{As}$, SQW ($y\sim 0.15$; 8 nm)
GaAs: 7 nm
$n\text{-Al}_x\text{Ga}_{1-x}\text{As}$: 200 nm ($x=0.6\text{-}0.3$)
n-clad layer $\text{Al}_{0.6}\text{Ga}_{0.4}\text{As}$: 1400 nm

Figure 5.1 Thin p-clad InGaAs SQW diode laser structure with 80 Å quantum well and thick p^+ -GaAs cap layer $t=200$ nm used in the p^+ -GaAs cap layer thickness effect study.

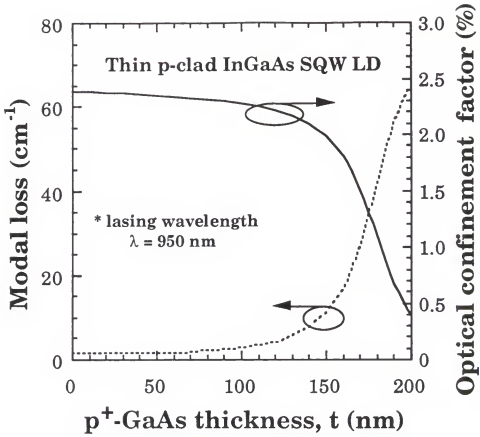


Figure 5.2 The calculated dependence of modal loss α_i and optical confinement factor Γ on the p⁺-GaAs cap layer thickness t of the laser structure shown in Figure 5.1.

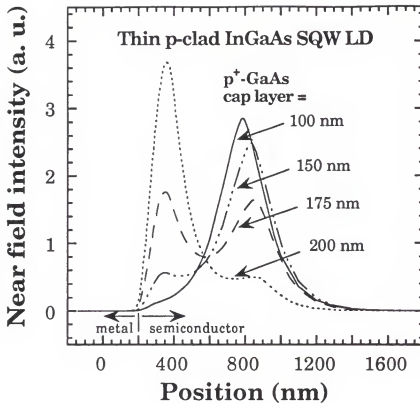


Figure 5.3 Calculated near field intensity distributions of thin p-clad InGaAs single quantum well laser structure shown in Figure 5.1 with different p^+ -GaAs cap layer thickness: 100 nm, 150 nm, 175 nm and 200 nm, where non-alloyed Au is assumed as the p-contact.

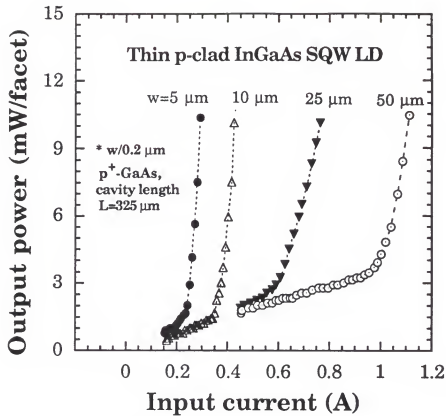
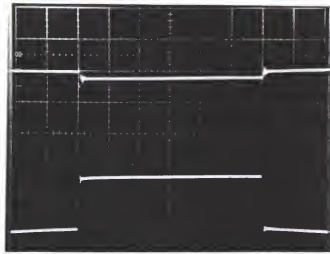
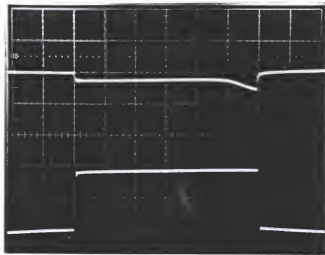


Figure 5.4 Measured pulsed output power P versus input current I characteristics of various stripe width, gain-guided thin p-clad InGaAs SQW diode lasers, where non-alloyed Au and alloyed Ge/Au/Ni/Au are used as the p-contact and n-contact respectively.

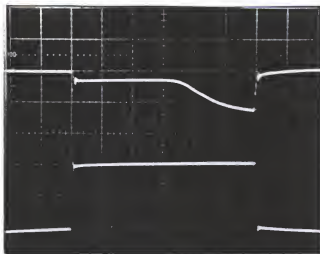


(a)

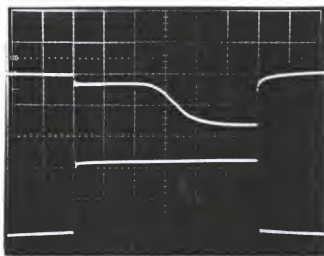


(b)

Figure 5.5 Measured lasing delay characteristics of wide stripe (50 μm) thin p-clad InGaAs SQW diode laser at various input currents: (a) 800 mA, (b) 900 mA, (c) 1000 mA and (d) 1100 mA, where the horizontal scale is $H=2 \mu\text{sec/div.}$, vertical scales are $V_u=100 \text{ mV/div.}$ (upper trace), and $V_i=500 \text{ mA/div.}$ (lower trace).

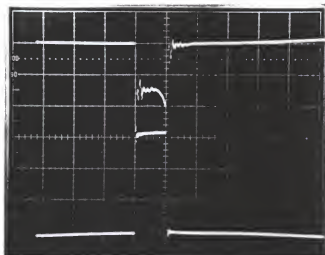


(c)

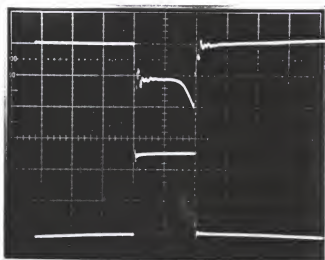


(d)

Figure 5.5 -Continued.

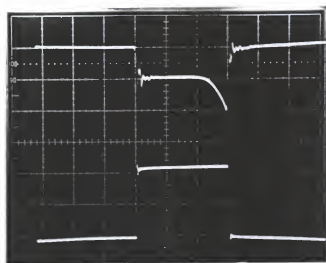


(a)

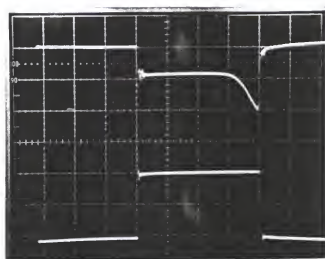


(b)

Figure 5.6 Measured input current pulse width dependent lasing threshold characteristics of wide stripe (50 μm) thin p-clad InGaAs SQW diode laser at pulse widths: (a) 2 μsec , (b) 4 μsec , (c) 6 μsec and (d) 8 μsec where the horizontal scale is $H = 2 \mu\text{sec/div.}$, vertical scales are $V_u = 50 \text{ mV/div.}$ (upper trace), and $V_l = 500 \text{ mA/div.}$ (lower trace)



(c)



(d)

Figure 5.6 -Continued.

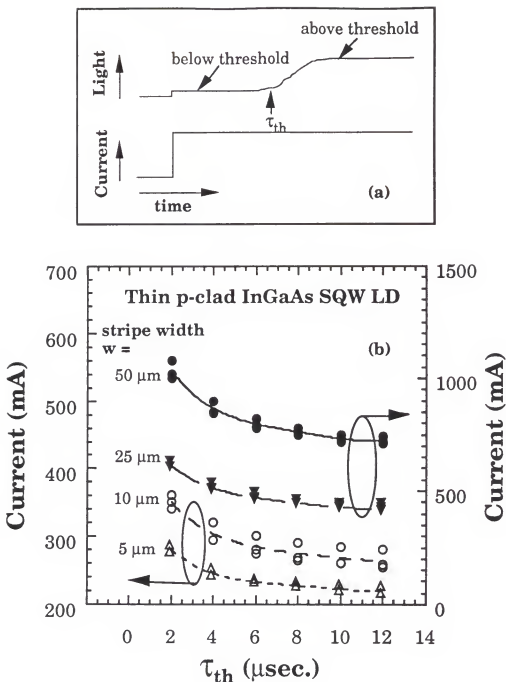


Figure 5.7 (a) Schematic diagram of lasing delay phenomena. (b) Measured dependence of current on the threshold input current on-time of different stripe width, gain-guided, thin p-clad InGaAs SQW diode lasers with 200 nm p⁺-GaAs cap layer, where the repetition rate is 1000 Hz.

<div style="text-align: center;"> <div>Lasing time delay</div> <div>Sample No., Modal loss and Optical confinement factor</div> </div>	Gain-guided laser stripe width			
	50 μm	25 μm	10 μm	5 μm
L978 (thick p-clad) Au contact: $\alpha_i=1\text{ cm}^{-1}$ $\Gamma = 2.3\%$	NO	NO	NO	YES
L979 (thin p-clad) Au contact: $\alpha_i=3\text{ cm}^{-1}$ $\Gamma = 2.3\%$	NO	NO	NO	YES
L980 (thin p-clad) Au contact: $\alpha_i=66\text{ cm}^{-1}$ $\Gamma = 0.4\%$	YES	YES	YES	YES
L529 (thin p-clad) Ni contact: $\alpha_i=70\text{ cm}^{-1}$ $\Gamma = 2.3\%$	NO			

Table 5.1 Comparison of measured lasing delay for various gain-guided SQW lasers with stripe width: 50, 25, 10 and 5 μm , where sample L978 is with 1300 nm p-cladding layer and 100 nm p-cap layer; sample L979 and sample L529 are with 250 nm p-cladding layer and 100 nm p-cap layer; sample L980 is with 250 nm p-cladding layer and 200 nm p-cap layer.

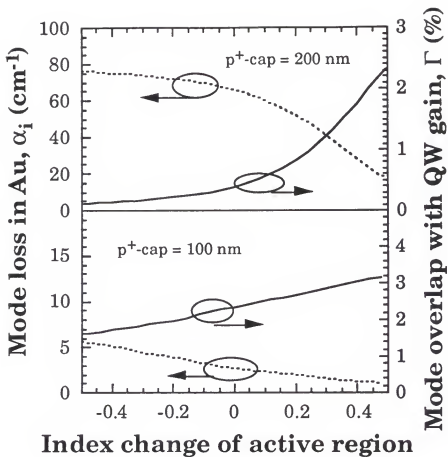


Figure 5.8 Calculated variations of optical confinement factor Γ and modal loss α_i of thin p-clad InGaAs SQW laser as a function of refractive index change of active region Δn_{active} , where p^+ -GaAs cap layer thickness = 100 nm and 200 nm are considered, respectively.

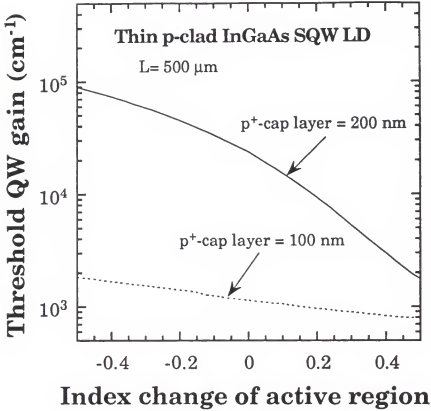


Figure 5.9 The calculated dependence of threshold quantum well gain g_{th} on the refractive index change of active region Δn_{active} for thin p-clad InGaAs SQW laser with different p⁺-GaAs cap layer thickness: 100 nm and 200 nm, where a facet reflectivity of 0.3 and cavity length $L=500 \mu\text{m}$ are used in the computations.

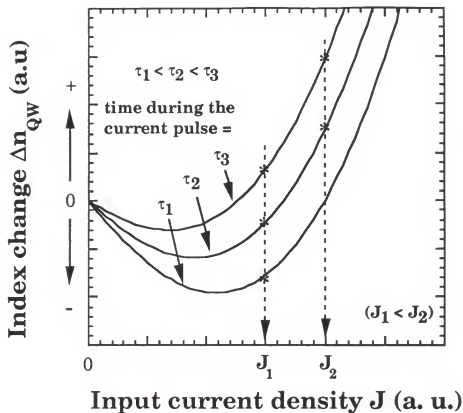


Figure 5.10 Schematic diagram of the dependence of refractive index change of quantum well on the input current density and current pulse time during the current pulse used to explain the unusual lasing delay behavior of thin p-clad InGaAs SQW lasers with thick p-cap (200 nm) layer.

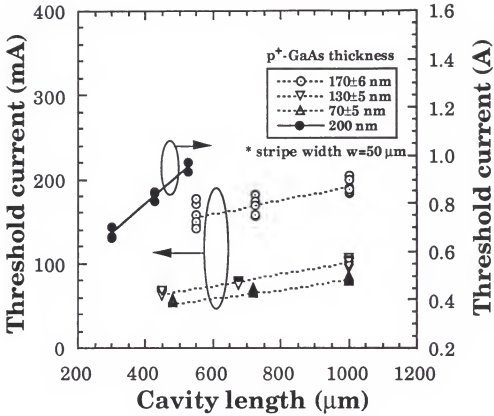


Figure 5.11 The variations of threshold current as a function of cavity length for thin p-clad InGaAs SQW diode lasers with 50 μm stripe width and different p⁺-GaAs cap layer thickness when measured at 1K Hz repetition rate and 2 μsec pulse width.

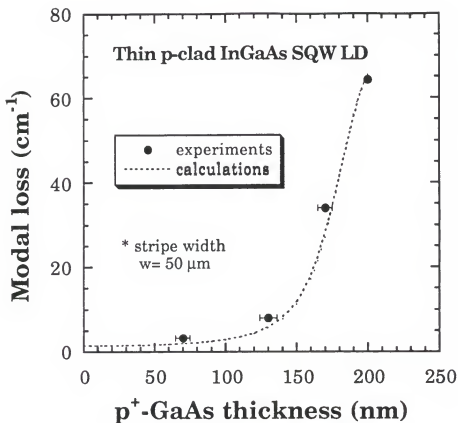


Figure 5.12 The variations of the measured modal loss of thin p-clad InGaAs SQW diode lasers as a function of the p⁺-GaAs cap layer thickness, where the calculated results as shown in Figure 5.2 are also plotted for comparison.

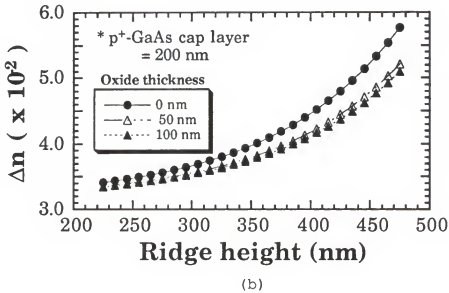
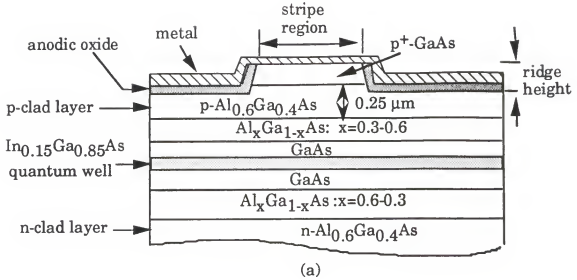


Figure 5.13 (a) Schematic diagram of narrow stripe thin p-clad InGaAs SQW ridge-guided laser, where p^+ -GaAs cap layer is 200 nm. (b) Calculated lateral index step Δn of laser structure in (a) as a function of ridge-height for various current blocking oxide values. It is assumed that the ridge guide structure is covered with Au.

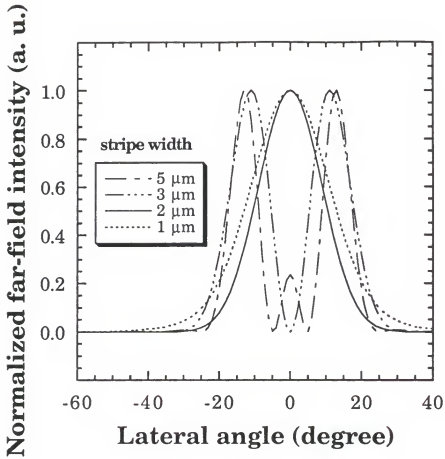


Figure 5.14 Normalized lateral far-field intensity distribution calculated from the laser structure shown in Figure 5.13 (a) when different stripe widths $w=1\ \mu\text{m}$, $2\ \mu\text{m}$, $3\ \mu\text{m}$ and $5\ \mu\text{m}$ are concerned. It is assumed the ridge height is $300\ \text{nm}$ and current blocking oxide on the outside stripe region is $100\ \text{nm}$.

Narrow stripe thin p-clad InGaAs SQW diode lasers with 300 nm ridge height				
Laser performance	stripe width: w			
	1.5 μm	2.5 μm	3.5 μm	6 μm
average threshold current: I_{th}	25 mA	80 mA	170 mA	280 mA
Lasing delay behavior	NO lasing delay	Q-switching to long time delay	Q-switching to long time delay	long time delay

Table 5.2 Summary of narrow stripe, thin p-clad SQW laser performance when measured at 2 $\mu\text{sec.}$ current pulse width and 1 KHz repetition rate, where the diode laser cavity length is 500 μm .

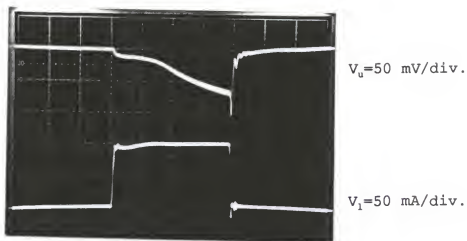


(a)

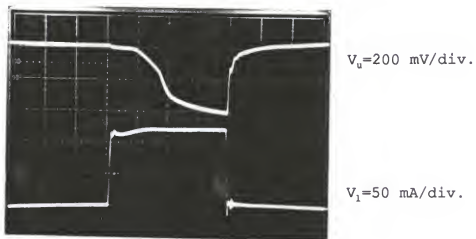


(b)

Figure 5.15 The evolution of lasing behavior from Q-switching to long time lasing delay of a $2.5 \mu\text{m}$ stripe-width thin p-clad InGaAs SQW laser with 300 nm ridge height when measured at $2 \mu\text{sec.}$ current pulse width, 1000 Hz repetition rate and input current (a) $I=60 \text{ mA}$, (b) $I=80 \text{ mA}$, (c) $I=100 \text{ mA}$, (d) $I=120 \text{ mA}$. The upper trace and the lower trace are the optical power and input current signal respectively. The horizontal scale is $0.5 \mu\text{sec./div.}$



(c)



(d)

Figure 5.15 -Continued.

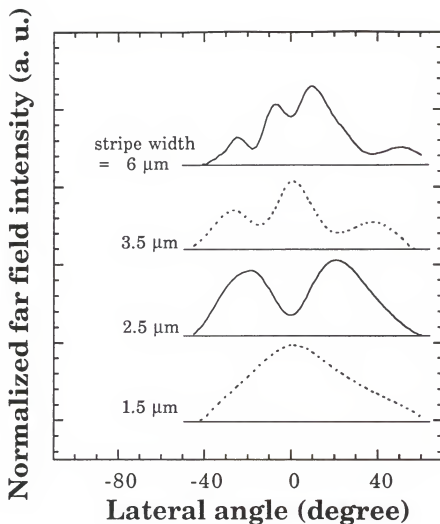


Figure 5.16 Normalized lateral far-field intensity distributions of thin p-clad InGaAs SQW lasers with 300 nm ridge height and various stripe width when measured at $I=1.3 I_{th}$, 4 μsec . current pulse width, 1000 Hz repetition rate and room temperature.

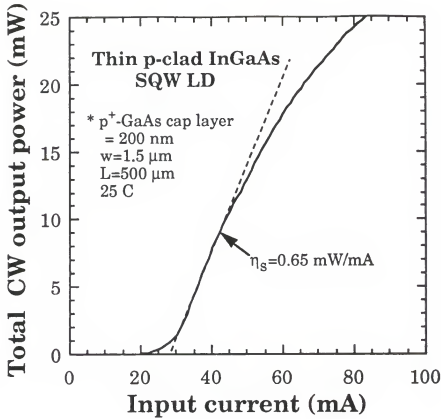


Figure 5.17 Measured room temperature CW output power versus input current characteristics of a 1.5 μm stripe-width, thin p-clad InGaAs SQW laser with 300 nm ridge height.

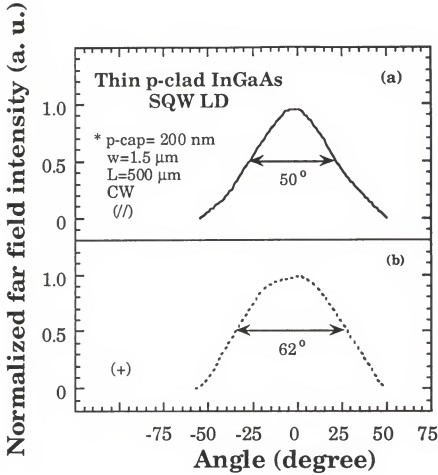


Figure 5.18 (a) Lateral and (b) transverse far-field intensity distributions of thin p-clad InGaAs SQW laser with 300 nm ridge height, 1.5 μm stripe-width when measured at input current $I=1.3\ I_{th}$, CW and room temperature.

CHAPTER 6

SURFACE SENSITIVE LASER DIODES

6.1 Introduction

In chapter 5 we have shown that p^+ -cap layer thickness has great effects on the thin p-clad laser performance. Especially, when the p^+ -cap layer thickness is thick (200 nm), a significant part of the lasing mode could penetrate into the p^+ -cap layer and make the laser lose the optical confinement and behave abnormally. Therefore, with this thin p-clad laser with thick p^+ -cap layer configuration, the interactions between the lasing mode and the thin film material on the top of the p^+ -cap layer should be stronger than those of similar lasers with thin p^+ -cap layer (100 nm). This is because lasing mode confinement of the thin p-clad laser with 100 nm p^+ -cap layer is much larger than that of laser with 200 nm p^+ -cap layer. Additionally, we have also shown that thin p-clad laser performance could be greatly improved when the p^+ -cap layer thickness is decreased below ~170 nm [Wu96a]. Based on these results, the combinations of using the 100 nm p-cap layer as the electron pumped section

and the 200 nm p-cap layer as the surface sensitive section into one laser structure could make it desirable to fabricate a "surface sensitive" diode laser [Wu96b]. With this hybrid laser structure, the application of the semiconductor diode laser as a "sensor" could be possible. The laser structure and the main design principle of the "surface sensitive" device are presented in Section II. In Section III, the details of the fabrication process of the SSLD are described. The device characterizations of the SSLD are outlined in Section IV.

6.2 Device Structure and Theoretical Calculations

The SSLD structure used in this study is shown in Figure 6.1, where the device is designed by inserting a thick p⁺-cap section (t_{cap} nm) into a thin p⁺-cap layer laser ($t_{\text{cap}} \sim 100$ nm) in which the "thick" p⁺-cap layer is used as the surface sensitive section and the "thin" p⁺-cap layer as the electron-pumped section. A thin film material with a variable absorbing property at the lasing wavelength and t_{film} thickness is deposited on the top of the sensor section as a sensor medium for the diode laser. The main operation principle of this laser structure to be used as a surface sensitive laser (SSLD) is to use shiny Au as the p-contact for the electron-pumped sections and change the absorption property of the deposited film through a chemical reaction between the

absorbing film and the material to be sensed, which could lead to changes of diode laser performance.

To check the effects of the absorbing material on the top of the sensor section, we have calculated the modal loss of the sensor section as a function of material loss α_{film} of the absorbing film at various absorbing film thickness t_{film} . Figure 6.2 shows the calculated dependence of modal loss on α_{film} at various film thickness: $t_{film} = 10$ nm, 50 nm and 100 nm. As can be seen from this plot, the modal loss of the sensor section is a linear function of α_{film} and greatly depends on t_{film} . When t_{film} is less than 50 nm and α_{film} is constant, modal loss increases quickly with t_{film} and becomes saturated when t_{film} is thicker than 100 nm.

Besides the effects caused by α_{film} , we are interested in checking the influence of the p⁺-cap layer thickness t_{cap} on the modal loss of the sensor section. The variations of the modal loss of the sensor section are then calculated at various t_{cap} and shown in Figure 6.3. In the computations, a $t_{film} = 100$ nm and various α_{film} of 0.2×10^4 cm⁻¹, 1.0×10^4 cm⁻¹, 2.5×10^4 cm⁻¹, 5×10^4 cm⁻¹ are assumed. From this figure, we can find that strong interactions between the lasing mode and the absorbing film only occur when t_{film} is larger than ~150 nm, in addition, α_{film} has to be larger than 10000 cm⁻¹ to generate significant effects. The peak interactions occur around $t_{cap} =$

180 nm. At constant $t_{cap} = 200$ nm, the modal loss is ~ 86 cm^{-1} when α_{film} is at 10^4 cm^{-1} and becomes as high as ~ 190 cm^{-1} when α_{film} is changed to 2.5×10^4 .

In order to understand the threshold behavior of the SSLD device, a Fabry-Perot model shown in Figure 6.4 is used to model the surface sensitive laser diode performance. In this plot, the laser cavity length L is divided into three sections: two pumped sections (section 1 and section 3), L_1 and L_3 ; and one unpumped section i.e. sensor section (section 2) L_2 . The associated real part and imaginary part of the refractive index value of section i ($i=1,2,3$) is expressed as n_i and n_i' respectively. In order to simplify the calculation, we assume a normal incidence case of the light intensity inside the laser cavity. The power reflectivity and power transmission coefficient when light intensity is passing from region i to region j is denoted as R_{ij} and T_{ij} respectively, where $R_{ij}=R_{ji}$ and $T_{ij}=T_{ji}=1-R_{ij}$. R_1 and R_3 are the power reflectivity of the laser facets ($R_1=R_3 \sim 0.32$ in this case). G_i and α_i represent the optical gain and modal loss of section i ($i=1,2,3$). At first, a lasing mode with power intensity I_1 propagating from $z=0$ in the section 1 of laser cavity is assumed. After the combined effects of optical gain G_1 and modal loss α_1 in the L_1 cavity, part of the power intensity in section 1 is transmitted into section 2. At $z=L_1$ of the section 2, the power intensity is I_2 . Similarly, part of the

power intensity in section 2 is transmitted to the section 3 after passing through the L_2 sensor section. At $z=L_1+L_2$ in the section 3, the power intensity becomes I_3 . At $z=L_1+L_2+L_3$ in this section, part of the power intensity is reflected and becomes I_4 . After propagating L_3 cavity length in the negative z direction, part of the power intensity is transmitted into the section 2 and becomes I_5 at $z=L-L_3$ in the section 2. At $z=L-L_3-L_2$ in section 1, the transmitted power intensity from section 2 is I_6 . After propagating the L_1 cavity length in section 1, part of the power intensity would be reflected from the laser facet at $z=L-L_1-L_2-L_3$ in section 1 and becomes I_7 . The associated power intensity I_j ($j=1$ to 7) can be expressed as the following equations.

$$I_2 = I_1 * e^{(G_1 - \alpha_1)L_1} * T_{12} \quad (6.2.1)$$

$$I_3 = I_2 * e^{(G_2 - \alpha_2)L_2} * T_{23} \quad (6.2.2)$$

$$I_4 = I_3 * e^{(G_3 - \alpha_3)L_3} * R_3 \quad (6.2.3)$$

$$I_5 = I_4 * e^{(G_3 - \alpha_3)L_3} * T_{32} \quad (6.2.4)$$

$$I_6 = I_5 * e^{(G_2 - \alpha_2)L_2} * T_{21} \quad (6.2.5)$$

$$I_7 = I_6 * e^{(G_1 - \alpha_1)L_1} * R_1 \quad (6.2.6)$$

After a simple manipulation from equation (6.2.1) to equation (6.2.6) and assume $T_{ij}=T_{ji}=T_2$ ($i, j=1, 2, 3$), one can obtain the relationship between I_7 and I_1 as shown in equation (6.2.7).

$$I_7 = I_1 * e^{2[(G_1 - \alpha_1)L_1 + (G_2 - \alpha_2)L_2 + (G_3 - \alpha_3)L_3]} * T_2^4 * R_1 * R_3 \quad (6.2.7)$$

Equation (6.2.7) can be further simplified, if the pumped section is made of the same t_{cap} and $G_1=G_3$, $\alpha_1=\alpha_3$. At the laser oscillating condition, I_7 is equal to I_1 . Therefore, one can obtain a closed form equation relating the optical gain with α_2 , L_2 and L_{pump} .

$$G_1 = \alpha_1 + \{ [2\alpha_2 L_2 + \ln(\frac{1}{T_2^4 R_1 R_3})] / (2L_{pump}) \} \quad (6.2.8)$$

where L_{pump} is the total pumped cavity length; $L_{pump}=L_1+L_3$

In deriving equation (6.2.8), only the transmitted parts of the power intensity at the junction between section 1 and section 2, and the junction between section 2 and section 3 are considered, the reflected parts are ignored. This is because the power reflectivity R_{ij} ($i, j=1, 2, 3$) at the junction is very small and can be negligible (this will be shown in the following). At threshold condition, the optical gain G_1 should be equal to threshold mode gain G_{th} . Consequently, the threshold mode gain G_{th} of the SSLD can be expressed by the following equation:

$$G_{th} = G_1 = \alpha_1 + \{ [2\alpha_2 L_2 + \ln(\frac{1}{T_2^4 R_1 R_3})] / (2L_{pump}) \} \quad (6.2.9)$$

As can be seen from equation (6.2.9), the threshold gain G_{th} depends on both the SSLD geometrical parameters (L_{pump} and L_2) and the modal loss in the pumped section as well as the sensor section.

By using equation (6.2.9), one can get the G_{th} value required for the SSLD with various designed structure. For example, we select the pumped section $L_{pump}=850 \mu m$, sensor section $L_{sensor}=150 \mu m$ and $t_{cap}=200 \text{ nm}$. The complex effective refractive index values of the sensor section and the pumped section at 950 nm lasing wavelength are calculated as $n(\text{sensor}) = (n_2, n_2') = (3.32, j0.0027)$, $n(\text{pump}) = (n_1, n_1') = (3.263, j0.000023)$, where we assume the sensor section is covered with $t_{film}=100 \text{ nm}$ film ($\alpha_{film}=5 \times 10^4 \text{ cm}^{-1}$) and the pumped section with shiny Au. Under this condition, we can estimate the power transmittance $T_{12}=0.999925 \sim 1$. Therefore, equation (6.2.9) can be reduced as:

$$G_{th} = G_1 = \alpha_1 + \{ [2\alpha_2 L_2 + \ln(\frac{1}{R_1 R_3})] / (2L_{pump}) \} \quad (6.2.10)$$

By substituting the calculated results of Figure 6.2 into equation (6.2.10), we can obtain the dependence of threshold mode gain G_{th} on the variations of α_{film} as shown in Figure 6.5, in which the sensor section $L_{sensor}=150 \mu m$ and a modal loss $\alpha_1=8 \text{ cm}^{-1}$ [Wu94b] in the pumped sections are assumed. In this plot,

we can find that G_{th} increases monolithically with α_{film} and the increasing rate becomes saturated as t_{film} is thicker than 100 nm. Figure 6.6 shows the calculated variations of G_{th} as a function of t_{cap} by substituting the results of Figure 6.3 into equation (6.2.10), where $L_{sensor}=150\text{ }\mu\text{m}$ and $t_{film}=100\text{ nm}$ are assumed. As can be seen from this plot, at $t_{cap}=200\text{ nm}$, G_{th} could be changed from 34 cm^{-1} to 86 cm^{-1} when α_{film} is increased from $\alpha_{film}=1\times 10^4\text{ cm}^{-1}$ to $\alpha_{film}=5\times 10^4\text{ cm}^{-1}$. In addition to the calculated effects caused by α_{film} and t_{cap} , we are interested in understanding the variations of G_{th} at different pumped cavity length L_{pump} . Figure 6.7 shows the dependence of G_{th} on the various pumped cavity length L_{pump} , where a $t_{cap}=200\text{ nm}$ of the sensor section and a $t_{film}=100\text{ nm}$ with different α_{film} values are considered. From this figure, with $\alpha_{film} \leq 10^4\text{ cm}^{-1}$, we can find that threshold mode gain G_{th} increases quickly when L_{pump} is shorter than $400\text{ }\mu\text{m}$. However, for larger α_{film} value ($\alpha_{film} \geq 2.5\times 10^4\text{ cm}^{-1}$), the calculated G_{th} increases significantly as L_{pump} is decreased below $800\text{ }\mu\text{m}$. At $L_{pump}=850\text{ }\mu\text{m}$, G_{th} could be changed from 28 cm^{-1} to 87 cm^{-1} when α_{film} is increased from $0.5\times 10^4\text{ cm}^{-1}$ to $5.0\times 10^4\text{ cm}^{-1}$. This indicates that threshold mode gain required for lasers to reach threshold condition could be very sensitive to the material loss α_{film} of the absorbing film. Consequently, it is possible for us to fabricate a

surface sensitive laser diode (SSLD) by using the proposed device structure as shown in Figure 6.1.

6.3 Device Fabrications

To fabricate surface sensitive laser diodes, 150 μm stripe width on 1000 μm centers are first defined by using the standard photolithography process as the "sensor stripes". Pulsed anodic oxidation technique is then used to etch away part of the p^+ -cap layer on the outside sensor stripe region. Usually, the remaining p^+ -cap layer thickness is ~ 100 nm by controlling the oxidation time at ~ 2.5 minutes. The remaining native oxide is removed by using a MIF-312 developer solution. After the first oxidation step, 100 μm stripe width on 500 μm centers are defined as the "pumped stripes" with the stripe direction perpendicular to the sensor stripes. The outside pumped stripe region is oxidized by the second anodic oxidation step to remove the remaining p^+ -GaAs cap layer for reducing the possible current spreading effects. At this step, the sensor section and the pumped section are then generated with the associated p^+ -cap layer thickness as $t_{\text{cap}}(\text{sensor}) = 200$ nm, $t_{\text{cap}}(\text{pump}) = \sim 100$ nm. After this step, wafer is cleaned and covered with new photoresist to protect the p^+ -cap layer surface during the lapping process. Following the lapping step, a metallurgy of Ge(20 nm)/Au(40 nm)/Ni(25 nm)/Au(50 nm) is evaporated sequentially on the substrate side and annealed at 430 C for $\sim 5'$ to obtain

a n-type ohmic contact. To deposit the Au contact on the p'-cap layer on the pumped stripe, Au-plating technique is used as described in Chapter 4. Before this process, the sensor stripe is protected by new photoresist. Lasers with total cavity length $L=1000\text{ }\mu\text{m}$ ($L=L_{\text{pump}}+L_{\text{sensor}}$), $500\text{ }\mu\text{m}$ wide is cleaved and soldered on the In-coated copper blocks and characterized. Figure 6.8 (a) and (b) show the top view picture and the schematic diagram of the finished surface sensitive laser diode. As can be seen from the device picture, the sensor section is well defined in the central portion of the device and makes it easy for depositing the absorbing material on this sensor section.

6.4 Device Characterizations

To check the uniformity of the surface sensitive laser diode, 20 devices are prepared and measured. Figure 6.9 shows the measured pulse P-I characteristics of these 20 SSLDs at 2 $\mu\text{sec.}$ pulse width and 1000 Hz repetition rate. The lasing wavelengths of these 20 samples are ranged from 941 nm to 943 nm, which are $\sim 10\text{ nm}$ shorter than the regular lasers without sensor section. This could be due to band filling effects [Chin88] caused by the fact that more gain are required for these lasers to reach threshold condition. The measured results indicate good uniformity of device performance and also confirm the feasibility of fabricating lasers by using this partially oxidized technique.

To know if the diode laser performance is sensitive to the material placed on the top of the sensor section, several material types are used for the experiments. Figure 6.10 shows the variations of pulse P-I characteristics for sample #1 measured before and after the sensor section is covered with dye 1 material which has smaller absorption effects on the lasing wavelength. As can be seen from this figure, the threshold current almost remains unchanged. At fixed current, only a small decrease of output power is obtained after applying the dye 1 material. In the second experiment, a dye 2 material with a strong absorption effects on the lasing wavelength is placed on the partial sensor section of sample #2. Figure 6.11 is the variations of the P-I characteristics of this sample measured without and with this dye 2 thin film. It is very interesting to find that this dye 2 material has a significant effects on the laser threshold performance. Before the application of this dye film, threshold current is $I_{th} = 200$ mA. After the application of dye 2 film, I_{th} is increased to $I_{th} = 280$ mA, i.e. 40% increases. In addition, at fixed current output power changes dramatically, for example, at $I = 300$ mA output power changes from $P(\text{w/o dye 2 film}) = 37$ mW/facet to $P(\text{w/dye 2 film}) = 11$ mW/facet. These results indicate that the diode laser behaviors are very sensitive to this dye 2 material. In the third experiment, sample #3 is measured before and after the dye 2 material is placed on the whole sensor section. As shown in Figure 6.11, the measured P-I characteristics change more significantly than that of

sample #2. Threshold current is almost two times increased from $I_{th}=200$ mA to 390 mA after the sensor section is wholly covered with dye 2 material. At fixed current $I=300$ mA, laser changes from lasing with output power $p=37$ mW per facet to non-lasing behaviors. So far we have proved that laser performance is dependent on the type of material placing on the sensor section, the next step is to check the effects from the material to be detected. Since the absorption coefficient of the dye 2 material can be somewhat changed with NH_3 material, i.e. sensitive to the NH_3 material, we are interested in understanding the effects of NH_3 vapor on the laser performance. To check this point, sample #3 with dye 2 film covered on the sensor section is passing through a solution made of 1 part NH_3 + 200 parts H_2O for ~2 seconds and P-I characteristics measured. From the measured results shown in Figure 6.13, it is noticed that threshold current is increased from $I_{th}=390$ mA to $I_{th}=440$ mA and output power (at $I=500$ mA) decreased from $P=26$ mW/facet to $P=18$ mW/facet after this experiment. The above experiments clearly point out the feasibility of using this unique laser structure as a surface sensitive device.

In order to see if diode laser performance could be recovered by removing the material on the sensor sector, the same sample #3 is dipped in Methanol solution for ~30 seconds and P-I performance characterized. The measured results are shown in Figure 6.13. It is interesting to note that diode laser performance is reversible with threshold current

changed from $I_{th}=440$ mA to $I_{th}=250$ mA. As compared with the results measured before placing dye 2 material, there is a ~50 mA increase of threshold current. This could be due to the material is not thoroughly removed from the sensor section or other unknown reason. Nevertheless, we have shown the possibility of fabricating a "surface sensitive" laser diode with reversible behaviors from this hybrid laser structure which may become useful as a "sensor" in some environment condition.

In summary, a surface sensitive laser diode structure is proposed and fabricated successfully. The basic device operating mechanism discussed in this chapter can be extended to the other material system and could be possible to explore a new application of semiconductor diode lasers for use as a "sensor".

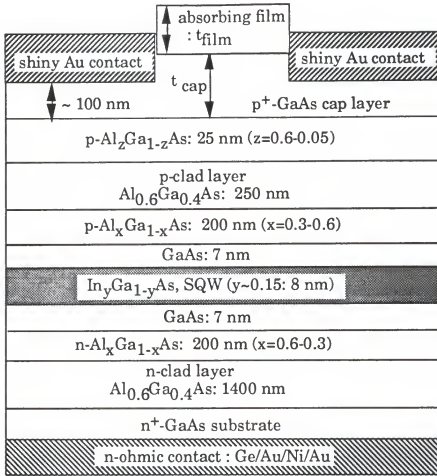


Figure 6.1 Surface sensitive laser diode structure used in this chapter.

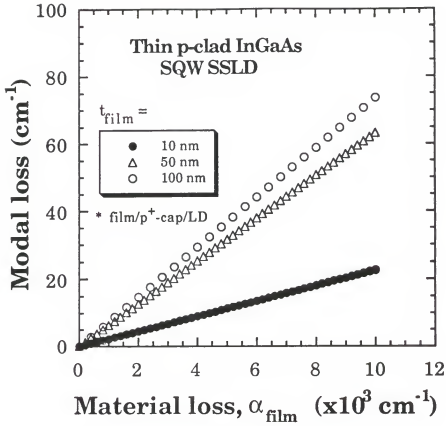


Figure 6.2 The calculated dependence of modal loss of the sensor section ($t_{\text{cap}}=200$ nm) on the material loss α_{film} of the absorbing film shown in Figure 6.1, where different film thickness are considered.

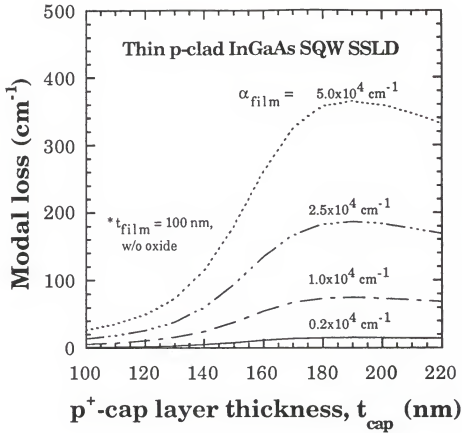


Figure 6.3 The calculated variations of modal loss of the sensor section (shown in Figure 6.1) as a function of p^+ -cap layer thickness t_{cap} , where a absorbing film thickness $t_{\text{film}}=100 \text{ nm}$ and various values of material loss α_{film} are assumed.

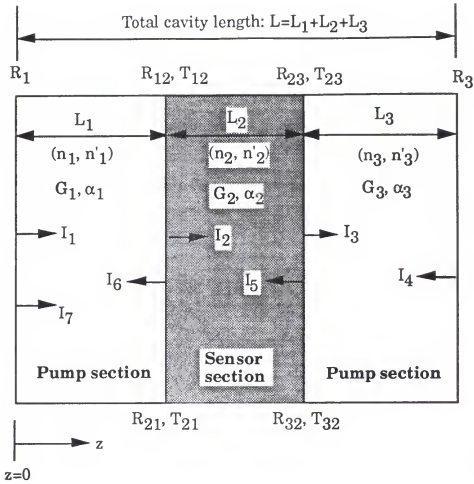


Figure 6.4 The schematic diagram of Fabry-Perot model used to derive the threshold behaviors of surface sensitive laser diode.

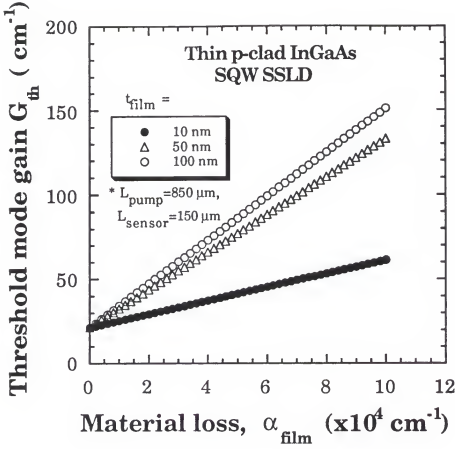


Figure 6.5 The calculated threshold mode gain G_{th} of SSLD as a function of the material loss α_{film} of the absorbing film. It is assumed that total pump section $L_{\text{pump}} = 850 \mu\text{m}$ are covered with gold and sensor section $L_{\text{sensor}} = 150 \mu\text{m}$ placed with different film thickness.

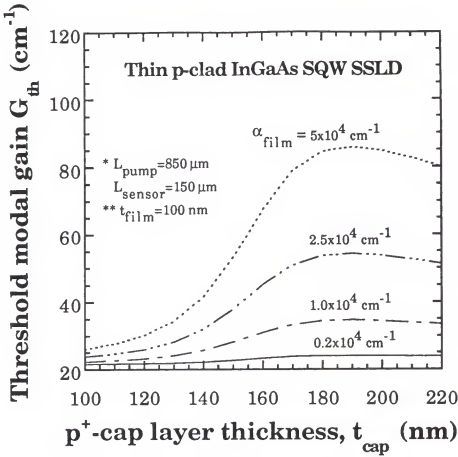


Figure 6.6 The calculated variations of threshold mode gain G_{th} of SSLD (laser structure shown in Figure 6.1) as a function of p^+ -cap layer thickness. It is assumed that total pump section $L_{\text{pump}} = 850 \mu\text{m}$ are covered with gold and sensor section $L_{\text{sensor}} = 150 \mu\text{m}$ placed with various α_{film} values of absorbing film.

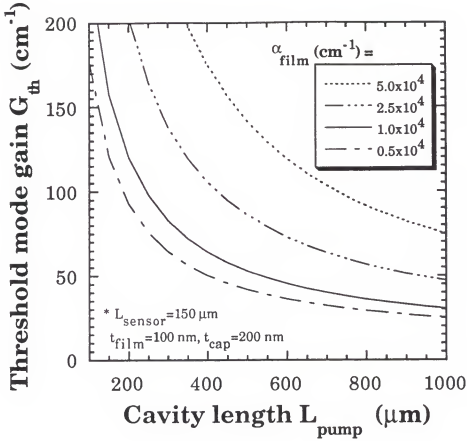
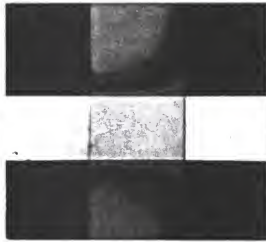
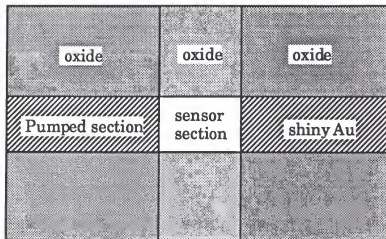


Figure 6.7 The calculated dependence of threshold mode gain G_{th} of SSLD (laser structure shown in Figure 6.1) as a function of total pump cavity length L_{pump} . It is assumed that total pump section $L_{\text{pump}} = 850 \mu\text{m}$ are covered with gold and sensor section $L_{\text{sensor}} = 150 \mu\text{m}$ placed with 100 nm absorbing film with various α_{film} .



(a)



(b)

Figure 6.8 Top view of the finished surface sensitive laser diode (SSLD) (a) picture (b) schematic diagram.

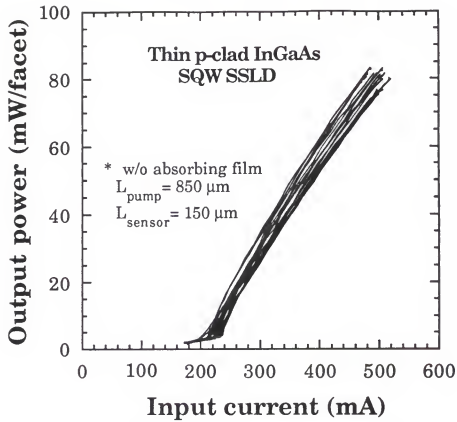


Figure 6.9 Measured pulse P-I characteristics of 20 SSLD samples when operated at 2 microseconds pulse width and 1000 Hz repetition rate, room temperature.

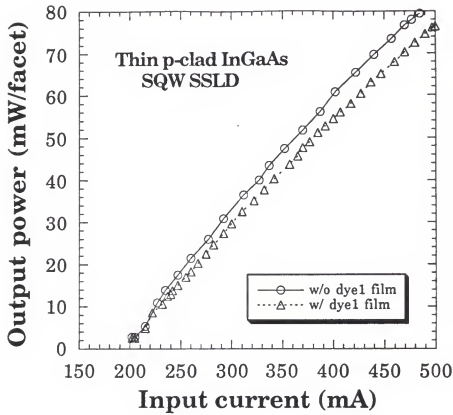


Figure 6.10 Measured pulse P-I characteristics of SSLD sample #1 before and after placing dye 1 material on the sensor section.

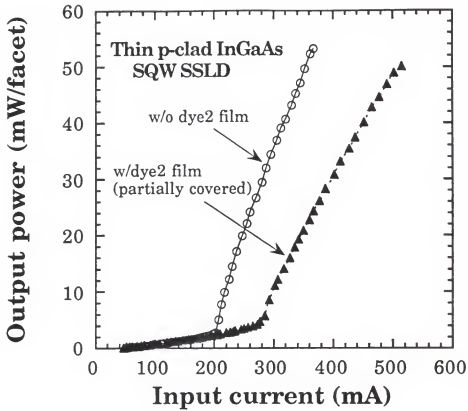


Figure 6.11 The variations of measured P-I characteristics of SSLD sample #2 before and after placing with dye 2 material on part of the sensor section.

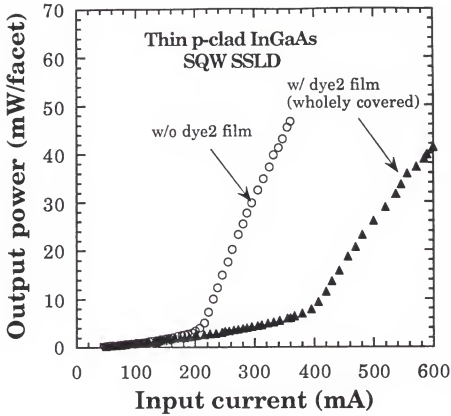


Figure 6.12 The measured variations of P-I characteristics of SSLD sample #3 before and after placing dye 2 material on the whole sensor section.

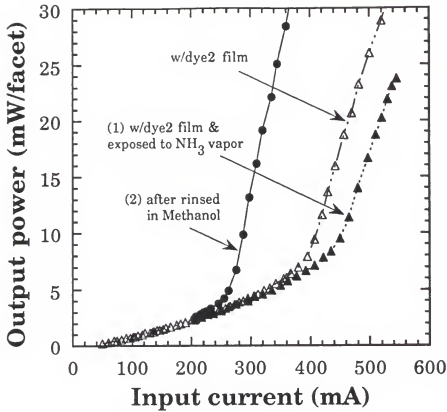


Figure 6.13 The measured variations of P-I characteristics of SS LD sample #3 with dye 2 material on the sensor section after being processed in different conditions: (1) exposed to NH_3 solution ~2 seconds (2) after step (1) then rinsed in Methanol to remove dye 2 film on the sensor section.

CHAPTER 7

SUMMARY AND RECOMMENDATION

7.1 Summary

The p-contact reflectivity effects on the device performance has been demonstrated in thin (250 nm) p-clad, 10 nm InGaAs quantum well lasers. Decreasing the reflectivity of the p-contact metal increases optical mode loss, which increases threshold current, decreases slope efficiency and shifts the emission wavelength. The more than 50 nm wavelength difference between the thin p-clad diode lasers with different p-contact metallurgy can be explained quantitatively by superimposing the threshold gain required for lasing in each case with the corresponding spectral gain curve calculated using standard QW laser theory. To avoid the extra mode loss and obtain a well-behaved thin p-clad diode laser, the p-contact metal can not be annealed. The CW life time tests show that 50 μm stripe-width, Au-contact, thin p-clad diode lasers with epi-side up package can live more than 1000 hrs. when continuously operate with 100 mW output power at room temperature.

Besides the contact reflectivity effects on the diode laser performance, one of the most important feature of the thin p-clad laser structure is that the lateral refractive index step generated in low-ridge diode lasers is sufficient to provide low loss and strong lateral waveguiding. As a result, neither the unusual threshold behaviors nor the wavelength jumps are observed for the shallow ridge, thin p-clad laser when stripe width is changed from 50 μm to 5 μm . In addition, the 5 μm stripe devices are shown to be capable of stable, single lateral mode CW lasing with less than 10 % broadening up to total output power levels of about 70 mW. On the contrary, for the thick p-clad (1300 nm) diode laser, deep etching for obtaining ridge height larger than 1000 nm is required to provide the sufficient waveguiding effects for narrow stripe lasers operating with stable single mode output.

By controlling the p-contact reflectivity, a two-stripe thin p-clad diode laser emitting dual wavelengths was successfully demonstrated. The fabrication process of this dual wavelength diode laser is much simpler and more reliable than those approaches studied before. Based on this experiment results, one can design a thin p-clad diode laser with several emission energy levels inside the single quantum well and select the suitable contact metal to control the emission wavelength to obtain a monolithic multiple wavelength emission diode laser. Additionally, thermal resistance is found to play an important role for diode

lasers operating at high temperature in CW regime. The maximum output power of CW laser performance can be greatly improved by reducing its thermal resistance through the deposition of thick Au layer as the heat spreader.

In addition to the contact reflectivity, another important parameter in determining thin p-clad diode laser performance is the p'-GaAs cap layer thickness. The increasing of p-cap thickness could result in the decrease of optical confinement of lasing mode and induce large modal loss. For the thin p-clad (250 nm) laser structure used in this study, long time lasing delay and abnormal high threshold behaviors are observed for both wide stripe and narrow stripe gain-guided lasers when p-cap layer thickness is as thick as 200 nm. The lasing delay in the wide stripe lasers can be eliminated and diode laser performance improved dramatically when p-cap layer thickness is decreased below 170 nm. This long delay is attributed to the time it takes for the active region to heat to the point where net mode gain exceeds mirror loss by the increase of overlap between the transverse mode profile (perpendicular to the QW plane) and the QW material gain as well as the decrease of the absorbing loss in the gold contact layer. In contrast to the strong lateral waveguiding effects obtained in narrow stripe, shallow-ridge, thin p-clad lasers fabricated with 100 nm p-cap layer, long time lasing delay and Q-switching lasing behaviors are observed for narrow stripe lasers with 300 nm ridge height and an effective refractive index step of 3.5×10^{-2} when the

stripe width is $w=6\text{ }\mu\text{m}$ and $w=3.5, 2.5\text{ }\mu\text{m}$ respectively. At $1.5\text{ }\mu\text{m}$ stripe width, strong lateral waveguiding effects are obtained and become sufficient to somehow improve the transverse waveguiding which makes laser operate in a low threshold current regime with CW differential quantum efficiency 50 %.

By combining 100 nm and 200 nm p⁺-cap layer structures into one laser and removing the gold layer from the 200 nm section, laser output power at fixed current becomes dependent on the type of material placed on the 200 nm section. Experiments of using these "surface sensitive laser diodes" to the possible application for use as a "sensor" have been successfully demonstrated.

7.2 Recommendation for Future Study

Several areas are needed to do the further study, most important among them are:

- (1) The improvement of adhesion between metal contact and p⁺-GaAs cap layer.

The adhesion quality between Au contact and p-cap layer is very crucial in determining thin p-clad lasers performance. The adhesion quality not only depends on the clean process before the deposition of p-metal but also depends on the metal itself. For the GaAs material, Au shows poor adhesion property as compared to the other metal such as

nickel (Ni) and chromium (Cr). However, these materials also show very low reflectivity at the lasing wavelength and become lossy metal for thin p-clad diode lasers. On the other hand, the modal loss induced by the low reflective metal could be dependent on the metal thickness. In the calculated results shown in Figure 7.1, we can see that modal loss for both metal type is in linear proportion to the metal thickness upto 100 nm metal thickness and then becomes gradually saturated when metal thickness is beyond 200 nm. If one can control the metal thickness below 20 Å, the resultant modal loss could be less than 10 cm^{-1} , which could be acceptable in most diode laser performance. The important issue for this method is how to control the uniformity of metal thickness during the deposition process to avoid possible increase of scattering loss due to the nonuniformity of metal thickness. Another method to improve the adhesion property is to use Au-plating technique instead of Au evaporation process. Both methods need to be further studied to show the uniformity of laser performance.

(2) Optimize and extend the surface sensitive device operation mechanism to the other semiconductor laser material system

Thin p-clad diode laser performance has been shown greatly dependent on the p-cap layer thickness. Based on these results, a hybrid laser diode structure with surface

sensitive capability has been successfully demonstrated in GaAs/InGaAs material system by selectively controlling the p-cap layer thickness used as either the electron-pumped section or the sensor section. However, several parameters need to be optimized to obtain even better device performance and reliability, such as the optimal cavity length for either pumped section L_{pump} or sensor section L_{sensor} , facet coating on both facets to protect lasers from being damaged by the working environment. On the other hand, the calculated results shown in Figure 7.2 indicate that it could be possible to design a SSLD with thin native oxide grown on the top of sensor section. With this extra oxide grown process, both the experimental and theoretical work need to be further studied. In addition, by using similar device operating mechanism combined with the semiconductor quantum well characteristics, the operating mechanism of SSLD can be extended to other semiconductor material systems with suitable operating wavelength for use as a sensor.

(3) Distributed Feedback (DFB) Diode Laser:

Gain coupling DFB lasers with better performance have been theoretically studied and realized. The usual way of realizing gain coupling DFB diode lasers is to grow an absorbing layer close to the active region and followed by the grating formation procedure and the regrowth process, which makes the whole fabrication process complicated. By

using either the contact reflectivity effects or controlling the p-cap layer thickness, one can control the modal loss of thin p-clad diode laser. As a result, the fabrication process of gain-coupled DFB lasers should become much simpler than those reported before. In addition, from the optimization of diode laser structure, single spatial mode operation with linear P-I profiles to much higher CW powers should be possible. This feature combined with the flexibility of fabricating different diffraction grating types in thin p-clad material (no regrowth required) could lead to the development of higher performance gain-coupled DFB lasers.

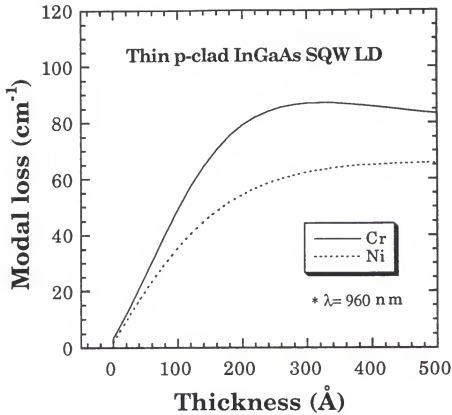


Figure 7.1 Calculated dependence of modal loss of thin p-clad InGaAs SQW laser as a function of different metal thickness: chromium(Cr) and nickel (Ni).

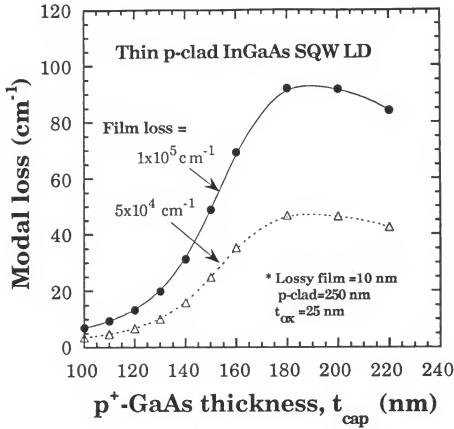


Figure 7.2 Calculated variations of modal loss as a function of p-cap layer thickness when two different lossy films with 10 nm thickness are covered on the top of p-cap layer, where the refractive indexes of the oxide and the lossy film are 1.8 and 1.5 respectively.

REFERENCES

- [Adac85] S. Adachi, "GaAs, AlAs, and $\text{Al}_x\text{Ga}_{1-x}\text{As}$: material parameters for use in research and device applications," J. Appl. Phys., vol. 58, pp. R1-R29, 1985.
- [Adam73] M. J. Adams, S. Grüdorfer, G. H. B. Thompson, C. F. L. Davies, and D. Mistry, "Time delay and Q-switching in homostructure and heterostructure injection lasers," IEEE J. Quantum Electron., vol. QE-9, pp.328-337, 1973.
- [Agra84] Govind P. Agrawal "Lateral analysis of quasi-index-guided injection lasers: transition from gain to index guiding," IEEE J. Lightwave Technol. vol. LT-2, pp. 537-543, 1984.
- [Aiki76] K. Aiki, M. Nakamura, and J. Umeda, "Frequency multiplexing light-source with monolithically integrated distributed-feedback diode lasers," Appl. Phys. Lett., vol. 29, pp. 506-508, 1976.
- [Bahf90] A. Behfar-Rad, J. R. Shealy, S. R. Chinn, and S. S. Wong, "Effect of cladding layer thickness on the performance of GaAs-AlGaAs graded index separate confinement heterostructure single quantum-well lasers," IEEE J.Quantum Electron., vol.26, pp. 1476-1480, 1990.
- [Bast88] Gerald Bastard ed., "Wave mechanics applied to semiconductor heterostructures," Les Ulis Cedex, France:Halsted Press, 1988, Chapter 1.
- [Beer91a] K. J. Beernink, J. J. Alwan, and J. J. Coleman, "Wavelength switching in narrow oxide stripe InGaAs-GaAs-AlGaAs strained-layer quantum well heterostructure lasers," Appl. Phys. Lett. vol. 58, pp. 2076-2078, 1991.
- [Beer91b] K. J. Beernink, J. J. Alwan, and J. J. Coleman, "Antiguiding in narrow stripe gain-guided InGaAs-GaAs strained-layer lasers," J. Appl. Phys., vol.69, pp. 56-60, 1991.

- [Boua82] N. Bouadma, J. C. Bouley, and J. Riou, "Dual wavelength (GaAs)Al laser," *Electron. Lett.* vol. 18, pp.871-873, 1982.
- [Bour90] D. P. Bour, N. A. Dinkel, D. B Gilbert, K. B. Fabian and M. G. Harvey, "980 nm diode laser for pumping Er^{3+} -doped fiber amplifiers," *IEEE Photon. Technol. Lett.*, vol. 2, pp. 153-155, 1990.
- [But175] J.K Butler, H. Kressel and I Ladany, "Internal optical loss in very thin CW heterojunction laser diodes," *IEEE, Quantum Electronics*, vol. QE-11, pp. 402-408, 1975.
- [Case75] H. C. Casey Jr. and M. B. Panish, "Influence of $\text{Al}_x\text{Ga}_{1-x}\text{As}$ layer thickness on threshold current density and differential quantum efficiency for $\text{GaAs-Al}_x\text{Ga}_{1-x}\text{As}$ DH lasers," *J. Appl. Phys.*, vol. 46, pp. 1393-1395, 1975.
- [Chin88] S. R. Chinn, P. S. Zory and A. R. Reisinger, "A model for GRINSCH SQW diode lasers," *IEEE Quantum Electron.* vol. 24 pp. 2191-2214, 1988.
- [Cole93] James J. Coleman "Strained layer quantum well heterostructure lasers," in *Quantum Well lasers*, P. S. Zory ed., New York: Academic, 1993.
- [Corz93] Scott W. Corzine, Ran-Hong Yan and Larry A. Coldren "Optical gain in III-V Bulk and Quantum Well Semiconductors," in *Quantum Well lasers*, P. S. Zory ed., New York: Academic, 1993.
- [Deme89] P. L. Demers. et.al. Modeig/II version 1.1, Dallas, TX, Southern Methodist University: Sep. 1989.
- [Dutt81] N. K. Dutta, "Calculated temperature dependence of threshold current of $\text{GaAs-Al}_x\text{Ga}_{1-x}\text{As}$ double heterostructure lasers," *J. Appl. Phys.*, vol. 52, pp.70-73, 1981.
- [Dutt83] N. K. Dutta, "Calculation of Auger rates in quantum well structure and its application to InGaAsP quantum well lasers," *J. Appl. Phys.*, vol. 54, pp. 1236-1245, 1983.
- [Dutt86] N. K. Dutta, T. Cella, J. L. Zilko, D. A. Ackerman, A. B. Piccirilli, and L. I. Greene, "InGaAsP closely spaced dual wavelength laser," *Appl. Phys. Lett.*, vol. 48, pp.1725-1726, 1986.

- [Dyme72] J. C. Dymert, J. E. Ripper, and J. P. Lee, "Measurement and interpretation of long spontaneous lifetime in double heterostructure lasers," J. Appl. Phys., vol. 43, pp. 452-457, 1972.
- [Eple90] John E. Epler, D. W. Treat, S. E. Nelson, and Thomas L. Paoli, "Multiple-wavelength diode laser superarray," IEEE Quantum Electronics, vol. QE-26, pp. 663-668, 1990.
- [Fisc87] S. E. Fischer, D. Fekete, G. B. Feak, and J. M. Ballantyne, "Ridge waveguide injection laser with GaInAs strained-layer quantum well ($\lambda=1\mu\text{m}$)," Appl. Phys. Lett. vol. 50, pp. 714-716, 1987.
- [Garb93] D. Z. Garbuzov and V. B. Khalfin, "Single quantum well InGaAsP and AlGaAs lasers: A study of some peculiarities," in Quantum Well lasers, P. S. Zory ed., New York:Academic, 1993.
- [Garr87] B. Garrett, and J. E. A. Whiteaway, "Self stabilization of the fundamental lateral mode in index-guided semiconductor lasers," IEE Proc., vol. 134, pt. J, No. 1, pp. 11-15, 1987.
- [Good75] A. R. Goodwin, J. R. Peters, M. Pion, G. H. B. Thompson, and J. E. A. Whiteaway, "Threshold temperature characteristics of double heterostructure $\text{Ga}_{1-x}\text{Al}_x\text{As}$ lasers," J. Appl. Phys., vol. 46, pp.3126-3131, 1975.
- [Gray72] D. E. Gray ed., American Institute of Physics Handbook, McGraw-Hill, 3rd edition, 1972.
- [Grov94] M. J. Grove, D. A. Hudson, P. S. Zory, R. J. Dalby, C. M. Harding, and A. Rosenberg, "Pulsed anodic oxides for III-V semiconductor device fabrication," J. Appl. Phys., vol.76, pp. 587-589,1994.
- [Grüd73] S. Grüdorfer and M. J. Adams, "Theoretical considerations of time delays in semiconductor lasers," IEEE J. Quantum Electron., vol. QE-9, pp.814-819, 1973.
- [Grüd74] S. Grüdorfer and M. J. Adams, "New theory of internal Q switching in semiconductor lasers," Electron. Lett., vol. 10, pp.354-356, 1974.
- [Guth94] James Guthrie, G. L. Tan, M. Ohkubo, T. Fukushima, Y. Ikegami, T. Ijichi, M. Irikawa, R. S. Mand, and J. M. Xu, "Beam instability in 980-nm power lasers: experiment and analysis," IEEE Photon. Technol. Lett., vol. 6, pp. 1409-1411, 1994.

- [Jones75] P. Garel-Jones and John C. Dymont, "Calculations of the continuous-wave lasing range and light-output power for double-heterostructure lasers," IEEE J. Quantum Electron., vol. QE-11, pp.408-413, 1975.
- [Joyc75] W. B. Joyce and R. W. Dixon, "Thermal resistance of heterostructure lasers," J. Appl. Phys., vol 46, pp. 854-862, 1975.
- [Lee91] Johnson Lee, C. Shieh, and M. O. Vassell, "Variation of threshold current with cavity length in strained-layer InGaAs/GaAs quantum well lasers," J. Appl. Phys., vol. 69, pp. 1882-1891, 1991.
- [Luo90] H. J. Luo and P. S. Zory, "Distributed feedback coupling coefficient in diode lasers with metalized gratings," IEEE Photon. Technol. Lett., vol. 2, pp. 614-616, 1990.
- [Luo92] Y. Luo, H. L. Cao, M. Dobashi, H. Hosomatsu, Y. Nakano, and K. Tada, "Gain-coupled distributed feedback semiconductor lasers with an absorptive conduction-type inverted grating," IEEE Photon. Technol. Lett., vol. 4, pp. 692-695, 1992.
- [Maco87] S. H. Macomber, J. S. Mott, R. J. Noll, G. M. Gallatin, E. J. Gratrix, S. L. O'Dwyer, and S. A. Lambert, "Surface emitting distributed feedback semiconductor laser," Appl. Phys. Lett. Vol. 51, pp. 472-474, 1987.
- [Marp64] D. T. F. Marple, "Refractive index of GaAs," J. Appl. Phys., vol. 35, pp.1241-1242, 1964.
- [Maws86] L. J. Mawst, M. E. Givens, C. A. Zmudzinski, M. A. Emanuel, and J. J. Coleman, "Near-and far-field observations of transient behavior in pulsed graded barrier quantum well lasers," J. Appl. Phys., vol. 60, pp.2613-2615, 1986.
- [Mott89] J. S. Mott and S. H. Macomber, "Two-dimensional surface distributed feedback laser arrays," IEEE, Photo. Technol. Lett. vol. 1, pp.202-204, 1989.
- [Nune77] F. D. Nunes, N. B. Patel and J. E. Ripper, "A theory on long time delay and internal Q switching in GaAs junction lasers," IEEE J. Quantum Electron., vol. QE-13, pp.675-681, 1977.
- [Pan88] S. H. Pan, H. Shen, Z. Hang, F. H. Pollak, W. Zhuang, Q. Xu, A. P. Roth, R. A. Masut, C. Lacelle, and D. Morris, "Photoreflectance study of narrow-

- well strained-layer $\text{In}_x\text{Ga}_{1-x}\text{As}$ /GaAs coupled multiple-quantum-well structures," Phys. Rev. B, vol. 38, pp. 3375-3382, 1988.
- [Paol75] Thomas L. Paoli, "A new technique for measuring the thermal impedance of junction lasers," IEEE J. Quantum Electronics, vol. QE-11, pp.498-503, 1975.
- [Pate87] N. B. Patel, T. J. S. Mattos, F. C. Prince and A. S. Nunes, "Narrow stripe graded barrier single quantum well lasers-threshold current considerations," IEEE J. Quantum Electron., vol. QE-23, pp.988-991, 1987.
- [Prin83] F. C. Prince, N. B. Patel, D. Kasemsel and C. S. Hong, "Long delay time for lasing in very narrow graded barrier single-quantum-well lasers," Electron. Lett., vol. 19, pp.435-437, 1983.
- [Prin85] F. C. Prince, T. J. S. Mattos, N. B. Patel, D. Kasemsel and C. S. Hong, "Waveguiding, spectral, and threshold properties of a stripe geometry single quantum well lasers," IEEE J. Quantum Electron., vol. QE-21, pp.634-639, 1985.
- [Rast91] A. Rast and A. Zach, "Room temperature cw operation of $l = 1.55\text{mm}$ InGaAsP/InP ITG-DFB-BCRW lasers with contact surface grating," Electron. Lett., vol. 27, pp. 108-109, 1991.
- [Ripp74] J. E. Ripper and J. A. Rossi, "Delay and Q switching in semiconductor lasers-still an operation question," IEEE J. Quantum Electron., vol. QE-10, pp.435-441, 1974.
- [Saka82] S. Sakai, T. Aoki, and M. Umeno, "InGaAsP/InP dual wavelength lasers," Electron. Lett. vol. 18, pp. 17-18, 1982.
- [Scif75] D. R. Scifres, R. D. Burnham, and W. Streifer, "Output coupling and distributed feedback utilizing substrate corrugations in double-heterostructure GaAs lasers," Appl. Phys. Lett., vol. 27, pp. 295-297, 1975.
- [Scif76] D. R. Scifres, W. Streifer, and R. D. Burnham, "Leaky wave room-temperature double heterostructure GaAs:GaAlAs diode laser," Appl. Phys. Lett., vol. 29, pp.23-25, 1976.
- [Shan88] Y. Shani, A. Katzir, M. Tacke and H. M. Preier, "Metal clad $\text{Pb}_{1-x}\text{Sn}_x\text{Se}/\text{Pb}_{1-x-y}\text{Eu}_y\text{Sn}_x\text{Se}$ distributed


- feedback lasers," IEEE J. Quantum Electron., vol. QE-24, pp. 2135-2137, 1988.
- [Shie89] C. Shieh, J. Mantz, H. Lee, D. Ackley, and R. Engelmann, "Anomalous dependence of threshold current on the stripe width in gain-guided strained-layer InGaAs/GaAs quantum well lasers," Appl. Phys. Lett., vol. 54, pp. 2521-2523, 1989.
- [Suem75] Y. Suematsu, M. Yamada, and K. Hayashi, "Integrated twin-guide AlGaAs laser with multiheterostructure," IEEE J. Quantum Electron., vol. QE-11, pp.457-460, 1975.
- [Taka78] T. Takagi, "Refractive index of $Ga_{1-x}In_xAs$ prepared by vapor-phase epitaxy," Japanese J. Appl. Phys., vol. 17, pp. 1813-1817, 1978.
- [Take90] Tatsuya Takeshita, Masanobu Okayasu, and Shingo Uehara, "High-power operation in 0.98- μm strained-layer InGaAs-GaAs single-quantum-well ridge waveguidelasers," IEEE Photon. Technol. Lett., vol. 2, pp. 849-851, 1990.
- [Thom80] G.H.B. Thompson ed., "Physics of semiconductor laser devices," New York: Wiley, 1980.
- [Thom74] G. H. B. Thompson, P. R. Selway, G. D. Henshall and J. E. A. Whiteaway, "Role of optical guiding in critical-temperature behavior, delays and Q switching in single heterostructure GaAs/(GaAl)As lasers," Electron. Lett., vol. 19, pp.354-355, 1974.
- [Tien70] P. K. Tien and R. Ulrich, "Theory of prism-film coupler and thin-film light guide," J. Opt. Soc. Am., vol. 60, pp. 1325-1337, 1970.
- [Toku87] Y. Tokuda, Y. Abe. T. Matsui, N. Tsukada, and T. Nakayama, "Dual-wavelength emission from a twin-stripe single quantum well laser," Appl. Phys. Lett., vo. 52, pp. 1664-1666, 1987.
- [Unge93] Peter Unger, Gian-Luca Bona, Roland Germann, Peter Roentgen, and David J. Webb, "Low-threshold strained GaInP quantum-well ridge lasers with AlGaAs cladding layers," IEEE J. Quantum Electron., vol. 29, pp.1880-1883, 1993.
- [Van89] C. G. Van de walle, "Band lineups and deformation potentials in the model-solid theory," Phys. Rev. B, vol. 39, pp1871-1883, 1989.

- [Weas87] R.C. Weast, ed., CRC Handbook of Chemistry and Physics, Florida: CRC Press, 68th edition, 1987.
- [Wu94a] C. H. Wu, P. S. Zory, and M. A. Emanuel, "Large wavelength shifts in thin p-clad InGaAs QW lasers," IEEE/LEOS annual meeting, Boston, Oct. 1994.
- [Wu94b] C. H. Wu, P. S. Zory, and M. A. Emanuel, "Contact reflectivity effects on thin p-clad InGaAs single quantum-well lasers," IEEE Photo. Technol. Lett., vol.6, pp.1427-1429, 1994.
- [Wu95] C. H. Wu, P. S. Zory, and M. A. Emanuel, "Characterization of thin p-clad InGaAs single-quantum-well lasers," IEEE Photo. Technol. Lett., vol.7, pp.718-720, 1995.
- [Wu96a] C. H. Wu, P. S. Zory, and M. A. Emanuel, "p⁺-GaAs cap layer thickness effects on thin p-clad InGaAs single-quantum-well lasers," in preparation.
- [Wu96b] C. H. Wu, P. S. Zory, and M. A. Emanuel, "InGaAs single-quantum-well surface sensitive diode lasers," in preparation.
- [Yone73] H. Yonezu, I. Sakuma, K. Kobayashi, T. Kamejima, M. Ueno, and Y. Nannichi, "A GaAs-Al_xGa_{1-x}As double heterostructure planar stripe laser," Japanese J. Appl. Phys., vol. 12, pp. 1585-1592, 1973.
- [Zory75] P. Zory and L. D. Comerford, "Grating-coupled double-heterostructure AlGaAs diode lasers," IEEE, Quantum Electronics, vol. QE-11, pp. 451-457, 1975.
- [Zory86] P. S. Zory, A. R. Reisinger, R. G. Water, L. J. Mawst, C. A. Zmudzinski, M. A. Emanuel, M. E. Givens, and J. J. Coleman, "Anomalous temperature dependence of threshold for thin quantum well AlGaAs diode lasers" Appl. Phys. Lett. vol. 49, pp. 16-18, 1986.

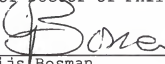
BIOGRAPHICAL SKETCH

Chih-Hung Wu was born in Taiwan in January 1960. He received his B.S. degree in electrical engineering from National Cheng-Kung University, Tainan, Taiwan, in June 1982. After his graduation, he was a communication lieutenant in army for two year of military service. In 1984 he became a graduate student in Institute of Electrical and Computer Engineering of National Cheng-Kung University and received his M.S. degree in 1986 with the thesis titled " The studies of dopants incorporation in GaAs grown by pressure metal organic vapor phase epitaxy." Then he joined the Institute of Nuclear Energy Research (INER) as a assistant researcher in 1986 and was involved in designing and developing the fabrication of high power single heterostructure (SH) diode laser arrays. In 1992, he won a scholarship from INER to start his Ph.D. study in USA. Since August 1993 has been a graduate research assistant at the Photonics Research Laboratory in the Department of Electrical and Computer Engineering of the University of Florida, where he is engaged in research on thin p-clad quantum well lasers and developing fabricating process for CW high power laser array. His research interests include semiconductor material growth and device fabrication process development.


I certify that I have read this study and that in my opinion it conforms to acceptable standards of scholarly presentation and is fully adequate, in scope and quality, as a dissertation for the degree of Doctor of Philosophy.


Peter S. Zory, Chairman
Professor of Electrical and
Computer Engineering

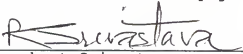
I certify that I have read this study and that in my opinion it conforms to acceptable standards of scholarly presentation and is fully adequate, in scope and quality, as a dissertation for the degree of Doctor of Philosophy.


Gijs Bosman
Professor of Electrical and
Computer Engineering

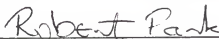
I certify that I have read this study and that in my opinion it conforms to acceptable standards of scholarly presentation and is fully adequate, in scope and quality, as a dissertation for the degree of Doctor of Philosophy.


Arnost Neugroschel
Professor of Electrical and
Computer Engineering

I certify that I have read this study and that in my opinion it conforms to acceptable standards of scholarly presentation and is fully adequate, in scope and quality, as a dissertation for the degree of Doctor of Philosophy.


Ramakant Srivastava
Professor of Electrical and
Computer Engineering

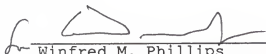
I certify that I have read this study and that in my opinion it conforms to acceptable standards of scholarly presentation and is fully adequate, in scope and quality, as a dissertation for the degree of Doctor of Philosophy.



Robert M. Park
Professor of Materials Science
and Engineering

This dissertation was submitted to the Graduate Faculty of the College of Engineering and to the Graduate School and was accepted as partial fulfillment of the requirements for the degree of Doctor of Philosophy.

May 1996



Winfred M. Phillips
Dean, College of Engineering

Karen A. Holbrook
Dean, Graduate School